(12) INTERNATIONAL APPLICATION PUBLISHED UNDER THE PATENT COOPERATION TREATY (PCT)

(19) World Intellectual Property Organization
International Bureau

(43) International Publication Date
19 December 2024 (19.12.2024)

WIPO | PCT

(10) International Publication Number
WO 2024/259360 A1

(51) International Patent Classification:
A61B 5/0245 (2006.01) *A61B 5/11* (2006.01)
A61B 5/024 (2006.01) *A61B 5/00* (2006.01)

(21) International Application Number:
PCT/US2024/034184

(22) International Filing Date:
14 June 2024 (14.06.2024)

(25) Filing Language: English

(26) Publication Language: English

(30) Priority Data:
63/521,309 15 June 2023 (15.06.2023) US
63/548,418 14 November 2023 (14.11.2023) US

(71) Applicant: **NORTHWESTERN UNIVERSITY** [US/US]; 633 Clark Street, Evanston, Illinois 60208 (US).

(72) Inventors: **ROGERS, John A.**; 1236 Greenwood Avenue, Wilmette, Illinois 60091 (US). **TZAVELIS, Andreas**; 633 Clark Street, Evanston, Illinois 60208 (US). **TRUEB, Jacob**; 633 Clark Street, Evanston, Illinois 60208 (US). **FRANKLIN, Daniel**; 633 Clark Street, Evanston, Illinois 60208 (US).

(74) Agent: **XIA, Tim Tingkang**; P.O. Box 55874, Boston, Massachusetts 02205 (US).

(81) Designated States *(unless otherwise indicated, for every kind of national protection available)*: AE, AG, AL, AM, AO, AT, AU, AZ, BA, BB, BG, BH, BN, BR, BW, BY, BZ, CA, CH, CL, CN, CO, CR, CU, CV, CZ, DE, DJ, DK, DM, DO, DZ, EC, EE, EG, ES, FI, GB, GD, GE, GH, GM, GT, HN, HR, HU, ID, IL, IN, IQ, IR, IS, IT, JM, JO, JP, KE, KG, KH, KN, KP, KR, KW, KZ, LA, LC, LK, LR, LS, LU, LY, MA, MD, MG, MK, MN, MU, MW, MX, MY, MZ, NA, NG, NI, NO, NZ, OM, PA, PE, PG, PH, PL, PT, QA, RO,

(54) Title: MULTI-NODAL PHYSIOLOGICAL MONITORING SYSTEM UTILIZING MULTISPECTRAL PHOTOPLETHYSMOGRAPHY FOR ADVANCED HEMODYNAMIC CLASSIFICATION AND APPLICATIONS THEREOF

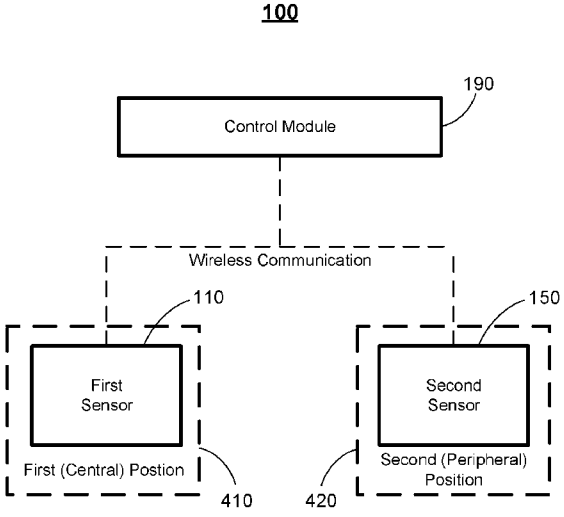


FIG. 1

(57) Abstract: This invention relates to multi-nodal physiological monitoring systems and methods for measuring physiological parameters of a living subject, and applications of the same. Specifically, the system includes a central sensor to be disposed at a central position, such as a chest area, to measure electrocardiogram (ECG) and mechano-acoustic (MA) signals. At least one multi-spatial, multi-wavelength photoplethysmography (MWPPG) sensor is disposed at the central position or a peripheral position, such as a finger, of the living subject to acquire cardiac and vascular signals. The central sensor and the at least one MWPPG sensor may communicate and time-synchronize with each other wirelessly, and the ECG and MA signals from the central sensor and the cardiac and vascular signals from the at least one MWPPG sensor are processed to simultaneously extract hemodynamic metrics and local vascular metrics.

WO 2024/259360 A1

[Continued on next page]

RS, RU, RW, SA, SC, SD, SE, SG, SK, SL, ST, SV, SY, TH, TJ, TM, TN, TR, TT, TZ, UA, UG, US, UZ, VC, VN, WS, ZA, ZM, ZW.

(84) **Designated States** *(unless otherwise indicated, for every kind of regional protection available)*: ARIPO (BW, CV, GH, GM, KE, LR, LS, MW, MZ, NA, RW, SC, SD, SL, ST, SZ, TZ, UG, ZM, ZW), Eurasian (AM, AZ, BY, KG, KZ, RU, TJ, TM), European (AL, AT, BE, BG, CH, CY, CZ, DE, DK, EE, ES, FI, FR, GB, GR, HR, HU, IE, IS, IT, LT, LU, LV, MC, ME, MK, MT, NL, NO, PL, PT, RO, RS, SE, SI, SK, SM, TR), OAPI (BF, BJ, CF, CG, CI, CM, GA, GN, GQ, GW, KM, ML, MR, NE, SN, TD, TG).

Published:

— *with international search report (Art. 21(3))*

— *before the expiration of the time limit for amending the claims and to be republished in the event of receipt of amendments (Rule 48.2(h))*

MULTI-NODAL PHYSIOLOGICAL MONITORING SYSTEM UTILIZING MULTISPECTRAL PHOTOPLETHYSMOGRAPHY FOR ADVANCED HEMODYNAMIC CLASSIFICATION AND APPLICATIONS THEREOF

CROSS-REFERENCE TO RELATED APPLICATIONS

This PCT application claims priority to and the benefit of U.S. Provisional Patent Application Serial No. 63/521,309, which was filed June 15, 2023, and U.S. Provisional Patent Application Serial No. 63/548,418, which was filed November 14, 2023. The content of each of the above-identified applications is incorporated herein by reference in its entirety.

FIELD OF THE INVENTION

The present invention relates generally to healthcare and vital sign monitoring, and more particularly to a multi-nodal physiological monitoring system utilizing multispectral photoplethysmography for advanced hemodynamic classification of a living subject, and applications of the same.

BACKGROUND OF THE INVENTION

The background description provided herein is for the purpose of generally presenting the context of the invention. The subject matter discussed in the background of the invention section should not be assumed to be prior art merely as a result of its mention in the background of the invention section. Similarly, a problem mentioned in the background of the invention section or associated with the subject matter of the background of the invention section should not be assumed to have been previously recognized in the prior art. The subject matter in the background of the invention section merely represents different approaches, which in and of themselves may also be inventions. Work of the presently named inventors, to the extent it is described in the background of the invention section, as well as aspects of the description that may not otherwise qualify as prior art at the time of filing, are neither expressly nor impliedly admitted as prior art against the invention.

Comprehensive cardiovascular health monitoring represents a challenging goal in medical practice and personal health management. Assessment of cardiopulmonary function is essential in the diagnosis and management of physiologic insufficiency and decompensation in life-threatening conditions such as circulatory shock. This hemodynamic evaluation involves

assessment of volume status (distributive), cardiac function (cardiogenic), and vascular tone (vasogenic) factors to target treatment plans. The simplest methods rely on physical exams, vital signs, and blood pressure (BP) measurements. In most cases, however, these assessments are intermittently captured and only provide a partial view of hemodynamic status, especially when signs change rapidly, overlap, or are obscured by physiologic compensation.

BP, the most widely studied cardiovascular parameter, represents only a single marker of hemodynamic health. BP is the product of the ability of the heart to generate blood flow, cardiac output (CO), against the resistance of the body's vascular beds, systemic vascular resistance (SVR). Dynamic changes in CO/SVR balance may mask changes in BP, complicating the identification of abnormal states that require intervention. In complex and severe cases which are unresponsive to first line treatments, guideline-directed management still recommends invasive hemodynamic monitoring, including arterial pressure catheters for continuous BP measurement and pulmonary artery catheterization for the estimation of CO. Estimates of SVR follow from the division of mean arterial BP by CO. Currently, these invasive measurements are not recommended for non-critical care patients or outpatients due to significant infection/trauma risks, requirement of specially trained personnel, and the physically limiting nature of these interventions. Studies in selected heart failure patients show ambulatory measurements from implantable pulmonary artery pressure sensors reduce hospitalizations, however the most recent guideline consensus remains uncertain on these benefits.

Therefore, a heretofore unaddressed need exists in the art to address the aforementioned deficiencies and inadequacies.

SUMMARY OF THE INVENTION

In one aspect, the invention relates to a multi-nodal physiological monitoring system for measuring physiological parameters of a living subject. In one embodiment, the system includes: a central sensor configured to be disposed at a central position of the living subject to measure electrocardiogram (ECG) and mechano-acoustic (MA) signals; and at least one multi-spatial, multi-wavelength photoplethysmography (MWPPG) sensor configured to be disposed at the central position or a peripheral position of the living subject to acquire cardiac and vascular signals. The central sensor and the at least one MWPPG sensor are configured to communicate and time-synchronize wirelessly, and the ECG and MA signals from the central sensor and the cardiac and vascular signals from the at least one MWPPG sensor are processed to

simultaneously extract hemodynamic metrics and local vascular metrics.

Another aspect of the invention relates to a method of measuring physiological parameters of a living subject with a multi-nodal physiological monitoring system. In one embodiment, the method includes: disposing a central sensor at a central position of the living subject to measure multi-modal ECG and MA signals; disposing at least one MWPPG sensor at the central position or a peripheral position of the living subject to acquire cardiac and vascular signals; and communicating and time-synchronizing the central sensor and the at least one MWPPG sensor wirelessly to process the ECG and MA signals from the central sensor and the cardiac and vascular signals from the at least one MWPPG sensor to simultaneously extract hemodynamic metrics and local vascular metrics from the ECG and MA signals and the cardiac and vascular signals.

In one embodiment, the central position is a chest area of the living subject, and the peripheral position is a finger area, a wrist area or a limb area of the living subject.

In one embodiment, the system is configured to measure and classify physiologic changes associated with specific hemodynamic states based on a pulse arrival time (PAT), a pulse propagation time and heart rate (HR), wherein the arterial PWV is obtained through the PAT, and the arteriolar PWV is obtained through the pulse propagation time.

In one embodiment, the central sensor includes: an analog differential amplifier-filter configured to measure ECG signals; a temperature sensor configured to measure temperature; and a triaxial accelerometer configured to simultaneously measure seismocardiogram (SCG) signals, core body motion, vocal processes, and physical activity.

In one embodiment, the at least one MWPPG sensor includes: a temperature sensor configured to measure temperature; a multispectral photodiode; and a plurality of linear array of light emitting diodes (LEDs) configured to emit visible light and near-infrared (NIR) light. In one embodiment, the at least one MWPPG sensor further includes: a triaxial accelerometer configured to simultaneously measure SCG signals, core body motion, vocal processes, and physical activity.

In one embodiment, each of the central sensor and the at least one MWPPG sensor includes: a flexible printed circuit board (fPCB); a middle circuit board layer disposed on the fPCB, including a plurality of electronic components, and a plurality of flexible and stretchable interconnects electrically connected to different electronic components; and a top elastomeric encapsulation layer and a bottom elastomeric encapsulation layer sandwiching the middle circuit

board layer, wherein the bottom elastomeric encapsulation layer forms a tissue-facing surface attached to the living subject, and the top elastomeric encapsulation layer forms an environment-facing surface.

In one embodiment, the middle circuit board layer is formed by a foldable electronic board, and the plurality of electronic components and the plurality of flexible and stretchable interconnects are disposed on the foldable electronic board.

In one embodiment, each of the central sensor and the at least one MWPPG sensor is attached to a skin of the living subject through an adhesive layer.

In one embodiment, the adhesive layer is formed by a dual-sided silicone-acrylate adhesive, a transparent film adhesive, or a self-adhering wrap.

In one embodiment, each of the central sensor and the at least one MWPPG sensor further comprises an embedded power supply or a remote charging power supply.

In one embodiment, the living subject is a human subject or a non-human subject.

In a further aspect, a non-transitory tangible computer-readable medium storing instructions is provided, which, when executed by one or more processors, cause the method as described above to be performed.

These and other aspects of the present invention will become apparent from the following description of the preferred embodiment taken in conjunction with the following drawings, although variations and modifications therein may be affected without departing from the spirit and scope of the novel concepts of the invention.

BRIEF DESCRIPTION OF THE DRAWINGS

The accompanying drawings illustrate one or more embodiments of the invention and together with the written description, serve to explain the principles of the invention. Wherever possible, the same reference numbers are used throughout the drawings to refer to the same or like elements of an embodiment.

FIG. 1 schematically shows a functional block diagram of a multi-nodal physiological monitoring system according to certain embodiments of the present invention.

FIG. 2A schematically shows the combined hemodynamic sensor concepts and devices overview, where (a) shows mode of operation of the combined sensor system, combining multi-wavelength measurements, differential voltage measurements, and triaxial accelerometry from multiple wireless sensors coordinated wirelessly by a control module through BLE; (b) shows

simultaneous physiologic measurements of systemic and peripheral pulse wave velocities enabling, (c) shows determination of relative hemodynamic states in dimensions of clinically pertinent hemodynamic parameters of BP and vascular resistance; (d) shows an exploded render of the multispectral device with silicone encapsulation layers, flexible printed circuit board (fPCB) consisting of four islands separated via flexible serpentine interconnects, and support circuitry; and (e) shows a bottom view of the multi-wavelength sensor with multiple pairs of individually controllable broadband and NIR LEDs.

FIG. 2B schematically shows the combined hemodynamic sensor concepts and devices overview, where (a) shows a side-by-side view of two different form factors achievable by folding the fPCB; (b) shows the device placement as a finger wrap; (c) shows the mechanical twisting of the peripheral multiwavelength device in its short form; (d) shows a diagram indicating various possible placements of the devices and associated normalized waveforms, offset for clarity, from central and peripheral locations, and with both arterial dominated or capillary dominated vascular beds (with more details shown in FIG. 4); Obtained during deep breathing exercises, the signal contains both low frequency oscillations due to respiration and high-frequency oscillations due to the cardiac cycle; (e) shows the monochromator scan of an encapsulated device showing relative responsivity at 9 different wavelengths throughout the visible and NIR ranges as well as LED pair emittance spectrum (black); and (f) shows a diagram of the measurement principles showing simultaneous wavelength- and distance-based light paths through a photoacoustic tomography render of real human skin.

FIG. 3 shows stretchable and flexible platforms according to certain embodiments of the invention, where engineered serpentine interconnects which bridge ridged islands enables two device forms, a wrap-like device, or a smaller patch-like device.

FIG. 4 shows Pulse Waveforms by Location. Local variations in vascular organization, structure, branching, path length, hydrostatic pressure, and skin thickness among many other effects all can modify the shape of the pulse waveform, where it is shown how this variation manifests in multiwavelength measurements at various locations, from peripheral placements, (a) finger and (b) thumb, to central placements, (c) ear, and (d) forehead.

FIG. 5A shows Combined Hemodynamic Sensor System and Measurements with a data analysis pipeline for extraction of arteriolar pulse transit time, extracting capillary and arterial pulsations from six discrete wavelength channels and employing normalized, subsampled cross-correlation to extract arteriolar (MW) time delay.

FIG. 5B shows Combined Hemodynamic Sensor System and Measurements, where (a) shows a block diagram of the sensors and key components enabling cross-body, central-vs-peripheral measurements of different modalities; (b) shows an example of time-synchronized sensor waveforms from the electrocardiogram (ECG), z-axis accelerometer seismocardiography (SCG), and photoplethysmography (PPG), with key physiological time intervals of hemodynamic relevance indicated; (c) shows Bland-Altman Plots with bias (black dashed line) and +/-1.96 standard deviations (dashed gray lines, CI=Confidence Interval) for conventional vitals measurements of heart rate (HR); (d) shows respiration rate (RR) and (e) shows pulse oxygenation (SpO_2) against references: Finapres pulse rate is used for healthy subjects, HR, RR and SpO_2 references are extracted from the electronic medical record for all patients.

FIG. 6A shows Visual MW Delay Algorithm, where raw multi-wavelength data (leftmost plot) is bandpassed filtered 0.5Hz to 5Hz and each wavelength is individually normalized, 5s windows are extracted for further analysis (center plot). Zooming in to the rising edge of a pulse shows relative timing between individual wavelengths, with IR and red leading, followed by yellow, and the shorter blue-green wavelength cluster.

FIG. 6B shows Visual MW Delay Algorithm, where (a) shows the PCA scheme is visualized, showing two separate PCAs performed on each 5s window of data, one using all six wavelengths, and the other using only the shortest two, generally near-surface limited, wavelengths; (b) shows the waveforms, with the leftmost plot showing the raw amplitudes of the extracted principal components and decoupled arterial pulsation; (c) shows what can occur when the PCA is calculated over the course of an entire dataset rather than uniquely in every 5s window; and (d) shows that while the resulting calculation of time delay remains consistent, there is considerable blunting during periods of maximal delay, resulting in the conclusion that the data is more reliable when maximally and uniquely projected.

FIG. 7A shows PPG Signal to Noise Ratio (SNR) Calculation through one method, where the darker line shows the result of bandpass filtering this data from 0.5 Hz to 5 Hz and represents the heart rate signal, while the lighter line is the result of high-pass filtering with cutoff frequency of 5 Hz and represents noise, and the calculation for SNR results in 20.86 dB.

FIG. 7B shows PPG SNR Calculation through another method, where the power spectral density of the highpass filtered (0.5Hz and up) PPG data, calculated on groups of 1024 samples at 128 sample overlap with Hanning windowing, and the SNR calculation results in 20.49 dB.

FIG. 8 shows a Table of Measurement Trends by Hemodynamic Stimulus.

FIG. 9A shows Representative Hemodynamic Studies on Healthy Individuals with short term interleaved pressor tests, cycling through Valsalva maneuver, cold pressor test, and breath holding.

FIG. 9B shows Representative Hemodynamic Studies on Healthy Individuals with (a) a 20-minute heat exposure challenge via personal sauna, and (b) a 20-minute exercise bike session, showing drastic change in PAT mirroring the HR which returns to baseline.

FIG. 10 shows Post-surgical Monitoring, where a patient monitored for a 12-hour period post mitral valve repair was given intravenous (IV) epinephrine in response to postoperative hypotension noted in the electronic medical record (EMR).

FIG. 11 shows Hemodynamic Measurement Scatter Plots, where (a) shows a theoretical plot between peripheral resistance and BP, indicating hypothesized relationships of different hemodynamic stimuli; (b) shows a baseline subtracted scatter plots between HR (bpm), PAT (ms), MW Delay (ms) and Systolic/Diastolic BP (mmHg), with each sample color coded by stimulus as in (a); (c) shows a scatter plot of the MW Delay fold change on a logarithmic axis against BP, showcasing separation of stimuli into groupings in similar positions as (a), with kernel density estimates of distributions of these quantities outside each axis; (d) shows Letter-value plots of MW Delay measurements during each hemodynamic state.

FIG. 12A shows the full scatter matrix between sensor measured HR, PAT, and MW Delay with reference SBP and DBP for Scatter Plots and Correlations.

FIG. 12B shows heatmaps, separated by class and overall, of Pearson correlation coefficients calculated for all pairs of measurements.

FIG. 13A shows a confusion matrix of model predictions for Hemodynamic Classification, grouped by hemodynamic condition (quadrant on BP vs SVR axis).

FIG. 13B shows Hemodynamic Classification, where (a) shows the receiver operator characteristic curves; and (b) shows precision-recall curves for all hemodynamic state predictions (one vs. all) colored by the quadrants outlined in FIG. 2A(c) and highlighted micro-average curve in black.

FIG. 14A shows ROC and PRC curves of 5-fold Training and Testing for (a) Baseline and (b) Exercise-Active cases.

FIG. 14B shows ROC and PRC curves of 5-fold Training and Testing for (a) Sauna/Exercise-Post and (b) Cold Pressor/Breath Hold cases.

FIG. 14C shows ROC and PRC curves of 5-fold Training and Testing for (a) Surgical

Pressors case and (b) the micro-averaged overall curves.

FIG. 14D shows the mean results of the ROC and PRC curves of 5-fold Training and Testing.

FIG. 15 shows SHapely Additive exPlanations (SHAP).

FIG. 16 shows an exemplary Circuit Design and Board Layout, where (a) shows a circuit diagram for 4-layer flexible circuit board, and (b) shows a final assembled circuit before folding.

FIG. 17 shows the device encapsulation process, where (a) shows the encapsulation mold for the top layer; (b) shows the encapsulation mold for the bottom layer; (c) shows transparent windows are created in the bottom layer by removing any residual silicone and filling with Ecoflex 31 before placing the device and sensor head in place to cure; and (d) shows two device forms.

FIG. 18 shows the emission spectrum of the broadband white LED on (a) an unencapsulated device and (b) a fully encapsulated device, at different LED drive currents.

FIG. 19A shows Intermittent Sampling Mode and Location Comparison, where the location is on the thumb.

FIG. 19B shows Intermittent Sampling Mode and Location Comparison, where the location is on the wrist.

FIG. 20 shows a Table of MW Delay Comparisons by Stimulus.

DETAILED DESCRIPTION OF THE INVENTION

The invention will now be described more fully hereinafter with reference to the accompanying drawings, in which exemplary embodiments of the invention are shown. This invention may, however, be embodied in many different forms and should not be construed as limited to the embodiments set forth herein. Rather, these embodiments are provided so that this specification will be thorough and complete, and will fully convey the scope of the invention to those skilled in the art. Like reference numerals refer to like elements throughout.

The terms used in this specification generally have their ordinary meanings in the art, within the context of the invention, and in the specific context where each term is used. Certain terms that are used to describe the invention are discussed below, or elsewhere in the specification, to provide additional guidance to the practitioner regarding the description of the invention. For convenience, certain terms may be highlighted, for example using italics and/or quotation marks. The use of highlighting has no influence on the scope and meaning of a term;

the scope and meaning of a term are the same, in the same context, whether or not it is highlighted. It will be appreciated that same thing can be said in more than one way. Consequently, alternative language and synonyms may be used for any one or more of the terms discussed herein, nor is any special significance to be placed upon whether or not a term is elaborated or discussed herein. Synonyms for certain terms are provided. A recital of one or more synonyms does not exclude the use of other synonyms. The use of examples anywhere in this specification including examples of any terms discussed herein is illustrative only, and in no way limits the scope and meaning of the invention or of any exemplified term. Likewise, the invention is not limited to various embodiments given in this specification.

It will be understood that, as used in the description herein and throughout the claims that follow, the meaning of "a", "an", and "the" includes plural reference unless the context clearly dictates otherwise. Also, it will be understood that when an element is referred to as being "on" another element, it can be directly on the other element or intervening elements may be present therebetween. In contrast, when an element is referred to as being "directly on" another element, there are no intervening elements present. As used herein, the term "and/or" includes any and all combinations of one or more of the associated listed items.

It will be understood that, although the terms first, second, third, etc. may be used herein to describe various elements, components, regions, layers and/or sections, these elements, components, regions, layers and/or sections should not be limited by these terms. These terms are only used to distinguish one element, component, region, layer or section from another element, component, region, layer or section. Thus, a first element, component, region, layer or section discussed below could be termed a second element, component, region, layer or section without departing from the teachings of the invention.

Furthermore, relative terms, such as "lower" or "bottom" and "upper" or "top," may be used herein to describe one element's relationship to another element as illustrated in the figures. It will be understood that relative terms are intended to encompass different orientations of the device in addition to the orientation depicted in the figures. For example, if the device in one of the figures. is turned over, elements described as being on the "lower" side of other elements would then be oriented on "upper" sides of the other elements. The exemplary term "lower", can, therefore, encompasses both an orientation of "lower" and "upper," depending on the particular orientation of the figure. Similarly, if the device in one of the figures is turned over, elements described as "below" or "beneath" other elements would then be oriented "above" the

other elements. The exemplary terms “below” or “beneath” can, therefore, encompass both an orientation of above and below.

It will be further understood that the terms “comprises” and/or “comprising,” or “includes” and/or “including” or “has” and/or “having”, or “carry” and/or “carrying,” or “contain” and/or “containing,” or “involve” and/or “involving, and the like are to be open-ended, i.e., to mean including but not limited to. When used in this specification, they specify the presence of stated features, regions, integers, steps, operations, elements, and/or components, but do not preclude the presence or addition of one or more other features, regions, integers, steps, operations, elements, components, and/or groups thereof.

Unless otherwise defined, all terms (including technical and scientific terms) used herein have the same meaning as commonly understood by one of ordinary skill in the art to which this invention belongs. It will be further understood that terms, such as those defined in commonly used dictionaries, should be interpreted as having a meaning that is consistent with their meaning in the context of the relevant art and this specification, and will not be interpreted in an idealized or overly formal sense unless expressly so defined herein.

As used in this specification, “around”, “about”, “approximately” or “substantially” shall generally mean within 20 percent, preferably within 10 percent, and more preferably within 5 percent of a given value or range. Numerical quantities given herein are approximate, meaning that the term “around”, “about”, “approximately” or “substantially” can be inferred if not expressly stated.

As used in this specification, the term "chest" refers to a central location on the human body and is synonymous with thorax. Both the terms "chest" and "thorax" are interchangeable.

As used in this specification, the phrase “at least one of A, B, and C” should be construed to mean a logical (A or B or C), using a non-exclusive logical OR. As used herein, the term “and/or” includes any and all combinations of one or more of the associated listed items.

The description below is merely illustrative in nature and is in no way intended to limit the invention, its application, or uses. The broad teachings of the invention can be implemented in a variety of forms. Therefore, while this invention includes particular examples, the true scope of the invention should not be so limited since other modifications will become apparent upon a study of the drawings, the specification, and the following claims. For purposes of clarity, the same reference numbers will be used in the drawings to identify similar elements. It should be understood that one or more steps within a method may be executed in a different

order (or concurrently) without altering the principles of the invention.

As discussed above, studies in selected heart failure patients show ambulatory measurements from implantable pulmonary artery pressure sensors reduce hospitalizations, however the most recent guideline consensus remains uncertain on these benefits. Recent advances in wireless, skin-interfaced sensor technologies enable continuous collection of critical health parameters that greatly improve the ability to monitor patient status non-invasively, continuously and remotely. The latest devices support measurements of heart rate (HR), respiration rate, physical activity and blood oxygenation, in many cases with regulatory approvals for use in the hospital and at home, across a wide range of age groups. Unfortunately, estimation of BP using wearable cuffless technology remains challenging. The most common approach to estimating blood pressure using wearable technology is through pulse wave velocity (PWV), which relates the stiffness of the arteries to driving pressure through empirical calibrations based on the Moens-Korteweg and Hughes equations. PWV can be measured non-invasively across a known distance through the time delay between the electrocardiogram (ECG) R-peak or mechano-acoustic measurements of aortic valvular openings and specific features in peripheral photoplethysmogram (PPG) waveforms – known as pulse arrival time (PAT) and pulse transit time (PTT) respectively. While this approach has shown some promise, it does not account for dynamic changes in the underlying vessel bed that can occur during conditions such as physical exercise, administration of vasoactive pharmaceuticals, variations in ambient temperature, circadian rhythms, and other natural activities. PWV can be highly correlated with HR, and care must be taken to evaluate PWV measurements under variable conditions where HR and BP are not highly correlated to prevent confounding. Additionally, efforts pursuing non-invasive methods of continuous CO estimation include impedance cardiography or pulse waveform/pulse pressure analysis, but which suffer from similar assumptions, empirically derived models, confounders, or tedious and invasive calibration requirements similar to PWV measurements.

Beyond BP and CO, SVR measurements are difficult to measure directly, however recent work suggests that arteriolar state – the primary factor determining vascular resistance – can be captured by exploiting the wavelength-dependent penetration depth of light into the skin. Shorter wavelength, blue-green light interacts primarily with near-surface capillaries, while red-infrared light interacts with larger arteries in the subdermal plexus. Thus, by deconvolving arterial and capillary pulsations, it is possible to quantify pulse wave propagation from the subdermal plexus,

through arterioles, to near-surface capillaries. This arteriolar pulse propagation time, herein termed "MW Delay" due to the multi-wavelength method of extraction, is modulated by the variable arteriolar diameter elicited by constriction or dilation and is thus related to local vascular resistance.

Tracking these factors continuously and remotely with discrete wearables provides a promising path towards personalized, outcome-oriented healthcare management. Beyond healthcare, wireless, non-invasive hemodynamic measurements may have implications in physical performance assessments such as exercise readiness and recovery, or cognitive stress management. These considerations suggest that a multi-modal approach is favorable over a single parameter model, to disentangle complex physiological interactions as the body experiences hemodynamic change.

In view of this, one aspect of the invention relates to a multi-nodal physiological monitoring system for measuring physiological parameters of a living subject. Specifically, the multi-nodal wireless, skin-interfaced system is capable of continuous hemodynamic classification within the BP, CO, and SVR coordinate space. The approach combines a unique, peripherally worn multi-spectral, multi-spatial photoplethysmography (MWPPG) sensor with a chest worn device that captures signals related to cardiac activity. By uniting (i) conventional time-synchronized PAT measurements, (ii) a correlate of local vascular resistance through MW delay, and (iii) heart rate (HR), this wearable system can measure and classify physiologic changes associated with specific hemodynamic states, thus delivering clinically actionable information. Pilot studies reveal the impact of short-term hemodynamic stimuli on healthy and hypertensive individuals through cold pressor tests, breath holds, Valsalva maneuvers, exercise, and full body heat exposure, as well as longer-term effects of pharmacological intervention during post-surgical recovery within a cardiothoracic intensive care unit. These hemodynamic modulating activities elicit disparate responses in BP/SVR/CO, where the heart both drives and reacts to conditions throughout a full range of realistic, natural scenarios.

FIG. 1 schematically shows a functional block diagram of a multi-nodal physiological monitoring system according to certain embodiments of the present invention. It should be noted that the system as shown in FIG. 1 is an exemplary system, and is not intended to limit the apparatus for measuring physiological parameters of a living subject. In one embodiment, the living subject is a human subject or a non-human subject.

As shown in FIG. 1, the exemplary system 100 includes a plurality of sensors 110 and

150, namely a first sensor 110 and a second sensor 150, and a control module 190 adapted in wireless communication with the sensors 110 and 150. The sensors 110 and 150 are time-synchronized and communicate with the control module 190 wirelessly and bidirectionally, and are respectively attached to the living subject. Specifically, the first sensor 110 is a central sensor configured to be disposed at a first (central) position 410 of the living subject, such as a chest area, a forehead area or an ear of the living subject, to measure multi-modal electrocardiogram (ECG) and mechano-acoustic (MA) signals, and the second sensor 150 is a peripheral multi-spatial photoplethysmography (MWPPG) sensor configured to be disposed at the first (central) position or a second (peripheral) position of the living subject, such as a finger area, a wrist area or a limb area, to acquire multi-modal cardiac and vascular signals. In certain embodiments, examples of the MA signals may include, without being limited to, seismocardiogram (SCG) signals. The control module 190 may be implemented by, for example, a microcontroller unit (MCU) that communicates and time-synchronizes with the central sensor 110 and the MWPPG sensor 150 wirelessly, and is used to manage and process the ECG and MA signals from the central sensor 110 and the cardiac and vascular signals from the MWPPG sensor 150 and to extract hemodynamic metrics and local vascular metrics, such as arterial pulse wave velocity (PWV) and arteriolar PWV, simultaneously from the ECG and MA signals and the cardiac and vascular signals obtained from the two sensors 110 and 150. Thus, the overall system is a multi-nodal, multi-modal system. In certain embodiments, instead of merely providing one MWPPG sensor 150, the system may include multiple MWPPG sensors 150.

In the embodiment as shown in FIG. 1, the control module 190 is provided to communicate and time synchronize with the central sensor 110 and the MWPPG sensor 150 wirelessly. In certain embodiments, it is possible that the system 100 is without the control module 190, and the central sensor 110 and the MWPPG sensor 150 may communicate and time-synchronize wirelessly in order to process the ECG and MA signals from the central sensor and the cardiac and vascular signals from the at least one MWPPG sensor to simultaneously extract the hemodynamic metrics and local vascular metrics.

In one embodiment, the system is configured to measure and classify physiologic changes associated with specific hemodynamic states based on a pulse arrival time (PAT), a pulse propagation time and heart rate (HR), wherein the arterial PWV is obtained through the PAT, and the arteriolar PWV is obtained through the pulse propagation time. In certain

embodiments, the system may measure and classify the physiologic changes using additional signals, such as pre-ejection period (PEP), left ventricular ejection time (LVET) and other signals based on the data streams.

In one embodiment, the central sensor includes: an analog differential amplifier-filter configured to measure ECG signals; a temperature sensor configured to measure temperature; and a triaxial accelerometer configured to simultaneously measure SCG signals, core body motion, vocal processes, and physical activity.

In one embodiment, the MWPPG sensor includes: a temperature sensor configured to measure temperature; a multispectral photodiode; and a plurality of linear array of light emitting diodes (LEDs) configured to emit visible light and near-infrared (NIR) light. In one embodiment, the MWPPG sensor further includes: a triaxial accelerometer configured to simultaneously measure multi-modal SCG, core body motion, vocal processes, and physical activity.

In one embodiment, each of the central sensor and the MWPPG sensor includes: a flexible printed circuit board (fPCB); a middle circuit board layer disposed on the fPCB, including a plurality of electronic components, and a plurality of flexible and stretchable interconnects electrically connected to different electronic components; and a top elastomeric encapsulation layer and a bottom elastomeric encapsulation layer sandwiching the middle circuit board layer, wherein the bottom elastomeric encapsulation layer forms a tissue-facing surface attached to the living subject, and the top elastomeric encapsulation layer forms an environment-facing surface.

In one embodiment, the middle circuit board layer is formed by a foldable electronic board, and the plurality of electronic components and the plurality of flexible and stretchable interconnects are disposed on the foldable electronic board.

In one embodiment, each of the central sensor and the MWPPG sensor is attached to a skin of the living subject through an adhesive layer.

In one embodiment, the adhesive layer is formed by a dual-sided silicone-acrylate adhesive, a transparent film adhesive, or a self-adhering wrap.

In one embodiment, each of the central sensor and the MWPPG sensor further comprises an embedded power supply or a remote charging power supply.

In one embodiment, each of the each of the central sensor and the MWPPG sensor is in wireless communication with the control module via a near field communication (NFC) protocol,

or Bluetooth protocol.

In certain embodiments, the system 100 as shown in FIG. 1 may be in the form of a mobile or wearable device or platform, which increases the flexibility of the apparatus.

Another aspect of the invention relates to a method of measuring physiological parameters of a living subject with a multi-nodal physiological monitoring system. In one embodiment, the method includes: disposing a central sensor at a first central position of the living subject to measure electrocardiogram (ECG) and seismocardiogram (SCG) signals; disposing a peripheral multi-spatial photoplethysmography (MWPPG) sensor at a second peripheral position of the living subject to acquire multi-modal cardiac signals; and providing a control module, communicating and time-synchronizing with the central sensor and the peripheral MWPPG sensor wirelessly, to manage and process the ECG and SCG signals from the central sensor and the multi-modal cardiac signals from the peripheral MWPPG sensor and to extract arterial pulse wave velocity (PWV) and arteriolar PWV simultaneously from the ECG and SCG signals and the multi-modal cardiac signals.

These and other aspects of the invention are further described below. Without intent to limit the scope of the invention, exemplary instruments, apparatus, methods and their related results according to the embodiments of the invention are given below. Note that titles or subtitles may be used in the examples for convenience of a reader, which in no way should limit the scope of the invention. Moreover, certain theories are proposed and disclosed herein; however, in no way they, whether they are right or wrong, should limit the scope of the invention so long as the invention is practiced according to the invention without regard for any particular theory or scheme of action.

EXAMPLES

As discussed above, the system as discussed above has two sensors, including a central, chest-worn sensor for ECG and SCG measurements along with a MWPPG sensor for simultaneous acquisition of multi-modal cardiac signals. the combined hemodynamic sensor concepts and devices overview, where (a) shows mode of operation of the combined sensor system, combining multi-wavelength measurements, differential voltage measurements, and triaxial accelerometry from multiple wireless sensors coordinated wirelessly by a control module through BLE; (b) shows simultaneous physiologic measurements of systemic and peripheral pulse wave velocities enabling, (c) shows determination of relative hemodynamic states in

dimensions of clinically pertinent hemodynamic parameters of BP and vascular resistance; (d) shows an exploded render of the multispectral device with silicone encapsulation layers, flexible printed circuit board (fPCB) consisting of four islands separated via flexible serpentine interconnects, and support circuitry; (e) shows a bottom view of the multi-wavelength sensor with multiple pairs of individually controllable broadband and NIR LEDs. Specifically, FIG. 2A(a) showcases the ECG/SCG device and MWPPG communicating wirelessly to a central control module with custom software that coordinates time synchronization and manages data transfer through the Bluetooth® Low Energy™ (BLE) protocol. The advantage of this combined approach is that both arterial PWV, corresponding to systemic factors, and arteriolar PWV, corresponding to local vascular dynamics, can be extracted simultaneously (see FIG. 2A(b)). Arterial stiffness and BP primarily determine the systemic PWV, measured by PAT, while the arteriolar resistance primarily determines the arteriolar PWV, measured by MW Delay. FIG. 2A(c) outlines key clinical entities on the BP vs peripheral vascular resistance axis relative to the resting state. Even with perfect measurement, BP alone cannot differentiate these conditions – a multiparameter approach is required. By measuring arteriolar PWV in addition to systemic PWV and HR, it may be possible to disentangle these states.

Device Design

The combined central-peripheral system uses a Bluetooth Low Energy (BLE) enabled System-on-a-Chip (SoC) to control data collection and local data storage, and to ensure inter-device time synchronization and coordinated data transfer. The chest device, which extends designs reported previously for neonatal monitoring, incorporates an analog differential amplifier-filter with filters tuned to the 0.5Hz-80Hz range for ECG measurements, a temperature sensor, and a triaxial accelerometer that simultaneously measures SCG, core body motion, vocal processes, and physical activity.

The peripheral device represents a unique enabling component of this system. This technology incorporates the same temperature sensor and accelerometer as the chest device, for rejecting motion artifacts, determining orientation, and recording physical activity. The key feature is a multispectral photodiode and linear array of light emitting diodes (LEDs) that emit across the visible and near-infrared region of the spectrum. FIG. 2A(d) shows an exploded view that highlights these components, along with power management circuits and sub-systems for wireless charging of a small lithium-polymer battery, all separated into four mechanically

isolated islands. The enclosure exploits a medical grade silicone elastomer, with transparent windows for the four pairs of broadband white and near-infrared (NIR) LEDs and the multispectral photodiode, as shown in FIG. 2A(e), where source-detector distances are 3mm, 6.5mm, 10 mm, and 13.5mm, and time-sequential LED sequencing allows for spatially resolved spectroscopy useful in tissue oximetry.

FIG. 2B schematically shows the combined hemodynamic sensor concepts and devices overview. Specifically, FIG. 2B(a) shows a side-by-side view of two different form factors achievable by folding the fPCB; FIG. 2B (b) shows the device placement as a finger wrap; and FIG. 2B(c) shows the mechanical twisting of the peripheral multiwavelength device in its short form. FIG. 3 shows stretchable and flexible platforms according to certain embodiments of the invention, where engineered serpentine interconnects which bridge ridged islands enables two device forms, a wrap-like device, or a smaller patch-like device. As shown in FIG. 3, panels (a)-(e) show the wrap-style device experiencing various levels of strain from top and bottom views while fully functioning, as well as (f) twisting; and panel (g) shows the smaller patch device at rest, (h) stretching and (i) twisting. As illustrated in FIG. 2B(a)-(c) and FIG. 3, serpentine interconnects greatly improve device flexibility and they mechanically isolate sensitive components from the battery, radio unit and other hardware.

FIG. 2B(d) shows a diagram indicating various possible placements of the devices and associated normalized waveforms, offset for clarity, from central and peripheral locations, and with both arterial dominated or capillary dominated vascular beds (with more details shown in FIG. 4). FIG. 4 shows Pulse Waveforms by Location. Local variations in vascular organization, structure, branching, path length, hydrostatic pressure, and skin thickness among many other effects all can modify the shape of the pulse waveform, where it is shown how this variation manifests in multiwavelength measurements at various locations, from peripheral placements, (a) finger and (b) thumb, to central placements, (c) ear, and (d) forehead. As shown in FIG. 4, these waveforms are collected simultaneously at these multiple locations. All waveforms are filtered with .5-5Hz bandpass filters and normalized, with an offset added to each wavelength for visual separation. Pulses from the 555nm channel are shown on the right to emphasize the morphological difference is pulse shape at these different locations. Peripheral pulses at the fingers tend to have sharper peaks and a more prominent dicrotic notch likely owing to the more direct, large vessel path to these vascular beds, while centrally measured pulses at the forehead and ear tend to be rounded, as they travel a more circuitous and branching route against gravity

to the generally capillary-dominated vasculature. Specifically, obtained during deep breathing exercises, the signal as shown in FIG. 2B(d) and FIG. 4 contains both low frequency oscillations due to respiration and high-frequency oscillations due to the cardiac cycle. This flexibility also allows for multiple final device forms via folding of the circuit before encapsulation to improve the fidelity of operation and to allow use on nearly any part of the body, from central locations such as the forehead or ear, to peripheral locations such as fingers or the wrist, as shown in FIG. 2B(d). Signals provide information that is specific to the characteristics of regional vascular beds. For example, the earlobe and forehead yield rounded, capillary-like pulse waveforms without a strong dicrotic notch, while the finger produces sharp pulse onsets and a pronounced dicrotic notch presence due to increased wave reflections from branching arterial trees and larger vessels near the surface. Additionally, low frequency oscillations due to respiration can be seen overlayed with high-frequency oscillations due to the cardiac cycle.

Sensor Modalities and Analysis

FIG. 2B(e) shows the monochromator scan of an encapsulated device showing relative responsivity at 9 different wavelengths throughout the visible and NIR ranges as well as LED pair emittance spectrum (black); and FIG. 2B(f) shows a diagram of the measurement principles showing simultaneous wavelength- and distance-based light paths through a photoacoustic tomography render of real human skin. The unique combination of broadband LEDs and a multispectral photodiode enables simultaneous spectroscopic measurements at 9 discrete wavelength bands in the visible-NIR range, shown in FIG. 2B(e) and the illustration of FIG. 2B(f). Longer wavelengths of light have lower tissue absorption and thus travel deeper into and further across the tissue before scattering, reflection and capture by the photodiode. Similarly, as the distance between the LED pairs and the multispectral photodiode increases, this effective penetration depth also increases. The multi-wavelength approach emphasizes near-surface depth dependence. By contrast, the source-detector distance approach allows greater depths of penetration for longer wavelengths, as is useful for spatially resolved tissue oxygenation measurements. The source-detector distances are 3mm, 6.5mm, 10mm, and 13.5mm, respectively.

For measurement of MW Delay, the device operates at a fixed LED with source-detector distance of 3mm, and with six wavelengths of 480nm, 515nm, 555nm, 590nm, 680nm, and 900nm. These wavelengths penetrate the tissue to depths of approximately 0.3mm, 0.4mm,

0.5mm, 0.6mm, 1.0mm, 2.3mm, and 1.8mm, respectively, at 50% fluence, each with sampling rates of 100Hz. The pulsations captured at each wavelength integrate contributions to the respective characteristic depths. FIG. 5A shows Combined Hemodynamic Sensor System and Measurements with a data analysis pipeline for extraction of arteriolar pulse transit time, extracting capillary and arterial pulsations from six discrete wavelength channels and employing normalized, subsampled cross-correlation to extract arteriolar (MW) time delay. FIG. 6A shows Visual MW Delay Algorithm, where raw multi-wavelength data (leftmost plot) is bandpassed filtered 0.5Hz to 5Hz and each wavelength is individually normalized, 5s windows are extracted for further analysis (center plot). Zooming in to the rising edge of a pulse shows relative timing between individual wavelengths, with IR and red leading, followed by yellow, and the shorter blue-green wavelength cluster. FIG. 6B shows Visual MW Delay Algorithm, where (a) shows the PCA scheme is visualized, showing two separate PCAs performed on each 5s window of data, one using all six wavelengths, and the other using only the shortest two, generally near-surface limited, wavelengths; (b) shows the waveforms, with the leftmost plot showing the raw amplitudes of the extracted principal components and decoupled arterial pulsation; (c) shows what can occur when the PCA is calculated over the course of an entire dataset rather than uniquely in every 5s window; and (d) shows that while the resulting calculation of time delay remains consistent, there is considerable blunting during periods of maximal delay, resulting in the conclusion that the data is more reliable when maximally and uniquely projected.

Specifically, FIG. 5A shows the high-level approach for extracting pure arterial and capillary contributions from a wavelength depth-dependent mixture model, while FIG. 6A covers this process at each step visually. In each 5 second window, a unique principal component analysis (PCA) of the normalized, 0.5Hz-5Hz bandpassed pulsatile waveforms at the two shallowest penetrating wavelengths, 480nm and 515nm, enables extraction of these near-surface, capillary-dominated pulsations. As shown in FIG. 6B(a), a single primary component is extracted from the former, representing a superposition of arterial and capillary pulsations, while two components are extracted from the latter, representing capillary pulsations and non-pulsatile noise, respectively. Subtraction of the capillary component from the superposed arterial-capillary component isolates the arterial pulse. These waveforms are plotted in FIG. 6B(b), with the leftmost plot showing the raw amplitudes of the extracted principal components and decoupled arterial pulsation. Normalization of each of these waveforms generates the center plot – note the black trace is entirely composed of non-pulsatile noise (second component of the near-

surface PCA). The rightmost plot shows zooming in at the rising edge of one of the pulsations, showing the leading arterial pulse, followed by the superposed arterial-capillary pulse, and finally the capillary pulse. Below this plot is a plot from trough to peak of a single pulse with a gray arrow indicating the earlier onset of the red arterial pulse at the onset of the beat, matching physiologic expectations. The plots in FIG. 6B(c) show what can occur when the PCA is calculated over the course of an entire dataset rather than uniquely in every 5s window. Large motion artifacts in other parts of the dataset or simply pulse morphology changes elicited with each hemodynamic stimulus can throw off the principal components, leading to leakage of pulsatile information into the noise component. While the significance of this finding remains under investigation, the bottom line is that in FIG. 6B(d), while the resulting calculation of time delay remains consistent, there is considerable blunting during periods of maximal delay, resulting in the conclusion that the data is more reliable when maximally and uniquely projected. All wavelengths contain a component of near-surface capillary pulsation, but yellow to NIR wavelengths also interact with arterioles and larger arteries. Calculation of the PCA uniquely at each window prevents gross motion artifacts or local variations in pulse morphology to influence calculations in other windows, shown visually in FIG. 6B(c) and (d). The first principal component of the short wavelengths represents pulsatile capillary blood volume changes, while the second principal component arises from motion artifacts. The first principal component of a separately calculated PCA of the normalized pulsatile waveforms at all available wavelengths extracts a superposed capillary-arterial pulse, from which the blue-green capillary pulse can be subtracted to isolate arterial pulsation. These pure arterial pulsations and pure capillary pulsations are cross-correlated with sub-sample interpolation. The delay at maximum correlation corresponds to the arteriolar pulse transit time (MW Delay).

FIG. 5B shows Combined Hemodynamic Sensor System and Measurements, where (a) shows a block diagram of the sensors and key components enabling cross-body, central-vs-peripheral measurements of different modalities; (b) shows an example of time-synchronized sensor waveforms from the electrocardiogram (ECG), z-axis accelerometer seismocardiography (SCG), and photoplethysmography (PPG), with key physiological time intervals of hemodynamic relevance indicated; (c) shows Bland-Altman Plots with bias (black dashed line) and +/-1.96 standard deviations (dashed gray lines, CI=Confidence Interval) for conventional vitals measurements of heart rate (HR); (d) shows respiration rate (RR) and (e) shows pulse oxygenation (SpO_2) against references: Finapres pulse rate is used for healthy subjects, HR, RR

and SpO_2 references are extracted from the electronic medical record for all patients. Specifically, a block diagram of the combined sensor system appears in FIG. 5B(a). The chest device captures single-lead ECG and triaxial accelerometry signals at sampling rates of 1kHz and up to 3.3kHz respectively. The green wavelength data from the MWPPG device yields the pulse rate. These three signals (FIG. 5B(b)) enable comparison of cardiac intervals known to be related to cardiovascular function, including the electromechanical delay/pre-ejection period (PEP), systolic/diastolic time intervals (Left Ventricular Ejection Time, LVET), pulse arrival time (PAT), and pulse transit time (PTT). Measurements of heart rate (HR), respiration rate (RR) and 2-wavelength (red-IR) pulse oxygenation (SpO_2) follow from MWPPG data, consistent with reference measurements as summarized in FIG. 5B(c)-(e). The signal to noise ratio (SNR) of the MWPPG device is 20.49 dB during hemodynamic pressors and calculated in FIG. 7B. Specifically, as shown in FIG. 7A and FIG. 7B, the SNR of the MWPPG device is calculated through two methods. FIG. 7A shows PPG SNR Calculation through one method, where the darker line shows the result of bandpass filtering this data from 0.5 Hz to 5 Hz and represents the heart rate signal, while the lighter line is the result of high-pass filtering with cutoff frequency of 5 Hz and represents noise. As shown in FIG. 7A, the root-mean-squared (RMS) of the PPG signal is 5.41 au while the RMS of the noise is 0.49 au, shown as two lines, respectively. The calculation for SNR in FIG. 7A follows below and results in 20.86 dB. FIG. 7B shows PPG SNR Calculation through another method, where the power spectral density of the highpass filtered (0.5Hz and up) PPG data, calculated on groups of 1024 samples at 128 sample overlap with Hanning windowing. As shown in FIG. 7B, the spectral power density is summed within a 0.5 Hz to 5 Hz band and averaged across time resulting in 273.23 au2, and the spectral power density is then summed for frequencies higher than 5 Hz and averaged across time to give 2.44 au2. The SNR calculation in FIG. 7B then follows as below to result in 20.49 dB. For both, the raw PPG data from FIG. 9(a) is averaged over all wavelength channels.

Hemodynamic Experiments

A set of experiments are chosen which elicit distinct hemodynamic responses within the BP-SVR-CO coordinate space and target separate BP regulatory mechanisms. Pilot studies with specific hemodynamic stimuli protocols produced data from healthy and hypertensive subjects with reference BP measurements provided by a volume clamp-based continuous non-invasive arterial BP monitor. Examination of the effects of pharmaceutical modulation focuses on patients

recovering in the cardiothoracic intensive care unit following mitral valve repair who required norepinephrine or epinephrine as standard clinical intervention in the immediate post-operative period in response to hypotension. Medical record data on medications, vital sign measurements, and laboratory values provide reference information for these patients. FIG. 8 shows a Table of Measurement Trends by Hemodynamic Stimulus. Specifically, the Table as shown in FIG. 8 displays characteristic changes relative to baseline across these experiments. As shown in FIG. 8, direction of changes in reference values and sensor measurements for each hemodynamic state relative to a resting baseline value for the dataset. Double arrows indicate significant changes. For dynamic events, the greatest direction of change is provided and phasing is ignored.

FIG. 9A shows a representative dataset on a healthy subject during cycles of interleaved, short-term stimuli to modulate BP in contrasting ways: Valsalva maneuvers, cold pressor tests, and breath holds. FIG. 9B shows Representative Hemodynamic Studies on Healthy Individuals with (a) a 20-minute heat exposure challenge via personal sauna, and (b) a 20-minute exercise bike session, showing drastic change in PAT mirroring the HR which returns to baseline. As shown in FIGS. 9A and 9B, the presentation includes changes in HR, PAT, and MW Delay alongside reference measurements of BP, demonstrating measurement repeatability. As shown in FIG. 9A, a consistent rise in MW Delay signal during ice bath exposure precedes a complementary rise in BP, indicating MW Delay is measuring a driving force inducing BP change. Conversely, alignment of MW Delay increase with BP in Valsalva phases II/III and breath holds indicates measurement of the reverse scenario – a compensatory, sympathetic vasoactive response to stimulus.

Valsalva

The Valsalva maneuver elicits a classical four-stage BP response as thoracic pressure is increased, held, and released. Because BP in this case is externally mediated and the heart reacts to baroreceptor stimulation, HR varies inversely with BP. PAT also exhibits an inverse response to BP as expected from theory. The response does not, however, track perfectly with BP, likely due to uneven central-peripheral pressure differential among other vasomotor compensatory effects. MW Delay, in contrast, exhibits a variable increase during Valsalva phase II which amplifies each repeated cycle associated with the time duration of the individual Valsalva maneuvers. Peripheral vasoconstriction is known to occur in response to decreased pulse pressure; the longer a Valsalva is held, the longer the body compensates for the decreased pulse

pressure.

Cold Pressor

Cold pressor challenges assess autonomic function, specifically sympathetic responses including vasoconstriction in the contralateral appendage. These tests elicit a gradual increase in BP due to sympathetic stimulation of both the heart and peripheral vessels. This dynamic process involves a rapid increase in HR followed by sustained oscillations throughout the challenge. An initial rapid decrease in PAT correlates with a small, sharp increase in BP, perhaps associated with bracing or initial shock. PAT then returns to values near the baseline, followed by a second, smaller decrease near the final seconds of cold exposure. This behavior contrasts with the expected decrease in PAT correlated to the increase in BP, likely due to autonomic driving forces that modify both arterial properties and cardiac contractility. MW Delay, on the other hand, exhibits a sharp increase, with oscillations that coincide with the period of cold exposure. Most importantly, these features exhibit a phase lead relative to the rise in BP, coinciding with the exposure to the cold-water bath. This suggests that vasoconstriction, not BP change, is indeed responsible for the increase in MW Delay.

Breath Hold

Breath holds include features of both intrathoracic pressure change, similar to the Valsalva maneuver, as well as peripheral vasoconstriction due to sympathetic reactions to hypoxia and hypercapnia. This complex response elicits a gradual rise in BP followed by a period of hypotension after breath release. The initial hold stage of this test leads to negligible changes in the HR and PAT. As the breath hold continues, however, it appears MW Delay changes remain in-phase with BP increase, contrary to the phase lead observations during the cold pressor test. Simultaneously, PAT remains constant until the BP begins to peak and the breath hold is released, exhibiting a phase lag to BP and MW Delay. The minimum value of PAT during the breath holds coincides with a return of MW Delay to baseline and corresponding decrease in BP. This phasing behavior between PAT and MW Delay with different driving forces of BP increase suggests a masking effect of arteriolar constriction on reflective-mode measurements of PAT or vice-versa.

Heat Exposure

During prolonged heat exposure, the increase in temperature leads to peripheral vasodilation and thus hypotension due to decreased peripheral resistance. To compensate, the HR increases, increasing CO to maintain BP. The experiments involve exposure of healthy subjects to elevated temperatures using a personal, portable sauna chamber for 20 minutes. The decrease in BP and increase in arterial compliance would, based on the empirical theory referenced previously, lead to a corresponding increase in PAT consistent with reported studies based on applanation tonometry. While this trend is modestly observed on initial exposure to heat, after profuse perspiration begins and BP decreases further around 10 minutes after entry into the sauna, the data from the system reported here and presented in FIG. 9B(a) indicates a consistent decrease in PAT is observed. Specifically, FIG. 9B(a) shows Representative Hemodynamic Studies on Healthy Individuals with a 20-minute heat exposure challenge via personal sauna. Note the loss of Finapres data during sauna entry, necessary due to disconnection of the wired system to pass the hand through a hole, while the wireless sensors experience no such limitation. Contrary to theory, PAT drops during this period, especially after profuse perspiration begins. MW Delay exhibits a small drop during heat exposure, which is partially reversed upon exiting the chamber. The MW Delay also moderately decreases in-phase with the PAT. As with the cold pressor test and breath hold challenges, this finding suggests that arteriolar pulse transit time may modulate PAT measured via reflective-mode PPG.

Physical Exercise

Exercise increases metabolic demand, and thus induces a corresponding increase in CO through an increase in HR and contractility. The result increases BP until the heat of increased metabolic demand begins to induce vasodilation. FIG. 9B(b) shows Representative Hemodynamic Studies on Healthy Individuals with a 20-minute exercise bike session, showing drastic change in PAT mirroring the HR which returns to baseline. As shown in FIG. 9B(b), MW Delay begins to drop only after the patient begins vasodilating, which occurs at the peak BP a few minutes after exercise starts. The delay remains low after exercise is complete and BP is still low despite the PAT return to baseline levels. Specifically, these processes lead to an immediate decrease in PAT and an increase in HR (12 min). Between 12 and 15 minutes, PAT exhibits an inverse relationship to BP, as expected by theory. At 15 minutes, the subject begins to perspire, and MW Delay begins to decrease in response to vasodilation. BP also begins to fall from its peak, but PAT and HR do not exhibit any similar inflection points. The decrease in MW

Delay after this point appears to balance the expected increase in PAT with the decrease in BP. For some period after exercise is complete, the vasodilation inferred by low MW Delay is maintained. Overall, HR and PAT exhibit a stronger correlation in this experiment than PAT and BP, while MW Delay trends add independent information.

Post-surgical Monitoring

Patients undergoing cardiothoracic surgery procedures can experience post-operative hypotension following cardiopulmonary bypass and surgical cardiac injury. Vasoconstrictive medications, such as phenylephrine, epinephrine, or norepinephrine delivered in the immediate post-operative period can help to maintain BP and prevent cardiogenic shock without stressing the heart. These medications increase end-organ perfusion by increasing peripheral resistance, corresponding to an increase in MW Delay relative to baseline.

FIG. 10 shows Post-surgical Monitoring, where a patient monitored for a 12-hour period post mitral valve repair was given intravenous (IV) epinephrine in response to postoperative hypotension noted in the electronic medical record (EMR). Hour 0 corresponds to start of surgical wound closure. IV epinephrine is started after initial rooming and assessment, and devices are placed shortly afterward. While the medication was tapered after 3 hours, MW Delay remained high in the setting of hypotension, suggesting elevated peripheral vascular tone. This lasted until the patient's BP recovered and the patient was able to feed, 10 hours after surgery completion. The results in FIG. 10 illustrate these trends for a representative patient during administration of intravenous epinephrine following a surgical procedure. After initial rooming and assessment concludes administration of epinephrine is appropriate, the medication is started and tapered as determined by regular clinical assessment and decision making. For the patient in FIG. 10, initial MW Delay was high and experienced a decline as epinephrine was withdrawn. In the following period, BP remains low for several hours, during which MW Delay experiences a resurgence and remains elevated relative to the period 11 hours after surgical closure, when BP recovers to pre-surgical levels and the patient has recovered from anesthesia.

Hemodynamic Classification

Complex homeostatic feedback loops connect BP and peripheral resistance. Depending on external stimuli or patient conditions, the equilibrium point between induced and compensatory changes in BP and peripheral resistance can shift relative to a defined resting state.

FIG. 11(a) shows a theoretical plot of expected clustering of hemodynamic states explored in this work relative to a central resting state. The four "core" examples that delineate this BP vs Resistance axis into quadrants relative to the resting state are 1) the cold pressor test and breath holding, which result in increased BP mediated by an increase in peripheral resistance associated with vasoconstriction, 2) physical exercise, which results in increased BP mediated by increases in cardiovascular stress and metabolic demand, while simultaneously decreasing peripheral resistance via vasodilation, 3) heat exposure via sauna, which results in decreased BP mediated by decreases in peripheral resistance associated with vasodilation, and 4) patients treated with post-surgical vasopressors in the setting of postoperative hypotension, where decreased BP is treated by medications which increase peripheral resistance. As illustrated by this plot, BP alone (horizontal axis) cannot distinguish all hemodynamic states. The pathophysiology that brings a patient into each of these quadrants is mediated by entirely different factors; identifying which quadrant a patient is in thus guides the choice of intervention to return to baseline.

FIG. 11(b) presents 2D projections of all data collected during this study separated by color for each hemodynamic stimulus. Each projection is across sensor-measured data (HR, PAT, and MW Delay) as well as reference Systolic and Diastolic BP (SBP, DBP). Specifically, FIG. 11(b) shows a baseline subtracted scatter plots between HR (bpm), PAT (ms), MW Delay (ms) and Systolic/Diastolic BP (mmHg), with each sample color coded by stimulus as in FIG. 11(a). To control for inter-subject variability, each data point is subtracted by the median of the baseline state, indicated by crosshairs.

FIGS. 12A and 12B shows Scatter Plots and Correlations, where the full scatter matrix between sensor measured HR, PAT, and MW Delay with reference SBP and DBP is shown in FIG. 12A. The diagonal is replaced with kernel density estimations of the distributions of measurements by hemodynamic stimulus. FIG. 12B shows heatmaps, separated by class and overall, of Pearson correlation coefficients calculated for all pairs of measurements. Importantly, the overall correlation between HR and BP is low, indicating that the chosen pressor experiments decouple this common interaction. Additionally, the very strong correlation between HR and PAT remains despite the previous finding that HR and BP is not correlated. This is a possible reason many BP prediction studies using only PAT measurements may suffer from confounding effects if studying interventions that do not effectively decouple HR from BP. Lastly, the addition of a metric like MW Delay which is at least partially independent to the effects of BP and HR (which itself is correlated with CO) is important to further improve the separability of these

hemodynamic states.

Several important observations can be inferred from the plots in FIG. 11(b) as well as quantitative Pearson correlations expanded upon in FIGS. 12A and 12B. First, the effect of the studied hemodynamic states on BP can be observed in the top-leftmost plot between SBP and DBP. While systolic and diastolic BP values are indeed highly correlated, some stimuli including active exercise and the Valsalva maneuvers exhibit more independence between SBP and DBP, conditions with significant pulse pressure variation. The next row emphasizes that across all the studied hemodynamic states, low correlation between HR and BP is achieved, which is often a significant confounder in hemodynamic studies especially studies of PWV. The following row further substantiates these findings, as PAT is not highly correlated to BP across all hemodynamic states but remains highly correlated with HR. The final row presents scatters of MW Delay against the reference BPs and sensor derived metrics, showing little to no correlation, as expected of a metric independent of CO or BP.

FIG. 11(c) shows a scatter plot of the MW Delay fold change on a logarithmic axis against BP, showcasing separation of stimuli into groupings in similar positions as FIG. 11(a), with kernel density estimates of distributions of these quantities outside each axis. Note the overlap of sauna and surgical pressor distributions on the BP axis, indicating two very different states are not adequately separable using BP alone, but with the addition of MW Delay begin to be distinguished. These plots illustrate the segregation of MW Delay and BP into discrete states similar to the theoretical peripheral resistance-BP axis. In particular, FIG. 11(c) plots the natural logarithm of the ratio of MW Delay values to baseline measurements (fold change) against reference SBP, replicating the theoretical plot in FIG. 11(a). MW Delay reliably identifies states of high and low peripheral resistance, regardless of BP. FIG. 11(d) shows Letter-value plots of MW Delay measurements during each hemodynamic state. The distributions of MW Delay for each hemodynamic stimulus are shown in FIG. 11(d) via letter-value box plots. In letter-value plots, each progressively smaller pair of boxes around the center value (median) represents a power of 2 smaller fraction of the data points, e.g. fourths, eighths, sixteenths, etc. Brunner-Munzel tests between each stimulus and the baseline distribution with significance are indicated by ns=not significant, ****=$p<.0001$. Brunner-Munzel tests for stochastic equality in non-normal, unequal-variance samples are performed for each stimulus against the baseline distribution. Overall observations of the clustering of sensor-measured parameters by hemodynamic stimuli in FIG. 11(b)-(d) suggest classification of various hemodynamic states is

possible using sensor data alone – without requiring direct measurements of absolute BP or SVR.

Based on visual inspection of the data in FIG. 11, a simple support vector classifier using the radial basis function kernel was chosen to separate the hemodynamic classes. The approach involves training on 20% of data for each condition, leaving the remaining 80% for testing and explainability evaluation. Data is not shuffled and is instead kept in chronological order to avoid contamination of the test set with similar sample points of the same subject performing the same activity used to train the model. The test set is thus maximally independent from the data used for training. Short-term dynamic stimuli, such as the Valsalva maneuver, are removed for this analysis. Stimuli are grouped into classification states based on their induced physiological response. Cold pressors and breath holds are combined into one group characterized by increased vascular resistance and BP, while sauna exposure and post-exercise are combined into one group characterized by decreased vascular resistance and BP. Support vector classifiers are defined as binary classifiers; to apply to a multiclass model, a separate model must be trained to classify each pair of classes. In this case, ${}_5C_2 = 10$ models are individually trained on the same subset of data, with the overall prediction deriving from a simple majority vote across all the one-vs-one models.

FIG. 13A shows the confusion matrix of the overall trained model when applied to the 80% left-out test data. Confusion occurs to a small degree between states where vasodilation is expected, or between states where vasoconstriction is expected, but not across different vascular states. For instance, confusion between exercise and sauna can be explained by varying exercise intensity, or conversely by the relatively high heart rates achieved in the sauna for some individuals. Confusion of cold pressor tests from baseline can be explained by some baseline measurements occurring in a cold environment, or that cold exposure causes a wave-like response of vasoconstriction followed by vasodilation which may vary substantially even with slight deviations in bath temperature. This phenomenon, in addition to the previously noted phase lead in MW Delay response and relative invariance in PAT may explain confusion of this dynamic stimulus. FIG. 13B(a) shows the receiver-operator characteristic (ROC) curves for each hemodynamic state for the left-out test data. Individual class ROC curves are computed in the one-vs-rest binary method, while the micro-average ROC combines these results accounting for class imbalance for an overall score. As shown in FIG. 13B(a), the areas under the curve values for receiver-operator characteristic curves include: Baseline = 0.96, Exercise = 0.98, Sauna = 0.93, Cold Pressor/Breath Hold = 0.98, Surgical Pressors = 1.0, and the micro-average AUROC

is 0.958. Precision-Recall curves are shown in FIG. 13B(b), where the areas under the curve values for precision-recall curves include: Baseline = 0.82, Exercise = 0.98, Sauna = 0.80, Cold Pressor/Breath Hold = 0.73, Surgical Pressors = 0.93, and the micro-averaged precision is 0.878.

FIGS. 14A-14D shows additional analysis repeating this training process on other folds in order to demonstrate model stability and generate an estimate of variance to the ROC curves. Specifically, FIGS. 14A-14D shows 5-fold Training and Testing, where the ROC and PRC curves for each training/testing fold are presented by individual class in FIGS. 14A(a) and (b), FIGS. 14B(a) and (b) and FIG. 14C(a), and FIG. 14C(b) shows the micro-averaged overall curves. FIG. 14D shows the mean results of the ROC and PRC curves of 5-fold Training and Testing. To demonstrate the stability of our training approach, the training/testing presented is a modified 5-fold cross-validation approach stratified by class. In the 5-fold Training and Testing, fold 0 corresponds the data presented in FIGS. 13A and 13B, which is training on the first 20% of data for each class and testing on the next 80%. The next fold uses the next chronological 20% of data for training, and test on the first 20% plus next 60%, and so on for the remaining folds. Chronological ordering is important to group repeated stimuli from the same subject together and minimize dependence between training and test sets.

Model interpretability and explainability is of critical importance in medical applications as models become increasingly complex. SHapely Additive exPlanations (SHAP) are a unified method of generating interpretable feature importance for each prediction. FIG. 15 shows SHapely Additive exPlanations (SHAP). SHAP analysis of model performed on left-out data, is performed and separated for each class. Error bars represent 95% confidence intervals. MW Delay appears to be uniquely informative in classifying conditions involving vasoconstriction, Cold Pressor/Breath Holds, and Surgical Pressors. As shown in FIG. 15, the SHAP analysis is applied to the trained support vector classifier model on up to 100 random examples of each hemodynamic class from the test set to generate an estimate of the importance of each input feature, MW Delay, PAT, or HR, in generating those predictions. MW Delay contributes most significantly toward predictions involving vasoconstriction. PAT, on the other hand, changes significantly in vasodilation, and is thus most helpful for prediction in those states. Overall, HR is the most important feature enabling identification of deviations from baseline, which is naturally in line with conventional clinical understanding.

Discussion

According to certain embodiments of the invention, a non-invasive multi-nodal, skin-interfaced, wireless system is provided for measurements of independent hemodynamic variables. The devices and subsequent classification method show promise in supplementing intermittent cuff-based home BP monitoring and invasive monitoring approaches currently reserved for patients with acute decompensated heart failure. The key technological advance is in the development of a multiwavelength device that mounts on a peripheral body location to measure a correlate of local vasoconstriction/dilation in arteriolar pulse transit time through MW Delay. Time synchronized operation with a chest unit that captures ECG and SCG waveforms leads to data streams with diverse information content. Data collected under a variety of scenarios indicate that the system yields consistent, repeatable results for individuals and between subjects over a large BP range. The largest and most predictable BP variability was elicited on healthy subjects undergoing specific tasks, while inpatient subjects were simply monitored during their clinical course without intervention beyond the standard of care. Results show that BP alone is not able to delineate all studied hemodynamic states; the addition of arteriolar PWV provided by MW Delay measurements are shown to be associated with vasoconstriction and dilation contribute significantly toward enabling hemodynamic classification.

Limitations of the invention include a relatively small number of subjects. Variations in skin thickness, melanin content, tolerance to pain and exercise, and vascular responsiveness are not able to be explicitly disentangled in this study and remain a subject of future research. Future work will include broader, outcome-oriented studies in diverse populations aimed at determining early warning and treatment thresholds. Additionally, the classification method incorporates only HR, PAT, and MW Delay. However, the sensor system enables collection of additional hemodynamic parameters such as pre-ejection period and left ventricular ejection time. Inclusion of these quantities may further extend the capabilities of classification and correlate to central cardiac function, including contractility and ejection fraction.

Together, the wireless monitoring system and classification method, provide objective information on the hemodynamic state of an individual, beyond that of BP alone. Detection of underlying BP regulatory mechanisms are of critical importance in guiding clinical decision making. With the ability to detect short-term hemodynamic responses to stimuli, medium-term compensatory responses, and longer-term trends, these technologies may provide early warning signs of hemodynamic decompensation warranting follow-up or intervention, as well as help

health-conscious individuals keep track of additional, meaningful vascular health parameters.

Methods

Device Fabrication

Circuit design with associated was performed on electronic design automation software (Eagle ver. 9.6.1, Autodesk) and outsourced for manufacturing on 4-layer flexible printed circuit board (fPCB) (PFC Flex, Inc). Key elements of the circuit include 1) Multispectral photodiode (AS7341, ams-OSRAM AG), 2) 4 pairs of broadband white LEDs and IR LEDs (L130-6580002011001, Lumileds , and SFH 4043, OSRAM), 3) power management electronics (BQ2510A, Texas Instruments), 4) NFC charging components (tuned coil and rectifier) to enable wireless charging, 5) a triaxial accelerometer (LSM6DSL, STMicroelectronics), 6) 8Gb NAND flash memory (MT29F8G08), 7) Bluetooth Low energy system-on-a-chip (ISP1807, Insight SiP), 8) passive components.

FIG. 16 shows an exemplary Circuit Design and Board Layout. Specifically, FIG. 16(a) shows a circuit diagram for 4-layer flexible circuit board, and FIG. 16(b) shows a final assembled circuit before folding. As shown in FIG. 16, the devices consist of four separate islands connected via serpentine fPCB traces to maximize mechanical flexibility while providing structural support for rigid components.

Encapsulation

The fPCBs were folded along the serpentine interconnects, depending on the intended final form factor (long for finger wrapping or short for placement on other surfaces), followed by attachment of 50mAh Li-Po batteries. 3D computer aided designed aluminum molds for the top (out-facing) and bottom (sensor-side) encapsulation were created using AutoCAD (Autodesk) and milled using CNC milling (Modela MDX-540, Roland). The molds were used to cast medical grade silicone elastomer (Silbione 4420, Elkem) shells, colored with cyan or black, visible-NIR-spectrum opaque, silicone paint (Silc Pig) with holes for the 4 LED pairs and photodiode on the bottom, and white on top. On glass slides, the bottom LED-PD holes were filled with transparent silicone (Ecoflex 00-31 Near Clear, Smooth-On) to bind the sensor head to the bottom encapsulation layer. The opposing outer shell was filled with remaining Ecoflex and the two sides of the silicone shell, with the device in between, were pressed together using external clamps and allowed to cure, thereby creating a sealed enclosure.

FIG. 17 details the encapsulation process. Specifically, FIG. 17(a) shows the encapsulation mold for the top layer, and FIG. 17(b) shows the encapsulation mold for the bottom layer. FIG. 17(c) shows transparent windows are created in the bottom layer by removing any residual silicone and filling with Ecoflex 31 before placing the device and sensor head in place to cure. FIG. 17(d) shows two exemplary device forms with different sizes.

FIG. 18 shows the effect of encapsulation on white LED emission spectrum. Specifically, FIG. 18(a) shows the emission spectrum of the broadband white LED on an unencapsulated device at different LED drive currents, and FIG. 18(b) shows the emission spectrum of the broadband white LED on a fully encapsulated device at different LED drive currents.

Adhesives

Depending on the experiment, the device was adhered to the skin using a laser cut, medical-grade, dual-sided silicone-acrylate adhesive (2477p, 3M). For long term wear or for mounting during physical exercise and sauna, the devices were adhered with medical grade transparent film adhesive (Tegaderm, 3M) or secured around a finger with medical grade self-adhering wraps (Coban, 3M).

Data Recording and Transfer

The devices are capable of both local storage of measurement data as well as real-time streaming of data to a tablet or other mobile device through Bluetooth Low Energy protocol. This external device also provides coordination of timestamping events when nearby. The devices can form a network of time-synchronized nodes using methods described previously.

FIGS. 19A and 19B show Intermittent Sampling Mode and Location Comparison, where FIG. 19A shows the location is on the thumb, and FIG. 19B shows the location to be on the wrist. In each of FIGS. 19A and 19B, panel (a) shows the whole sampling time period, and panels (b) and (c) shows detailed data in an enlarged period within the whole sampling time period. As shown in FIGS. 19A and 19B, pre-programmed sleep-wake intervals can be implemented to save battery life where continuous recording is not required. Specifically, to save battery life where continuous measurements are not required, the device can enter a low power mode and wake up for measurements at a predefined time interval, enabling more than 24h of data on a single charge.

Short-term and Medium-term BP Experiments

Pilot studies rely on healthy subjects (n=10, 8 male, 2 female, median age 28 years, std. dev. 2.5 years) with repeated exposure (total number of sets) to a sauna (10), cold pressor (21), physical exercise (15), breath hold (15), and Valsalva maneuver (20). Additional analysis includes data from 20 hypertensive patients (10 male, 10 female, median age 69 years, std. dev. 14 years) collected during regular clinical visits with repeated Valsalva maneuvers. Data from six different wavelength channels from MWPPG signals captured using the first pair of LEDs were captured during simultaneous reference measurements of BP using the continuous volume-clamp method (NOVA, Finapres Medical Systems). Subjects wore a MWPPG sensor on their non-dominant hand, as well as an ECG/SCG sensor on their chest for HR and PAT. Subjects were asked to rest for 5 minutes to establish baseline measurements, then to perform a Valsalva maneuver for no longer than 15 seconds, followed by a period of rest and return to within 5mmHg of baseline systolic BP. Then, each subject placed their dominant (non-sensor) hand in a bucket of cold water no colder than 4°C for as long as they were comfortable but no longer than 1 minute. This procedure was followed by a rest and return to within 5mmHg of baseline systolic BP, and then a period of breath holding for as long as the subject was comfortable. After another return to 5mmHg of baseline systolic BP, the pressors were repeated two more times for consistency. Hypertensive subjects were only asked to perform the Valsalva maneuver. Any test which did not elicit a systolic BP rise > 15mmHg was not included in subsequent analysis. Subject were not asked to repeat the experiment for any missed cycle. Healthy subjects willing to participate in additional, medium-term, experiments were asked to return for exercise or sauna testing. The devices were affixed in the same locations as the short-term BP Experiments. For the sauna test, following a 10-minute period of rest to establish baseline measurements, subjects sat in a portable sauna for 30 minutes (or until tolerated) at 50°C, followed by 15 minutes of recovery. For the exercise test, following a 10-minute period for baseline measurements, the subjects physically exercised at a moderate rate until light sweating was elicited, held that intensity for 10 minutes, and then stopped exercise and recovered for 15 minutes.

Post-surgical Monitoring

The study devices were affixed to 15 (8 male, 7 female, median age 61 years, std. dev. 11.4 years) previously informed and consented patients upon completion of cardiothoracic

surgery in the Northwestern Memorial Hospital cardiothoracic intensive care unit. Sensors are placed as soon as possible following rooming in the cardiothoracic intensive care unit without interrupting standard of care procedures. Information on demographics (height weight, age, sex), relevant cardiac medical history, hemodynamic modulating medications and relevant vital signs and laboratory measurements were collected via pre-defined queries through the Northwestern Electronic Data Warehouse (EDW). Sensor data and EDW data were de-identified, linked only through a unique subject ID. Only subjects with significant post-surgical hypotension treated by vasoconstrictive medications (e.g. epinephrine, norepinephrine, phenylephrine) were considered for classification (n=4, 1 male, 3 female), however all data with additional medications and interventions are available for further analysis.

Data Exclusion

Datasets were planned to be excluded if measurements during the baseline resting period varied by more than +/-10mmHg, as this could indicate problems with reference measurements or underlying hemodynamic instability which could confound response to stimuli. Patients who were not treated with vasoconstrictive medication in the immediate postoperative period were excluded from analysis. Extreme values due to artifact were excluded on a physiological basis (e.g. sudden HR spikes or drops of > 50bpm that could indicate missed peaks), or measurement values > 6 standard deviations from others in that dataset.

Data Analysis

Analysis of sensor data was performed in Python 3.10 using openly available packages including NumPy (1.23.5), SciPy (1.9.3), Pandas (1.5.1), Scikit-learn (1.1.2) and SHAP (0.41.0), with visualization in matplotlib (3.6.0) and seaborn (0.11.2). Hemodynamic state labeling was performed on reference BP measurements (Finapres for short-medium term experiments, Cuff BP or arterial line BP for patients) in combination with experiment timelines or medical record medication administration and events where available. Alignment between sensor data and labelled reference sources was accomplished by matching the HR calculation from sensor system and Finapres or medical record HR values, as well as induced signal perturbations in both data streams by tapping. In the final HR, PAT, and MW Delay data used for the FIG. 11 scatter plots and classification, a 5 second median window was applied to all measurements around every detected heartbeat after grouping by label. To control for inter-subject variability due to

differences in limb length, arterial tree morphology, and baseline vascular tone, each data point is baseline subtracted. Baseline corresponds to the median value captured as the subject remains seated at rest for 5 minutes and diastolic BP remains within an interval of +/-10mmHg. The median value of each calculated parameter during this time is subtracted from each remaining datapoint for that set.

HR-PAT Calculation

The green wavelength at 515nm channel of the MWPPG signal was used for further processing given its relative resistance to blood volume changes in deeper layers driven by motion artifacts. The signal was bandpass filtered with a zero-phase, 4th order Butterworth filter with cutoffs at 0.5Hz - 5Hz. The first derivative of the bandpass filtered signal was calculated and passed through an automatic multiscale peak-detector algorithm. In some cases, the R-peak of the ECG signal was used to determine a search domain for complimentary first-derivative pulse peaks in the PPG waveform. Complementary ECG R-peak and PPG first derivative peak locations were subtracted to calculate PAT.

SpO_2

Blood oxygenation is defined as the ratio of oxygenated hemoglobin to total hemoglobin in the following formula:

$$SpO_2 = \frac{c_{HbO_2}}{c_{HbO_2} + c_{Hb}} \times 100\%$$

Oxygenated hemoglobin has a local peak absorbance in the infrared range, roughly at 940 nm. A local minimum in absorbance occurs at roughly 680 nm, a wavelength where deoxygenated hemoglobin absorbs more strongly. The device used in this study wavelengths of 900nm and 680nm were used for analysis of SpO_2. Relative changes in reflected light intensity with frequencies between 0.5-10Hz correspond to pulsatile signals that result from changes in blood volume changes. The time independent part of the signal corresponds to light reflected from the bulk tissue. The quantity R, known as the ratio of ratios, is inversely related to SpO_2,

$$R = \frac{Pulse_{680nm}/Baseline_{680nm}}{Pulse_{900nm}/Baseline_{900nm}}$$

Empirical fitting procedures establish relationships between R and SpO_2. In the case of

this study, the fit coefficients were determined using reference SpO_2 values generated from data originating from the post-surgical patient with the greatest range of SpO_2 in their medical record while the devices were mounted.

MW Delay

Calculations of MW Delay were performed on windows of 5 seconds of pulsatile signals with the same 0.5-5Hz bandwidth from all 6 available wavelengths. 6 wavelengths are used as they are the maximum allowed in a single integration cycle on the multispectral photodiode, maximizing sample rate. The bandpassed waveforms were normalized, and principal component analysis (PCA) with two output dimensions was performed on the matrix with all wavelengths, and separately on a subset of this matrix consisting of only near-surface interacting wavelengths (blue-green). The PCA weights are calculated uniquely on each window to prevent influence of motion artifacts and pulse morphology changes from other sections of the dataset from affecting local processes. Following approaches similar to those reported previously, and visually described in FIG. 6B, the first component of the PCA with all the wavelengths was theorized to consist of a superposition of arterial- and capillary- type pulsations, while the first component of the PCA with only near-surface wavelengths was considered to contain only capillary components. A signal consisting of primarily arterial pulsation followed from subtraction of the latter from the former. The capillary and arterial pulse waveforms were then compared using a fractional delay estimation algorithm based on the fast Fourier transform and sub-sample phase fitting to estimate the delay between the two signals throughout the waveform at a high precision. The second principal component from the near-surface PCA was extracted to develop signal quality indices based on statistical analysis of those, generally non-pulsatile, components.

FIG. 20 shows a Table of MW Delay Comparisons by Stimulus. Statistical test between each hemodynamic stimulus and baseline values across all datasets. The two-tailed Welch's t-test for unequal variances is used. Negative signs indicate an increase relative to baseline values. Data points correspond to median values of each measurement around each detected heartbeat. The number of surgical pressor points is low due to the intermittent BP measurements acquired from the medical record data warehouse. P values are indicated in parentheses next to the test statistic with ****=p<.0001.

Data availability

Data used in classification model training is presented in its entirety within FIG. 11 and is available from the corresponding authors upon reasonable request and Institutional Review Board approval.

Code availability

Code used for analysis and to produce figures is also available upon reasonable request to the corresponding authors, however implementations of methods described in the text exist in public repositories described in the data analysis section and in referenced work.

The foregoing description of the exemplary embodiments of the invention has been presented only for the purposes of illustration and description and is not intended to be exhaustive or to limit the invention to the precise forms disclosed. Many modifications and variations are possible in light of the above teaching.

The embodiments were chosen and described in order to explain the principles of the invention and their practical application so as to enable others skilled in the art to utilize the invention and various embodiments and with various modifications as are suited to the particular use contemplated. Alternative embodiments will become apparent to those skilled in the art to which the invention pertains without departing from its spirit and scope. Accordingly, the scope of the invention is defined by the appended claims rather than the foregoing description and the exemplary embodiments described therein.

Some references, which may include patents, patent applications, and various publications, are cited and discussed in the description of this invention. The citation and/or discussion of such references is provided merely to clarify the description of the invention and is not an admission that any such reference is "prior art" to the invention described herein. All references cited and discussed in this specification are incorporated herein by reference in their entireties and to the same extent as if each reference was individually incorporated by reference.

REFERENCE LIST:

1. Heidenreich, P. A. *et al.* 2022 AHA/ACC/HFSA Guideline for the Management of Heart Failure: A Report of the American College of Cardiology/American Heart Association Joint Committee on Clinical Practice Guidelines. *J Am Coll Cardiol* **79**, e263–e421 (2022).

2. January, C. T. *et al.* 2019 AHA/ACC/HRS Focused Update of the 2014 AHA/ACC/HRS Guideline for the Management of Patients With Atrial Fibrillation: A Report of the American College of Cardiology/American Heart Association Task Force on Clinical Practice Guidelines and the Heart Rhythm Society in Collaboration With the Society of Thoracic Surgeons. *Circulation* **140**, e125–e151 (2019).
3. Truby, L. K. & Rogers, J. G. Advanced Heart Failure: Epidemiology, Diagnosis, and Therapeutic Approaches. *Heart Fail* **8**, 523–536 (2020).
4. Pinsky, M. R. & Payen, D. Functional hemodynamic monitoring. *Crit Care* **9**, 566–572 (2005).
5. Teboul, J. L. *et al.* Less invasive hemodynamic monitoring in critically ill patients. *Intensive Care Med* **42**, 1350–1359 (2016).
6. Cotter, G. *et al.* The role of cardiac power and systemic vascular resistance in the pathophysiology and diagnosis of patients with acute congestive heart failure. *Eur J Heart Fail* **5**, 443–451 (2003).
7. Delong, C. & Sharma, S. Physiology, Peripheral Vascular Resistance. in *StatPearls* (StatPearls Publishing, 2022).
8. Keville, M. P. *et al.* Arterial or cuff pressure: Clinical predictors among patients in shock in a critical care resuscitation unit. *Am J Emerg Med* **46**, 109–115 (2021).
9. Tran, Q. K. *et al.* Discrepancy Between Invasive and Noninvasive Blood Pressure Measurements in Patients with Sepsis by Vasopressor Status. *Western Journal of Emergency Medicine* **23**, 358–367 (2022).
10. Chen, Y. *et al.* Right Heart Catheterization-Related Complications: A Review of the Literature and Best Practices. *Cardiol Rev* **28**, 36–41 (2020).
11. Desai, A. S. *et al.* Ambulatory Hemodynamic Monitoring Reduces Heart Failure Hospitalizations in "Real-World" Clinical Practice. *J Am Coll Cardiol* **69**, 2357–2365 (2017).
12. Abraham, J. *et al.* Association of Ambulatory Hemodynamic Monitoring of Heart Failure With Clinical Outcomes in a Concurrent Matched Cohort Analysis. *JAMA Cardiol* **4**, 556–563 (2019).
13. Malasinghe, L. P., Ramzan, N. & Dahal, K. Remote patient monitoring: a comprehensive study. *J Ambient Intell Humaniz Comput* **10**, 57–76 (2019).
14. Noah, B. *et al.* Impact of remote patient monitoring on clinical outcomes: an updated meta-analysis of randomized controlled trials. *npj Digital Medicine 2018 1:1* **1**, 1–12 (2018).
15. Yetisen, A. K. *et al.* Wearables in Medicine. *Advanced Materials* **30**, 1706910 (2018).
16. Olmedo-Aguirre, J. O. *et al.* Remote Healthcare for Elderly People Using Wearables: A Review. *Biosensors (Basel)* **12**, 73 (2022).
17. Bayoumy, K. *et al.* Smart wearable devices in cardiovascular care: where we are and how to move forward. *Nature Reviews Cardiology 2021 18:8* **18**, 581–599 (2021).
18. Pevnick, J. M., Birkeland, K., Zimmer, R., Elad, Y. & Kedan, I. Wearable technology for cardiology: An update and framework for the future. *Trends Cardiovasc Med* **28**, 144–150 (2018).
19. Prieto-Avalos, G. *et al.* Wearable Devices for Physical Monitoring of Heart: A Review. *Biosensors (Basel)* **12**, 292 (2022).
20. Huhn, S. *et al.* The Impact of Wearable Technologies in Health Research: Scoping Review. *JMIR Mhealth Uhealth* **10**, (2022).

21. Boubouchairopoulou, N., Ntineri, A., Kollias, A., Destounis, A. & Stergiou, G. S. Blood pressure variability assessed by office, home, and ambulatory measurements: comparison, agreement, and determinants. *Hypertension Research* **44**, 1617–1624 (2021).
22. Stergiou, G. S. *et al.* Hypertension Evaluation of the Accuracy of Cuffless Blood Pressure Measurement Devices: Challenges and Proposals. *Hypertension* **78**, 1161–1167 (2021).
23. Stergiou, G. S. *et al.* Cuffless blood pressure measuring devices: review and statement by the European Society of Hypertension Working Group on Blood Pressure Monitoring and Cardiovascular Variability. *J Hypertens* **40**, 1449–1460 (2022).
24. Schutte, A. E., Kollias, A. & Stergiou, G. S. Blood pressure and its variability: classic and novel measurement techniques. *Nature Reviews Cardiology 2022 19:10* **19**, 643–654 (2022).
25. Stergiou, G. S. *et al.* Methodology and technology for peripheral and central blood pressure and blood pressure variability measurement: Current status and future directions - Position statement of the European Society of Hypertension Working Group on blood pressure monitoring and cardiovascular variability. *J Hypertens* **34**, 1665–1677 (2016).
26. Ma, Y. *et al.* Relation between blood pressure and pulse wave velocity for human arteries. *Proc Natl Acad Sci U S A* **115**, 11144–11149 (2018).
27. Mukkamala, R. *et al.* Towards Ubiquitous Blood Pressure Monitoring via Pulse Transit Time: Theory and Practice HHS Public Access. *IEEE Trans Biomed Eng* **62**, 1879–1901 (2015).
28. Wibmer, T. *et al.* Blood pressure monitoring during exercise: Comparison of pulse transit time and volume clamp methods. *Blood Press* **24**, 353–360 (2015).
29. Finnegan, E. *et al.* Pulse arrival time as a surrogate of blood pressure. *Sci Rep* **11**, 1–21 (2021).
30. Proença, J., Muehlsteff, J., Aubert, X. & Carvalho, P. Is pulse transit time a good indicator of blood pressure changes during short physical exercise in a young population? *Annu Int Conf IEEE Eng Med Biol Soc* **2010**, 598–601 (2010).
31. Kounalakis, S. N. & Geladas, N. D. The role of pulse transit time as an index of arterial stiffness during exercise. *Cardiovascular Engineering* **9**, 92–97 (2009).
32. Polónia, J., Barbosa, L., Silva, J. A. & Maldonado, J. Different influences on central and peripheral pulse pressure, aortic wave reflections and pulse wave velocity of three different types of antihypertensive drugs. *Rev Port Cardiol* **22**, 1485–1492 (2003).
33. Kelly, R. P., Millasseau, S. C., Ritter, J. M. & Chowienczyk, P. J. Vasoactive Drugs Influence Aortic Augmentation Index Independently of Pulse-Wave Velocity in Healthy Men. *Hypertension* **37**, 1429–1433 (2001).
34. Borner, A., Murray, K., Trotter, C. & Pearson, J. Baseline aortic pulse wave velocity is associated with central and peripheral pressor responses during the cold pressor test in healthy subjects. *Physiol Rep* **5**, e13357 (2017).
35. Elias, S. O. & Ajayi, R. E. Effect of sympathetic autonomic stress from the cold pressor test on left ventricular function in young healthy adults. *Physiol Rep* **7**, (2019).
36. Parati, G., Stergiou, G. S., Dolan, E. & Bilo, G. Blood pressure variability: clinical relevance and application. in *Journal of Clinical Hypertension* vol. 20 1133–1137 (Blackwell Publishing Inc., 2018).
37. Lantelme, P., Mestre, C., Lievre, M., Gressard, A. & Milon, H. Heart Rate: An Important Confounder of Pulse Wave Velocity Assessment. *Hypertension* **39**, 1083–1087 (2002).

38. Papaioannou, T. G. *et al.* The influence of resting heart rate on pulse wave velocity measurement is mediated by blood pressure and depends on aortic stiffness levels: insights from the Corinthia study. *Physiol Meas* **40**, 055005 (2019).
39. Sherwood, A. *et al.* Methodological Guidelines for Impedance Cardiography. *Psychophysiology* **27**, 1–23 (1990).
40. Levy, J. H., Kouz, K., Scheeren, T. W. L., De Backer, D. & Saugel, B. CliniCal FoCus Review Pulse Wave Analysis to Estimate Cardiac Output. *Anesthesiology* **134**, 119–145 (2021).
41. Hametner, B. & Wassertheurer, S. Pulse Waveform Analysis: Is It Ready for Prime Time? *Current Hypertension Reports 2017 19:9* **19**, 1–7 (2017).
42. Liu, J. *et al.* Multi-wavelength photoplethysmography method for skin arterial pulse extraction. *Biomed Opt Express* 7, 4313 (2016).
43. Liu, J. *et al.* Multi-Wavelength Photoplethysmography Enabling Continuous Blood Pressure Measurement With Compact Wearable Electronics. *IEEE Trans Biomed Eng* **66**, 1514–1525 (2019).
44. Liu, J. *et al.* PCA-Based Multi-Wavelength Photoplethysmography Algorithm for Cuffless Blood Pressure Measurement on Elderly Subjects. *IEEE J Biomed Health Inform* **25**, 663–673 (2021).
45. Spigulis, J., Gailite, L., Lihachev, A. & Erts, R. Simultaneous recording of skin blood pulsations at different vascular depths by multiwavelength photoplethysmography. *Appl Opt* **56**, (2007).
46. Aidar, F. J. *et al.* Can Post-Exercise Hemodynamic Response Be Influenced by Different Recovery Methods in Paraplegic Sportsmen? *International Journal of Environmental Research and Public Health 2022, Vol. 19, Page 1772* **19**, 1772 (2022).
47. Francisco, M. A. *et al.* Hemodynamics of postexercise versus post-hot water immersion recovery. *J Appl Physiol* **130**, 1362–1372 (2021).
48. Churchill, T. W. The Impact of Exercise and Athletic Training on Vascular Structure and Function. *Curr Treat Options Cardiovasc Med* **22**, 1–11 (2020).
49. Bauer, P. *et al.* Blood Pressure Response and Vascular Function of Professional Athletes and Controls. *Sports Med Int Open* **5**, E45–E52 (2021).
50. McDuff, D. *et al.* Non-contact imaging of peripheral hemodynamics during cognitive and psychological stressors. *Scientific Reports 2020 10:1* **10**, 1–13 (2020).
51. Chung, H. U. *et al.* Skin-interfaced biosensors for advanced wireless physiological monitoring in neonatal and pediatric intensive-care units. *Nat Med* **26**, 418–429 (2020).
52. Lee, K. H. *et al.* Mechano-acoustic sensing of physiological processes and body motions via a soft wireless device placed at the suprasternal notch. *Nat Biomed Eng* **4**, 148–158 (2020).
53. Finlayson, L. *et al.* Depth Penetration of Light into Skin as a Function of Wavelength from 200 to 1000 nm. *Photochem Photobiol* **98**, 974–981 (2022).
54. Rwei, A. Y. *et al.* A wireless, skin-interfaced biosensor for cerebral hemodynamic monitoring in pediatric care. *Proc Natl Acad Sci U S A* **117**, 31674–31684 (2020).
55. Nishimura, R. A. & Tajik, A. J. The Valsalva Maneuver and Response Revisited. *Mayo Clin Proc* **61**, 211–217 (1986).
56. Bennett, T., Hosking, D. J. & Hampton, J. R. Vasomotor responses to the Valsalva manoeuvre in normal subjects and in patients with diabetes mellitus. *Br Heart J* **42**, 422–428 (1979).

57. Awad, A. A. *et al.* Different responses of ear and finger pulse oximeter wave form to cold pressor test. *Anesth Analg* **92**, 1483–1486 (2001).
58. Lovallo, W. The Cold Pressor Test and Autonomic Function: A Review and Integration. *Psychophysiology* **12**, 268–282 (1975).
59. Heistad, D. D., Abboud, F. M. & Eckstein, J. W. Vasoconstrictor response to simulated diving in man. *J Appl Physiol* **25**, 542–549 (1968).
60. Kellogg, D. L., Crandall, C. G., Liu, Y., Charkoudian, N. & Johnson, J. M. Nitric oxide and cutaneous active vasodilation during heat stress in humans. *J Appl Physiol* **85**, 824–829 (1998).
61. Kim, M. Y. *et al.* Acute Reduction of Pulse Wave Velocity after Sauna in Adults in a Community. *Journal of the Korean Academy of Family Medicine* **27**, 384–390 (2006).
62. Lee, E. *et al.* Sauna exposure leads to improved arterial compliance: Findings from a non-randomised experimental study. *Eur J Prev Cardiol* **25**, 130–138 (2018).
63. Laukkanen, T. *et al.* Acute effects of sauna bathing on cardiovascular function. *Journal of Human Hypertension 2017 32:2* **32**, 129–138 (2017).
64. Teixeira, L., Ritti-Dias, R. M., Tinucci, T., Mion, D. & De Moraes Forjaz, C. L. Post-concurrent exercise hemodynamics and cardiac autonomic modulation. *Eur J Appl Physiol* **111**, 2069–2078 (2011).
65. Vatner, S. F. & Pagani, M. Cardiovascular adjustments to exercise: Hemodynamics and mechanisms. *Prog Cardiovasc Dis* **19**, 91–108 (1976).
66. Desebbe, O. *et al.* Control of Postoperative Hypotension Using a Closed-Loop System for Norepinephrine Infusion in Patients After Cardiac Surgery: A Randomized Trial. *Anesth Analg* **134**, 964–973 (2022).
67. Richard E. Klabunde. *Cardiovascular Physiology Concepts*. (Wolters Kluwer | Lippincott Williams & Wilkins, 2021).
68. Hofmann, H., Kafadar, K. & Wickham, H. Letter-value plots: Boxplots for large data. (2011).
69. Brunner, E. & Munzel, U. Rank-Score Tests in Factorial Designs with Repeated Measures. *J Multivar Anal* **70**, 286–317 (1999).
70. Mitchell, L. A., MacDonald, R. A. R. & Brodie, E. E. Temperature and the cold pressor test. *J Pain* **5**, 233–237 (2004).
71. Reddy, S. Explainability and artificial intelligence in medicine. *Lancet Digit Health* **4**, e214–e215 (2022).
72. Lundberg, S. M., Allen, P. G. & Lee, S.-I. A Unified Approach to Interpreting Model Predictions. *Adv Neural Inf Process Syst* **30**, (2017).
73. Newlin, D. B. & Levenson, R. W. Pre-ejection Period: Measuring Beta-adrenergic Influences Upon the Heart. *Psychophysiology* **16**, 546–552 (1979).
74. Garrard, C. L., Weissler, A. M. & Dodge, H. T. The Relationship of Alterations in Systolic Time Intervals to Ejection Fraction in Patients with Cardiac Disease. *Circulation* **42**, 455–462 (1970).
75. Harris, C. R. *et al.* Array programming with NumPy. *Nature* **585**, 357–362 (2020).
76. Virtanen, P. *et al.* SciPy 1.0: fundamental algorithms for scientific computing in Python. *Nat Methods* **17**, 261–272 (2020).
77. McKinney, W. Data Structures for Statistical Computing in Python. *Proceedings of the 9th Python in Science Conference* 56–61 (2010) doi:10.25080/MAJORA-92BF1922-00A.

78. Pedregosa, F. *et al.* Scikit-learn: Machine Learning in Python. *Journal of Machine Learning Research* **12**, 2825–2830 (2011).
79. Hunter, J. D. Matplotlib: A 2D Graphics Environment. *Comput Sci Eng* **9**, 90–95 (2007).
80. Waskom, M. seaborn: statistical data visualization. *J Open Source Softw* **6**, 3021 (2021).
81. Maeda, Y., Sekine, M. & Tamura, T. The advantages of wearable green reflected photoplethysmography. *J Med Syst* **35**, 829–834 (2011).
82. Lee, J. *et al.* Comparison between red, green and blue light reflection photoplethysmography for heart rate monitoring during motion. *Annu Int Conf IEEE Eng Med Biol Soc* **2013**, 1724–1727 (2013).
83. Scholkmann, F., Boss, J. & Wolf, M. An Efficient Algorithm for Automatic Peak Detection in Noisy Periodic and Quasi-Periodic Signals. *Algorithms* **5**, 588–603 (2012).

CLAIMS

What is claimed is:

1. A multi-nodal physiological monitoring system for measuring physiological parameters of a living subject, comprising:

a central sensor configured to be disposed at a central position of the living subject to measure electrocardiogram (ECG) and mechano-acoustic (MA) signals; and

at least one multi-spatial, multi-wavelength photoplethysmography (MWPPG) sensor configured to be disposed at the central position or a peripheral position of the living subject to acquire cardiac and vascular signals;

wherein the central sensor and the at least one MWPPG sensor are configured to communicate and time-synchronize wirelessly, and the ECG and MA signals from the central sensor and the cardiac and vascular signals from the at least one MWPPG sensor are processed to simultaneously extract hemodynamic metrics and local vascular metrics.

2. The multi-nodal physiological monitoring system of claim 1, wherein the central position is a chest area of the living subject, and the peripheral position is a finger area, a wrist area, or a limb area of the living subject.

3. The multi-nodal physiological monitoring system of claim 1, being configured to measure and classify physiologic changes associated with specific hemodynamic states based on a pulse arrival time (PAT), a pulse propagation time and heart rate (HR), wherein the arterial PWV is obtained through the PAT, and the arteriolar PWV is obtained through the pulse propagation time.

4. The multi-nodal physiological monitoring system of claim 1, wherein the central sensor comprises:

an analog differential amplifier-filter configured to measure ECG signals;

a temperature sensor configured to measure temperature; and

a triaxial accelerometer configured to simultaneously measure seismocardiogram (SCG) signals, core body motion, vocal processes, and physical activity.

5. The multi-nodal physiological monitoring system of claim 1, wherein the at least one MWPPG sensor comprises:

a temperature sensor configured to measure temperature;

a multispectral photodiode; and

a plurality of linear array of light emitting diodes (LEDs) configured to emit visible light and near-infrared (NIR) light.

6. The multi-nodal physiological monitoring system of claim 5, wherein the at least one MWPPG sensor further comprises:

a triaxial accelerometer configured to simultaneously measure seismocardiogram (SCG) signals, core body motion, vocal processes, and physical activity.

7. The multi-nodal physiological monitoring system of claim 1, wherein each of the central sensor and the at least one MWPPG sensor comprises:

a flexible printed circuit board (fPCB);

a middle circuit board layer disposed on the fPCB, including a plurality of electronic components, and a plurality of flexible and stretchable interconnects electrically connected to different electronic components; and

a top elastomeric encapsulation layer and a bottom elastomeric encapsulation layer sandwiching the middle circuit board layer, wherein the bottom elastomeric encapsulation layer forms a tissue-facing surface attached to the living subject, and the top elastomeric encapsulation layer forms an environment-facing surface.

8. The multi-nodal physiological monitoring system of claim 7, wherein the middle circuit board layer is formed by a foldable electronic board, and the plurality of electronic components and the plurality of flexible and stretchable interconnects are disposed on the foldable electronic board.

9. The multi-nodal physiological monitoring system of claim 1, wherein each of the central sensor and the at least one MWPPG sensor is attached to a skin of the living subject

through an adhesive layer.

10. The multi-nodal physiological monitoring system of claim 9, wherein the adhesive layer is formed by a dual-sided silicone-acrylate adhesive, a transparent film adhesive, or a self-adhering wrap.

11. The multi-nodal physiological monitoring system of claim 1, wherein each of the central sensor and the at least one MWPPG sensor further comprises an embedded power supply or a remote charging power supply.

12. The multi-nodal physiological monitoring system of any one of claims 1-11, wherein the living subject is a human subject or a non-human subject.

13. A method of measuring physiological parameters of a living subject with a multi-nodal physiological monitoring system, the method comprising:

disposing a central sensor at a central position of the living subject to measure multi-modal electrocardiogram (ECG) and mechano-acoustic (MA) signals;

disposing at least one multi-spatial, multi-wavelength photoplethysmography (MWPPG) sensor at the central position or a peripheral position of the living subject to acquire cardiac and vascular signals; and

communicating and time-synchronizing the central sensor and the at least one MWPPG sensor wirelessly to process the ECG and MA signals from the central sensor and the cardiac and vascular signals from the at least one MWPPG sensor to simultaneously extract hemodynamic metrics and local vascular metrics from the ECG and MA signals and the cardiac and vascular signals.

14. The method of claim 13, wherein the central position is a chest area of the living subject, and the peripheral position is a finger area, a wrist area or a limb area of the living subject.

15. The method of claim 13, wherein the multi-nodal physiological monitoring system is

configured to measure and classify physiologic changes associated with specific hemodynamic states based on a pulse arrival time (PAT), a pulse propagation time and heart rate (HR), wherein the arterial PWV is obtained through the PAT, and the arteriolar PWV is obtained through the pulse propagation time.

16. The method of claim 13, wherein the central sensor comprises:

an analog differential amplifier-filter configured to measure ECG signals;

a temperature sensor configured to measure temperature; and

a triaxial accelerometer configured to simultaneously measure seismocardiogram (SCG) signals, core body motion, vocal processes, and physical activity.

17. The method of claim 14, wherein the at least one MWPPG sensor comprises:

a temperature sensor configured to measure temperature;

a multispectral photodiode; and

a plurality of linear array of light emitting diodes (LEDs) configured to emit visible light and near-infrared (NIR) light.

18. The method of claim 17, wherein the at least one MWPPG sensor further comprises:

a triaxial accelerometer configured to simultaneously measure seismocardiogram (SCG) signals, core body motion, vocal processes, and physical activity.

19. The method of claim 13, wherein each of the central sensor and the at least one MWPPG sensor comprises:

a flexible printed circuit board (fPCB);

a middle circuit board layer disposed on the fPCB, including a plurality of electronic components, and a plurality of flexible and stretchable interconnects electrically connected to different electronic components; and

a top elastomeric encapsulation layer and a bottom elastomeric encapsulation layer sandwiching the middle circuit board layer, wherein the bottom elastomeric encapsulation layer forms a tissue-facing surface attached to the living subject, and the top elastomeric encapsulation layer forms an environment-facing surface.

20. The method of claim 19, wherein the middle circuit board layer is formed by a foldable electronic board, and the plurality of electronic components and the plurality of flexible and stretchable interconnects are disposed on the foldable electronic board.

21. The method of claim 13, wherein each of the central sensor and the at least one MWPPG sensor is attached to a skin of the living subject through an adhesive layer.

22. The method of claim 21, wherein the adhesive layer is formed by a dual-sided silicone-acrylate adhesive, a transparent film adhesive, or a self-adhering wrap.

23. The method of claim 13, wherein each of the each of the central sensor and the at least one MWPPG sensor further comprises an embedded power supply or a remote charging power supply.

24. The method of any one of claims 13-23, wherein the living subject is a human subject or a non-human subject.

25. A non-transitory tangible computer-readable medium storing instructions which, when executed by one or more processors, cause the method of any one of claims 13-23 to be performed.

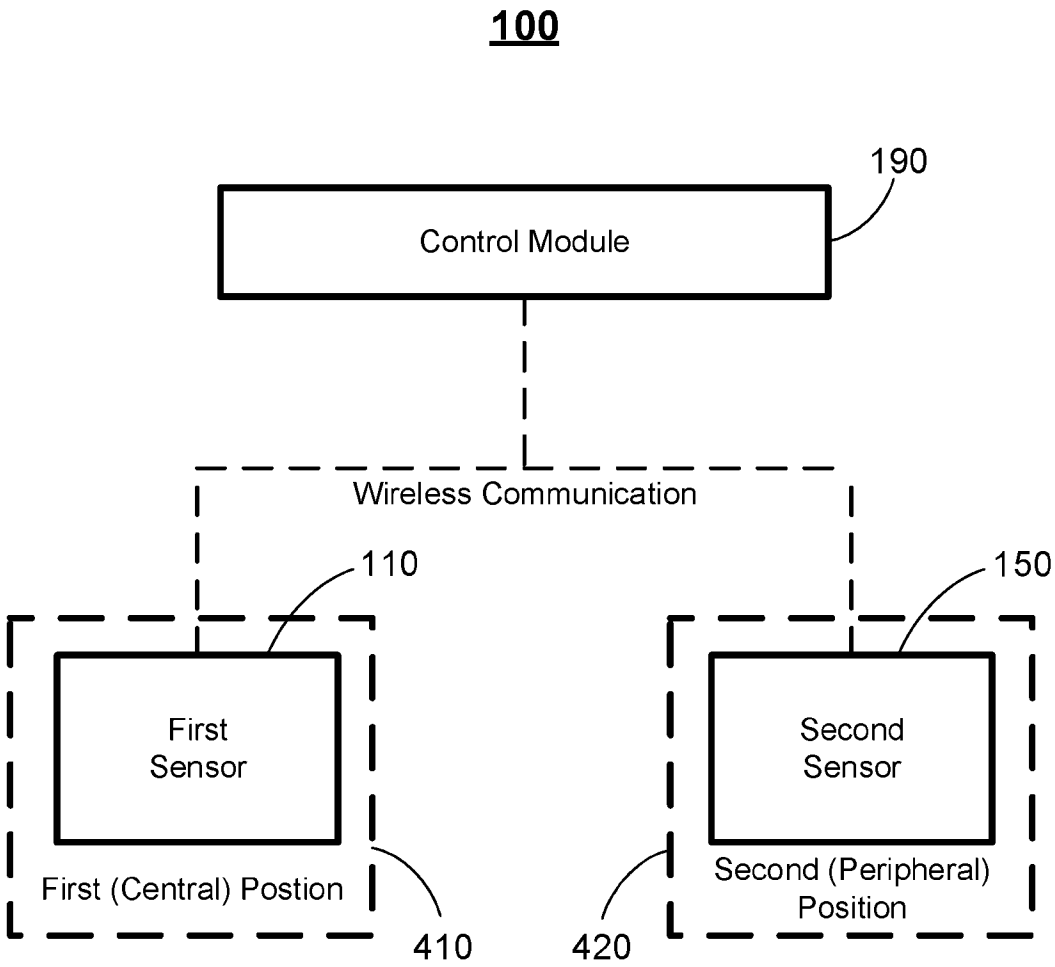

100
190
Control Module
Wireless Communication
110
150
First
Sensor
Second
Sensor
First (Central) Postion
410
420
Second (Peripheral)
Position

FIG. 1

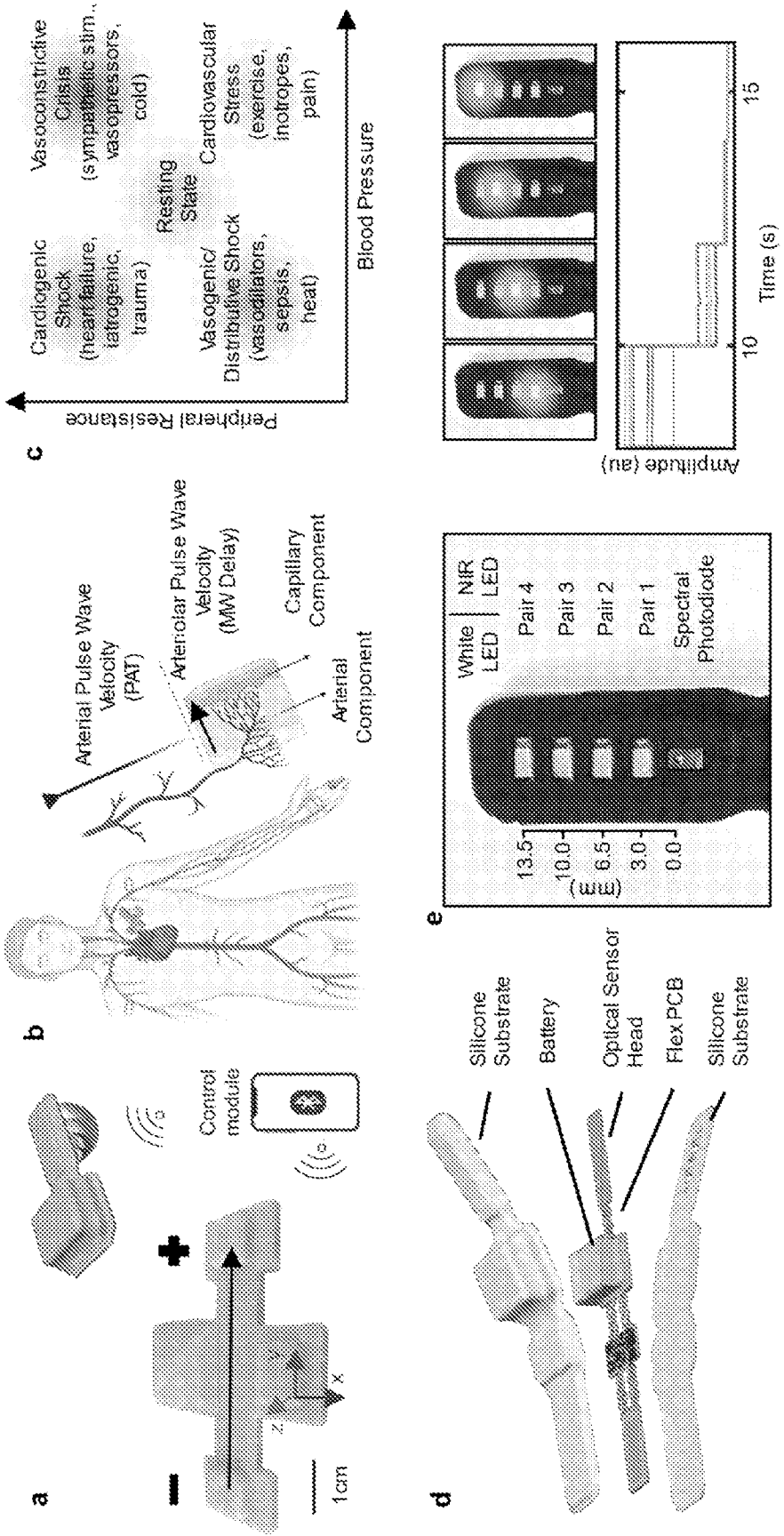

a
Control module
1cm
x
z
b
Arterial Pulse Wave Velocity (PAT)
Arteriolar Pulse Wave Velocity (MW Delay)
Capillary Component
Arterial Component
c
Peripheral Resistance
Blood Pressure
Cardiogenic Shock (heart failure, iatrogenic, trauma)
Vasogenic/ Distributive Shock (vasodilators, sepsis, heat)
Resting State
Vasoconstrictive Crisis (sympathetic stim., vasopressors, cold)
Cardiovascular Stress (exercise, inotropes, pain)
d
Silicone Substrate
Battery
Optical Sensor Head
Flex PCB
Silicone Substrate
e
White LED
NIR LED
Pair 4
Pair 3
Pair 2
Pair 1
Spectral Photodiode
13.5
10.0
6.5
3.0
0.0
(mm)
Amplitude (au)
10
15
Time (s)

FIG. 2A

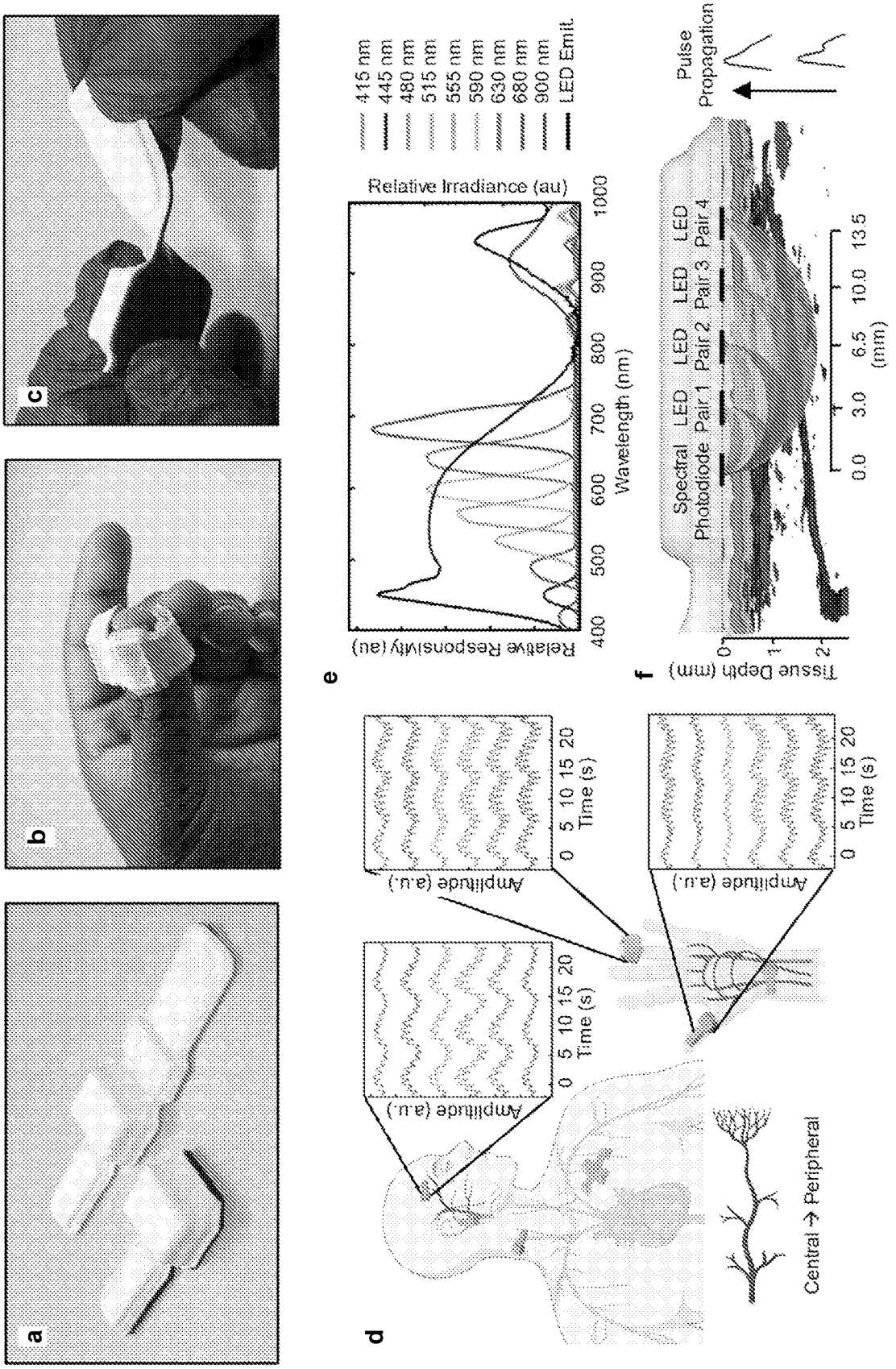

a
b
c
d
e
f
Amplitude (a.u.)
0 5 10 15 20
Time (s)
Central → Peripheral
Relative Irradiance (au)
Relative Responsivity (au)
400 500 600 700 800 900 1000
Wavelength (nm)
415 nm
445 nm
480 nm
515 nm
555 nm
590 nm
630 nm
680 nm
900 nm
LED Emit.
Spectral LED Photodiode Pair 1
LED Pair 2
LED Pair 3
LED Pair 4
Pulse Propagation
Tissue Depth (mm)
0 1 2
0.0 3.0 6.5 10.0 13.5
(mm)

FIG. 2B

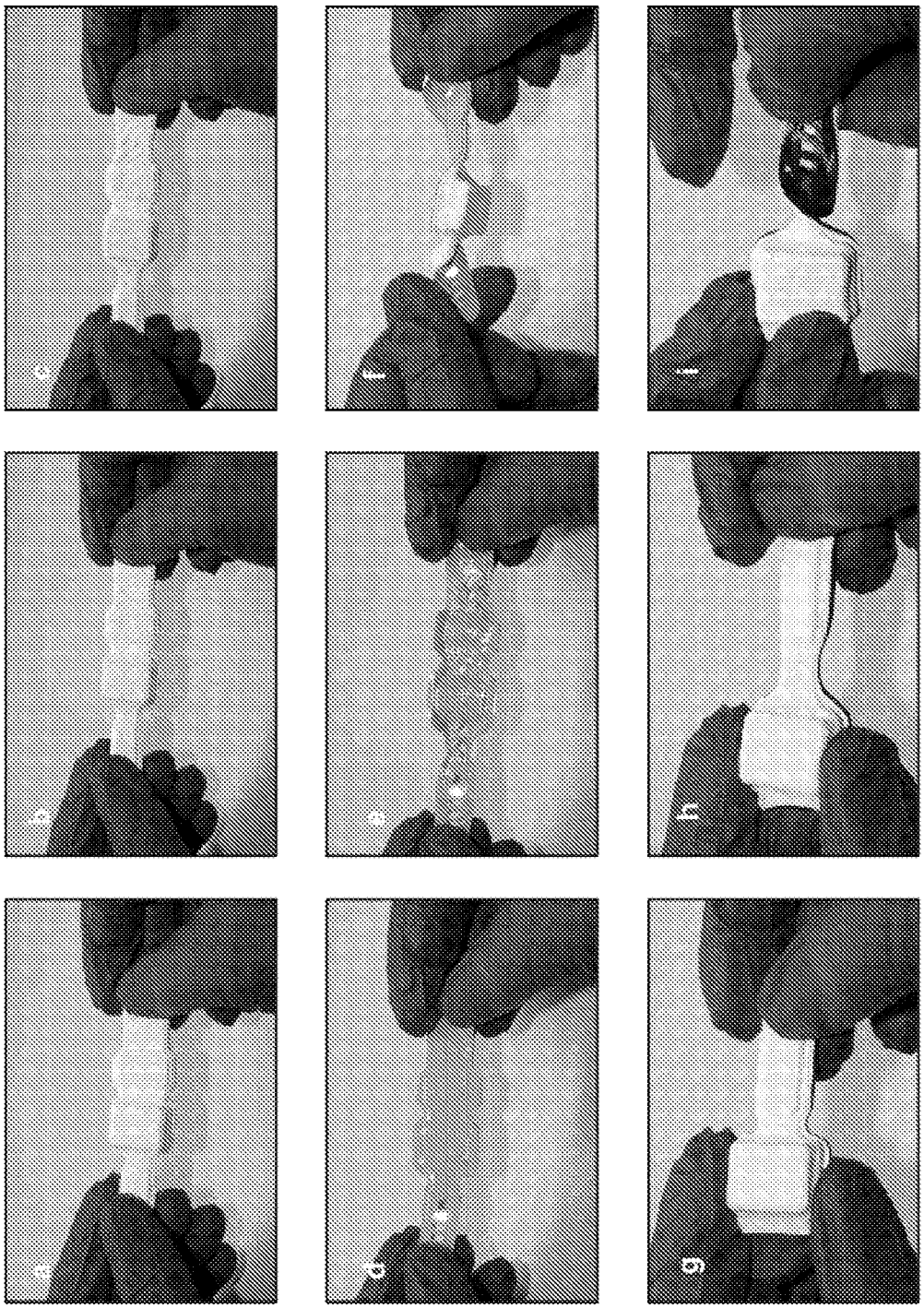


FIG. 3

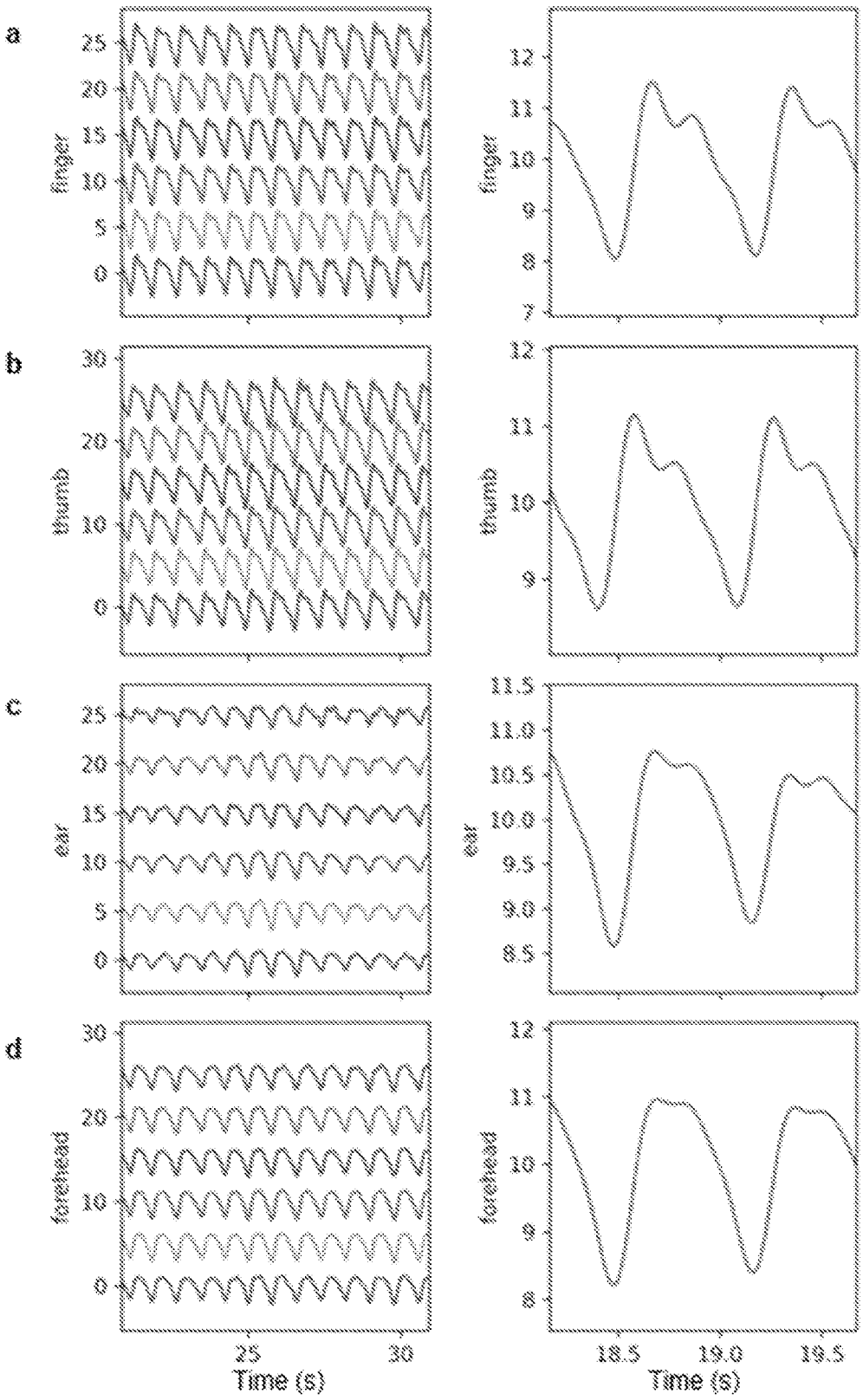


FIG. 4

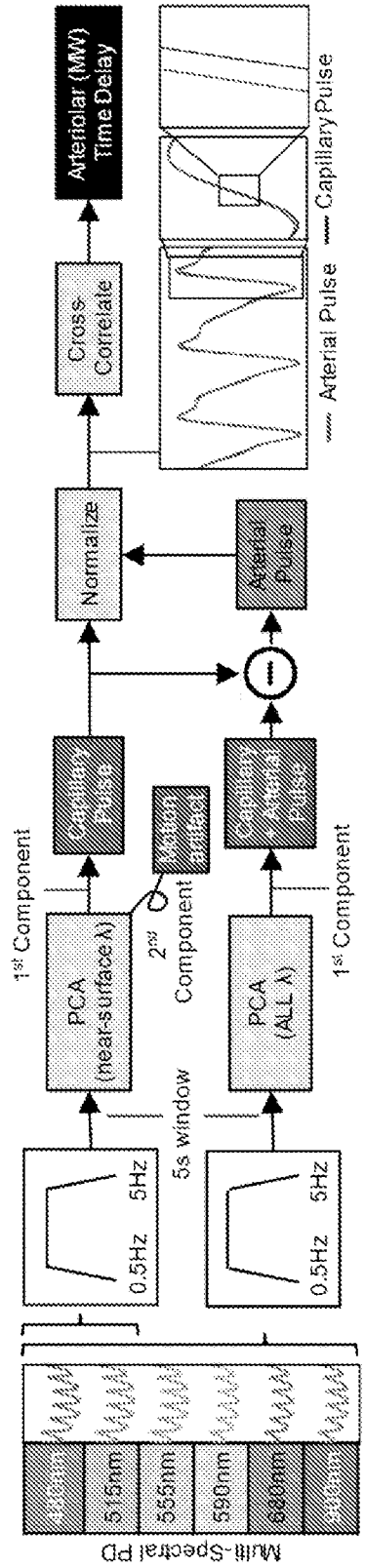

Multi-Spectral PD
525nm
515nm
555nm
590nm
620nm
660nm
0.5Hz 5Hz
0.5Hz 5Hz
5s window
PCA (near-surface λ)
PCA (ALL λ)
1st Component
2nd Component
1st Component
Capillary Pulse
Motion Artifact
Capillary + Arterial Pulse
Arterial Pulse
Normalize
Cross-Correlate
Arteriolar (MW) Time Delay
Arterial Pulse
Capillary Pulse

FIG. 5A

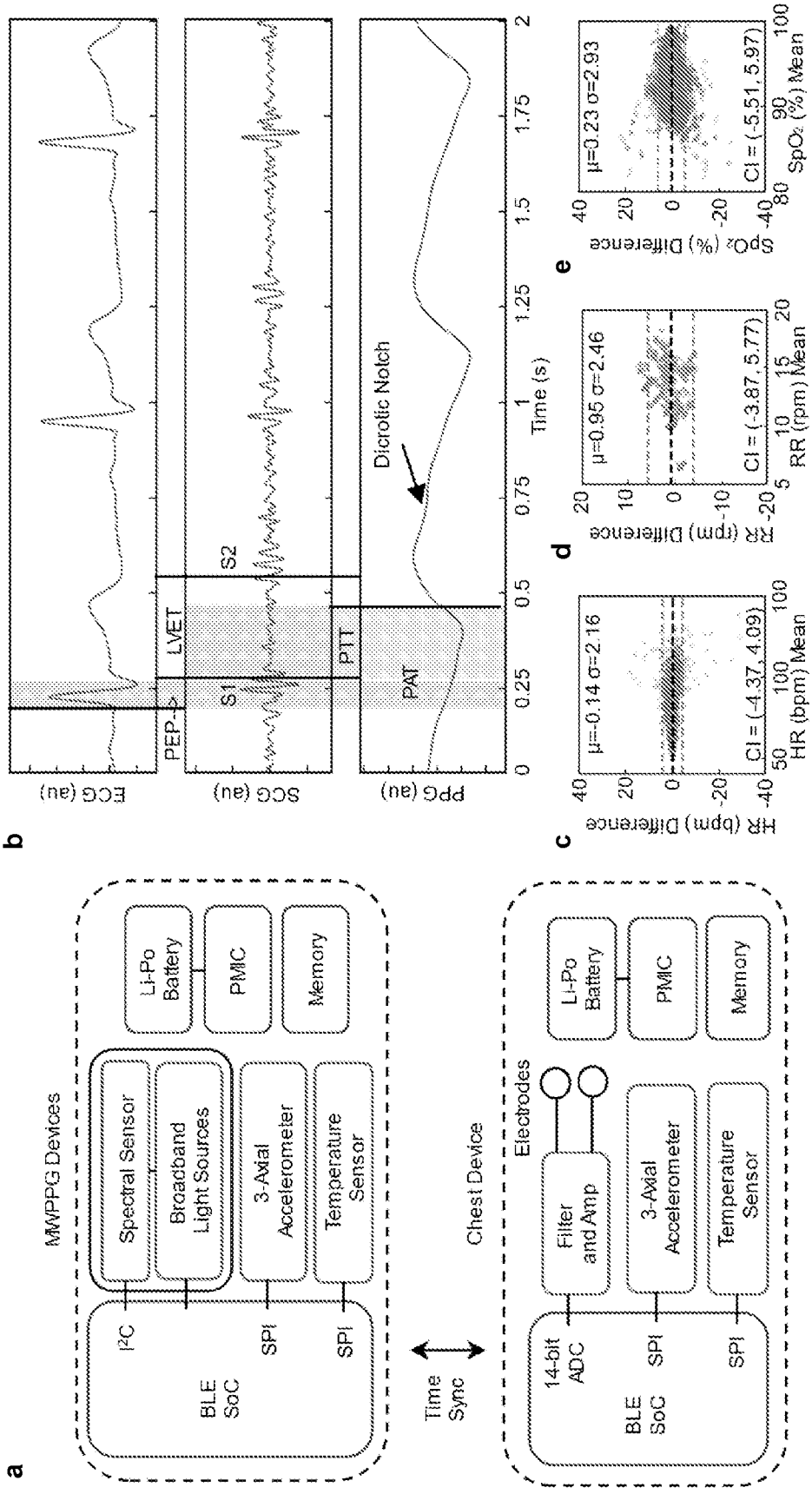

a
MWPPG Devices
Spectral Sensor
Broadband Light Sources
3-Axial Accelerometer
Temperature Sensor
Li-Po Battery
PMIC
Memory
I2C
SPI
SPI
BLE SoC
Time Sync
Chest Device
Electrodes
Filter and Amp
3-Axial Accelerometer
Temperature Sensor
Li-Po Battery
PMIC
Memory
14-bit ADC
SPI
SPI
BLE SoC
b
ECG (au)
SCG (au)
PPG (au)
PEP
LVET
S1
S2
PTT
PAT
Dicrotic Notch
0
0.25
0.5
0.75
1
1.25
1.5
1.75
2
Time (s)
c
HR (bpm) Difference
μ=-0.14 σ=2.16
CI = (-4.37, 4.09)
40
20
0
-20
-40
50
100
100
HR (bpm) Mean
d
RR (rpm) Difference
μ=0.95 σ=2.46
CI = (-3.87, 5.77)
20
10
0
-10
-20
5
10
15
20
RR (rpm) Mean
e
SpO2 (%) Difference
μ=0.23 σ=2.93
CI = (-5.51, 5.97)
40
20
0
-20
-40
80
90
100
SpO2 (%) Mean

FIG. 5B

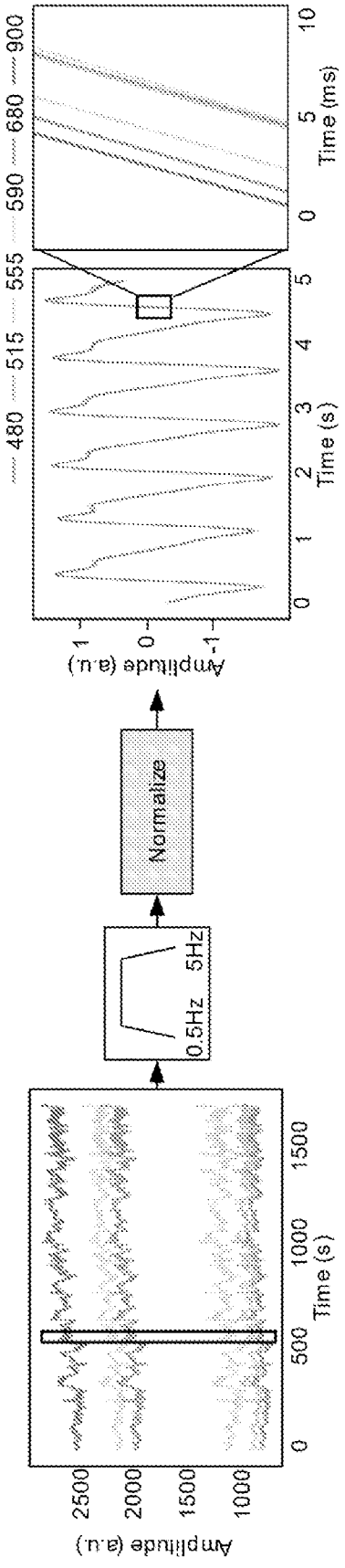

Amplitude (a.u.)
2500
2000
1500
1000
0
500
1000
1500
Time (s)
0.5Hz
5Hz
Normalize
Amplitude (a.u.)
1
0
-1
480
515
555
590
680
900
0
1
2
3
4
5
Time (s)
0
5
10
Time (ms)

FIG. 6A

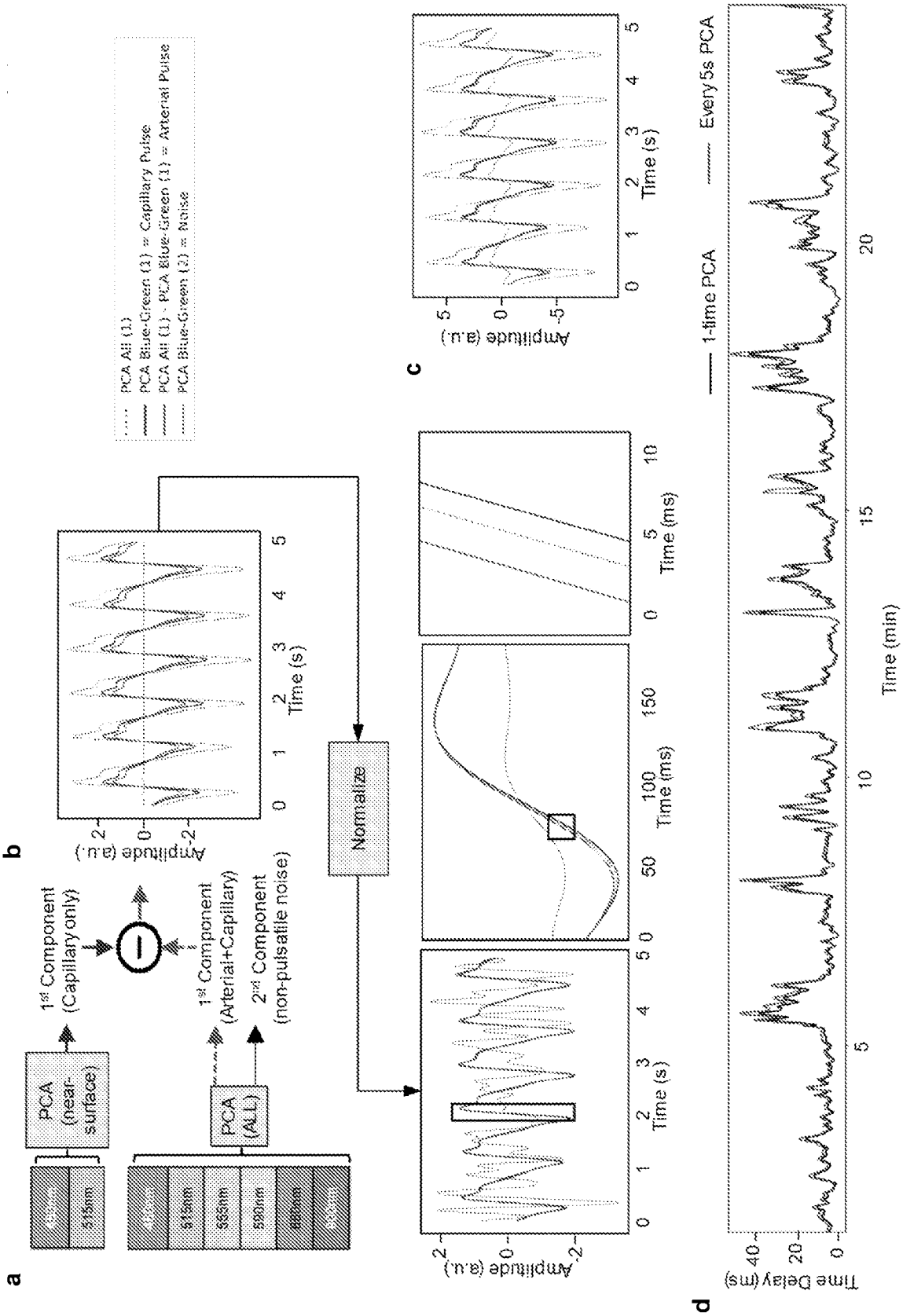
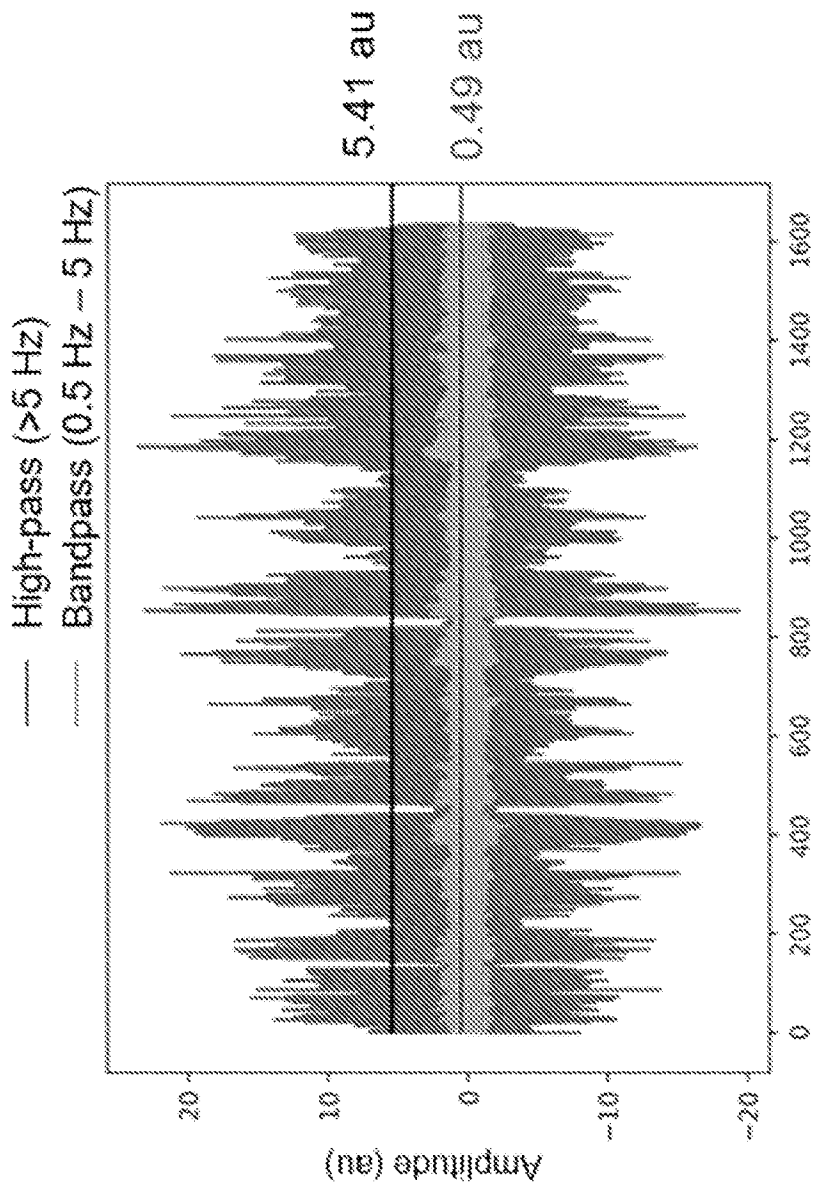
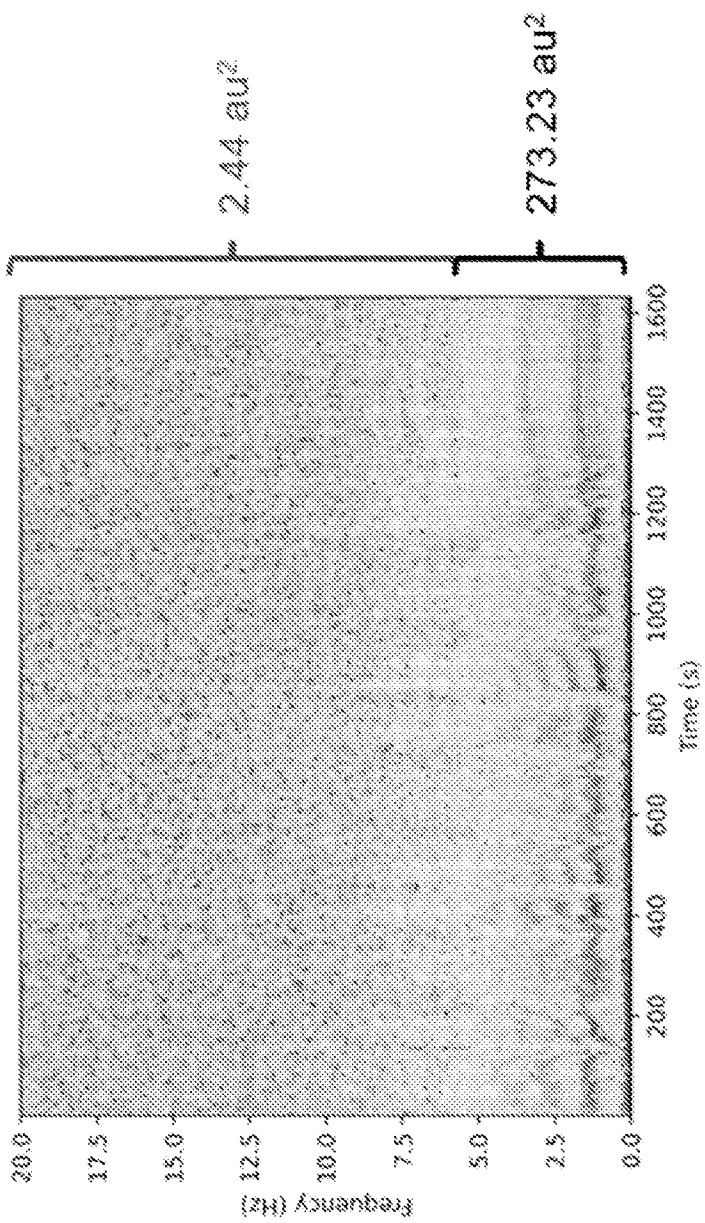

a
PCA (near-surface)
PCA (ALL)
1st Component (Capillary only)
1st Component (Arterial+Capillary)
2nd Component (non-pulsatile noise)
515nm
513nm
563nm
590nm
660nm
Normalize
b
PCA All (1)
PCA Blue-Green (1) = Capillary Pulse
PCA All (1) - PCA Blue-Green (1) = Arterial Pulse
PCA Blue-Green (2) = Noise
Amplitude (a.u.)
Time (s)
c
Amplitude (a.u.)
Time (ms)
Time (s)
d
1-time PCA
Every 5s PCA
Time Delay (ms)
Time (min)

FIG. 6B



$$SNR = 20 * \log_{10} \frac{5.41\ au}{0.49\ au} = 20.86\ \text{dB}$$

FIG. 7A



$$SNR = 10 * \log_{10} \frac{273.23\ au^2}{2.44\ W\ au^2} = 20.49\ \text{dB}$$

FIG. 7B

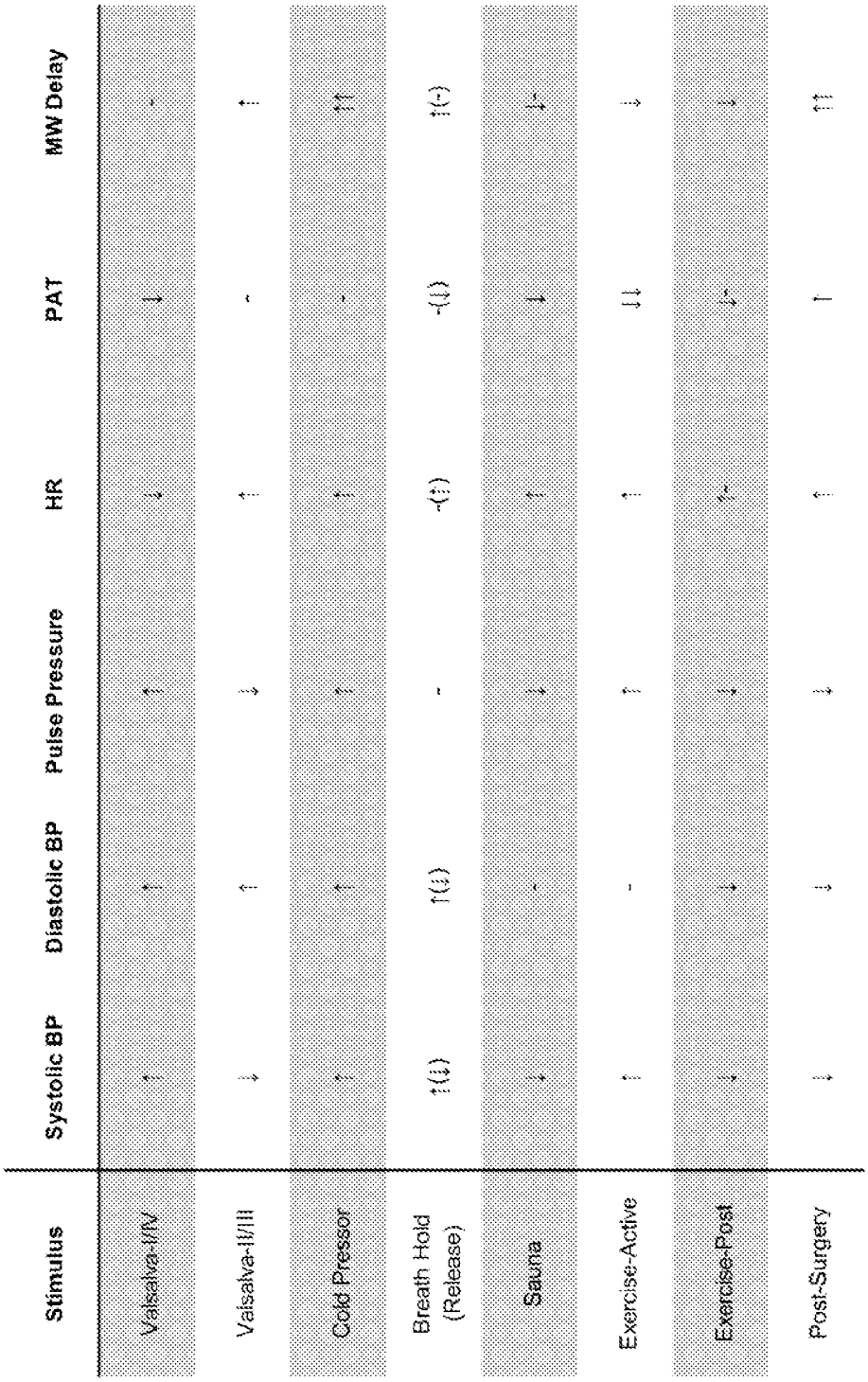

Stimulus
Systolic BP
Diastolic BP
Pulse Pressure
HR
PAT
MW Delay
Valsalva-I/IV
Valsalva-II/III
Cold Pressor
Breath Hold (Release)
Sauna
Exercise-Active
Exercise-Post
Post-Surgery

FIG. 8

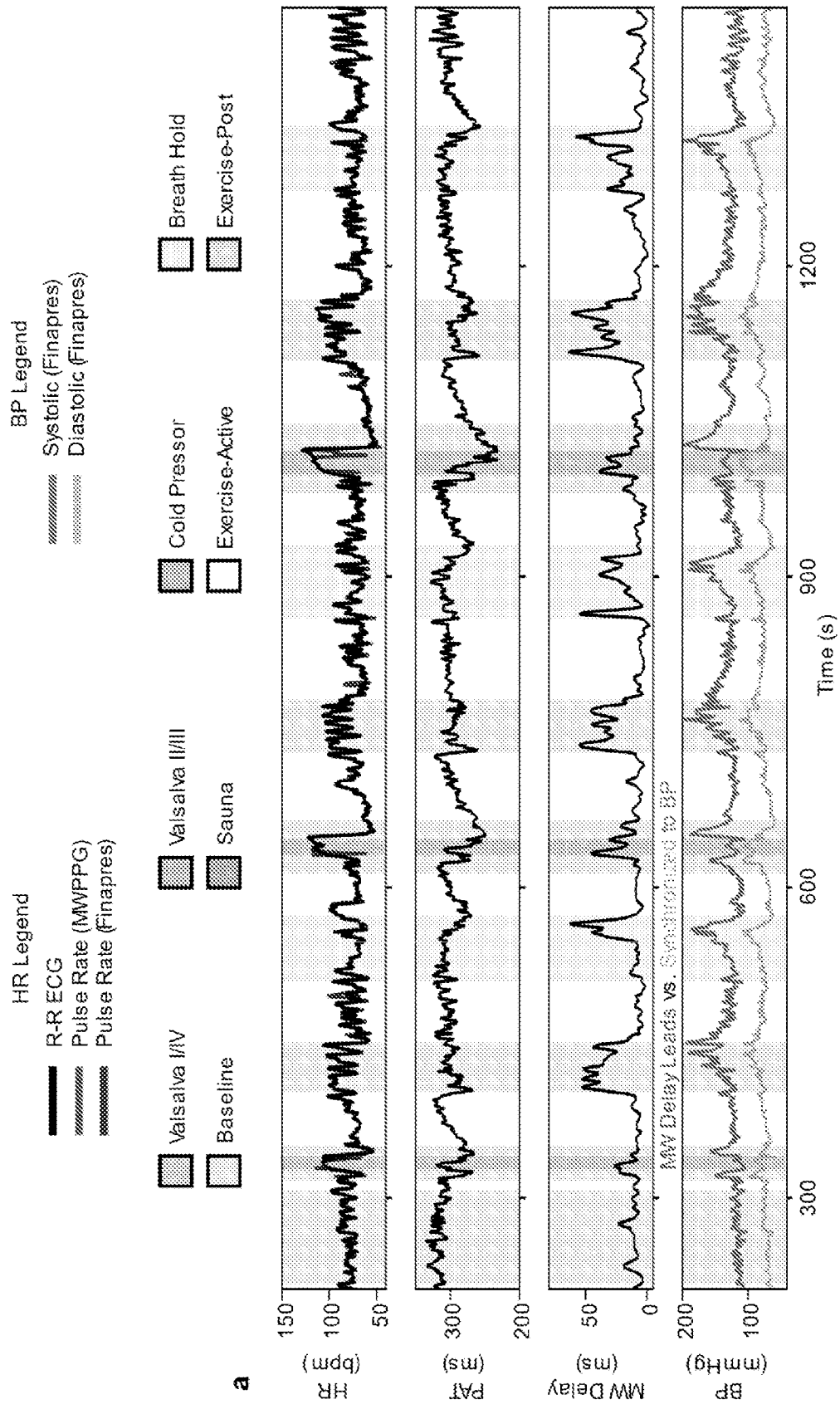

HR Legend
R-R ECG
Pulse Rate (MVPPG)
Pulse Rate (Finapres)
Valsalva I/IV
Baseline
Valsalva II/III
Sauna
Cold Pressor
Exercise-Active
Breath Hold
Exercise-Post
BP Legend
Systolic (Finapres)
Diastolic (Finapres)
a
HR (bpm)
PAT (ms)
MW Delay (ms)
BP (mmHg)
MW Delay Leads vs. Synchronized to BP
Time (s)

FIG. 9A

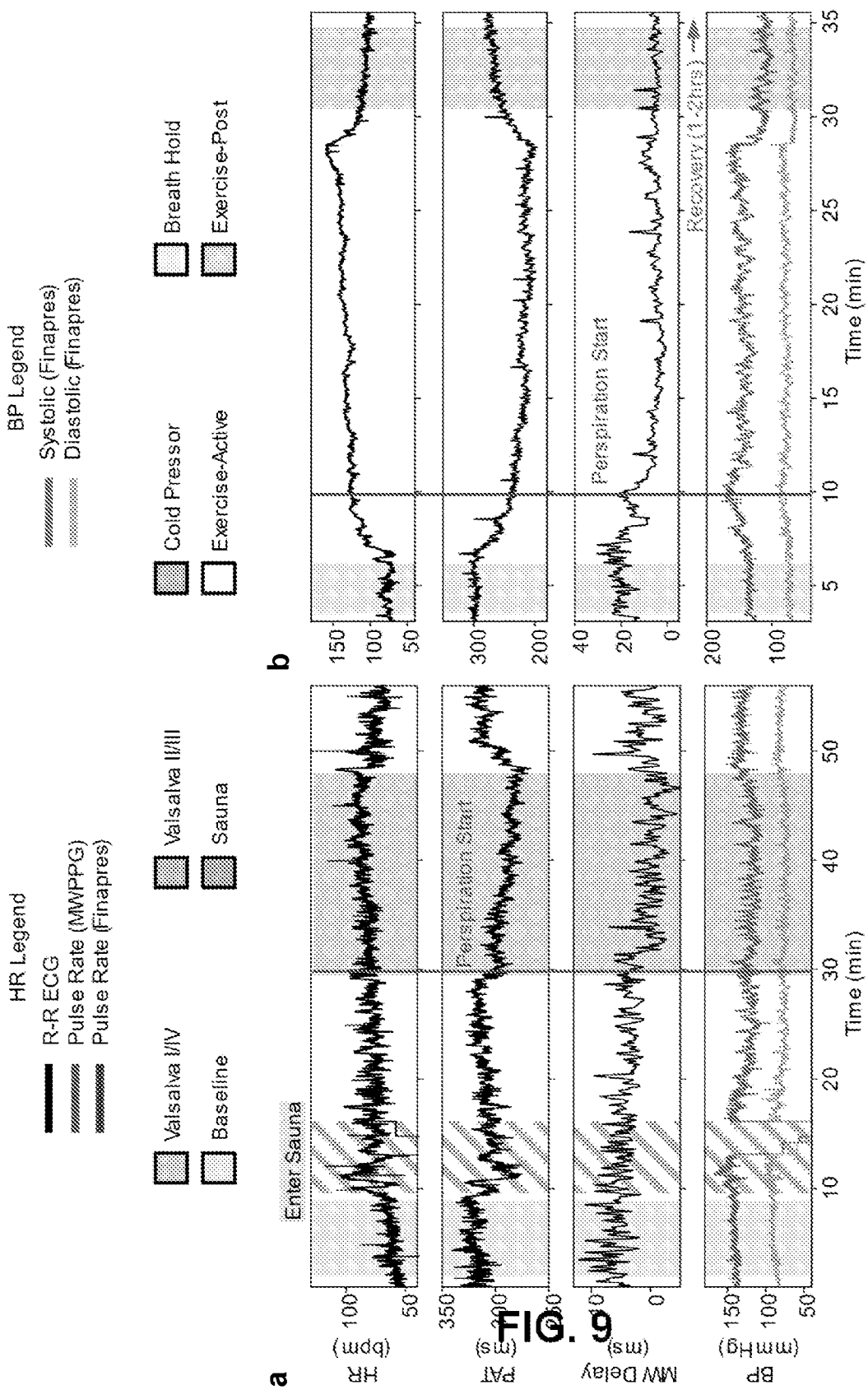

HR Legend
R-R ECG
Pulse Rate (MWPPG)
Pulse Rate (Finapres)
BP Legend
Systolic (Finapres)
Diastolic (Finapres)
Valsalva I/IV
Baseline
Valsalva II/III
Sauna
Cold Pressor
Exercise-Active
Breath Hold
Exercise-Post
a
b
Enter Sauna
Perspiration Start
Recovery (1-2hrs)
HR (bpm)
PAT (ms)
MW Delay (ms)
BP (mmHg)
Time (min)

FIG. 9B

FIG. 9

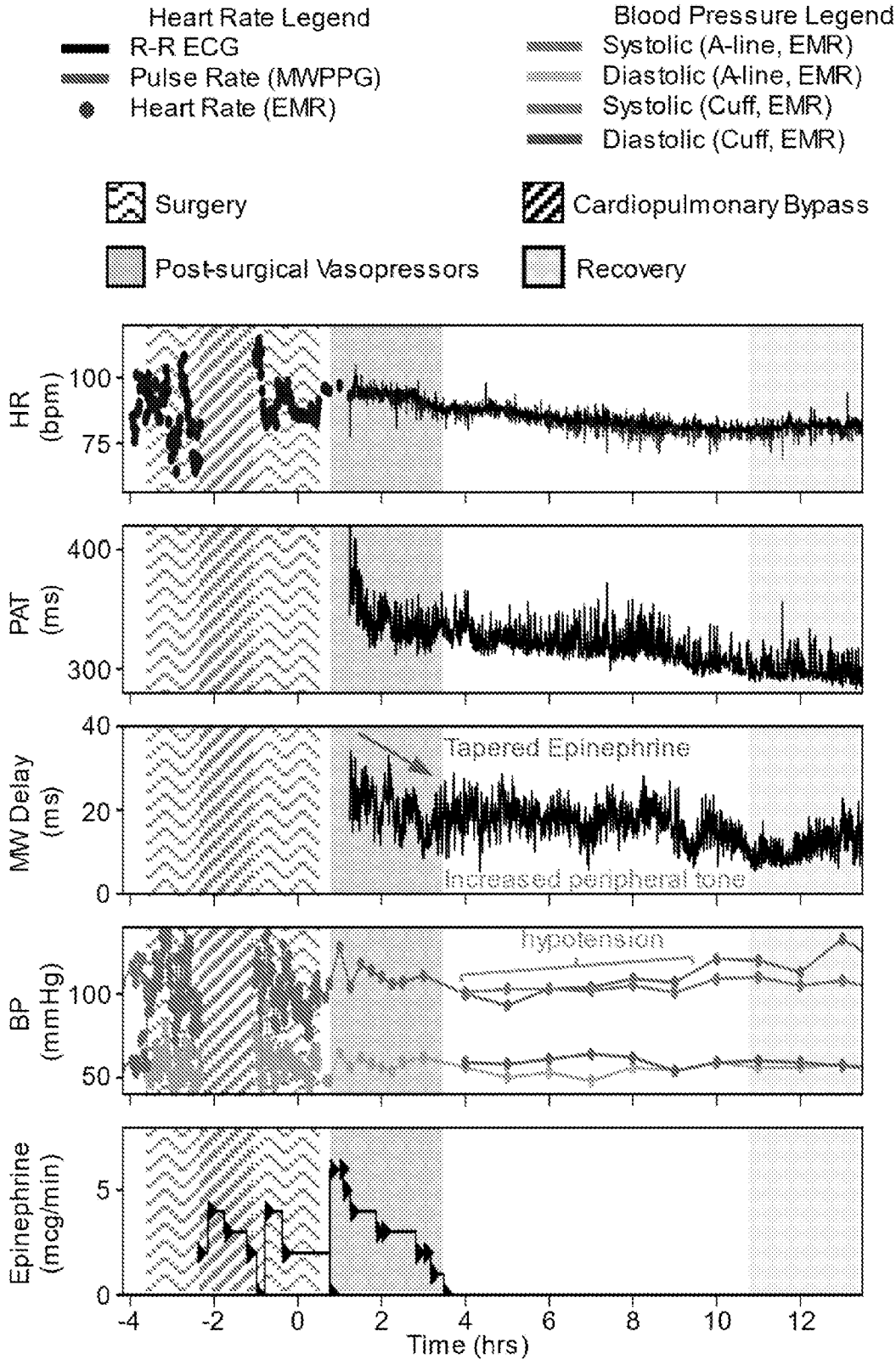

Heart Rate Legend
R-R ECG
Pulse Rate (MWPPG)
Heart Rate (EMR)
Blood Pressure Legend
Systolic (A-line, EMR)
Diastolic (A-line, EMR)
Systolic (Cuff, EMR)
Diastolic (Cuff, EMR)
Surgery
Cardiopulmonary Bypass
Post-surgical Vasopressors
Recovery
HR (bpm)
100
75
PAT (ms)
400
300
MW Delay (ms)
40
20
0
Tapered Epinephrine
Increased peripheral tone
BP (mmHg)
100
50
hypotension
Epinephrine (mcg/min)
5
0
-4
-2
0
2
4
6
8
10
12
Time (hrs)

FIG. 10

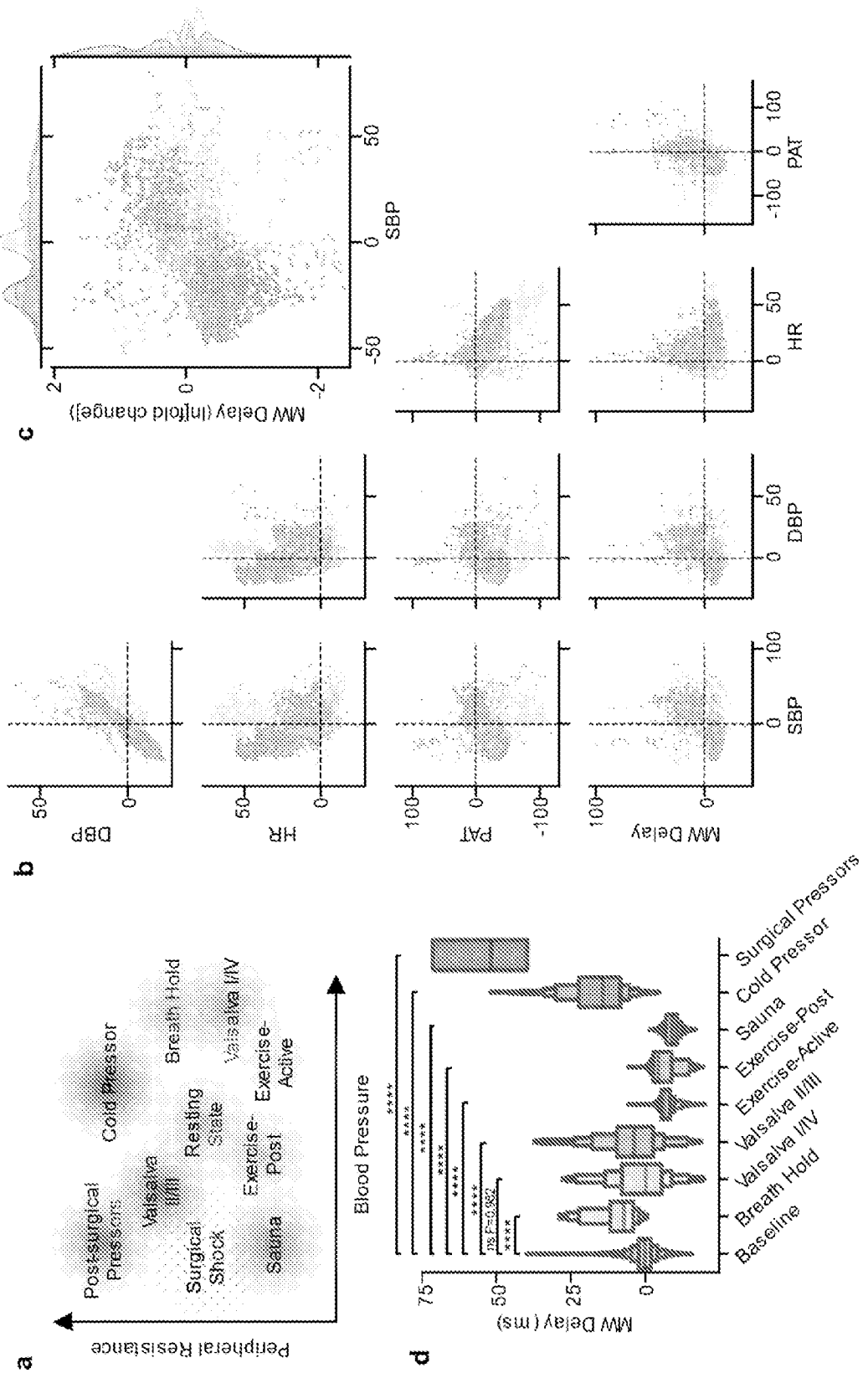

a
Peripheral Resistance
Blood Pressure
Post-surgical Pressors
Cold Pressor
Breath Hold
Valsalva I/III
Resting State
Valsalva I/IV
Surgical Shock
Exercise-Post
Exercise-Active
Sauna
b
DBP
HR
PAT
MW Delay
SBP
DBP
HR
PAT
MW Delay
SBP
c
MW Delay (Infold change)
SBP
HR
PAT
d
MW Delay (ms)
Surgical Pressors
Cold Pressor
Sauna
Exercise-Post
Exercise-Active
Valsalva II/III
Valsalva I/IV
Breath Hold
Baseline

FIG. 11

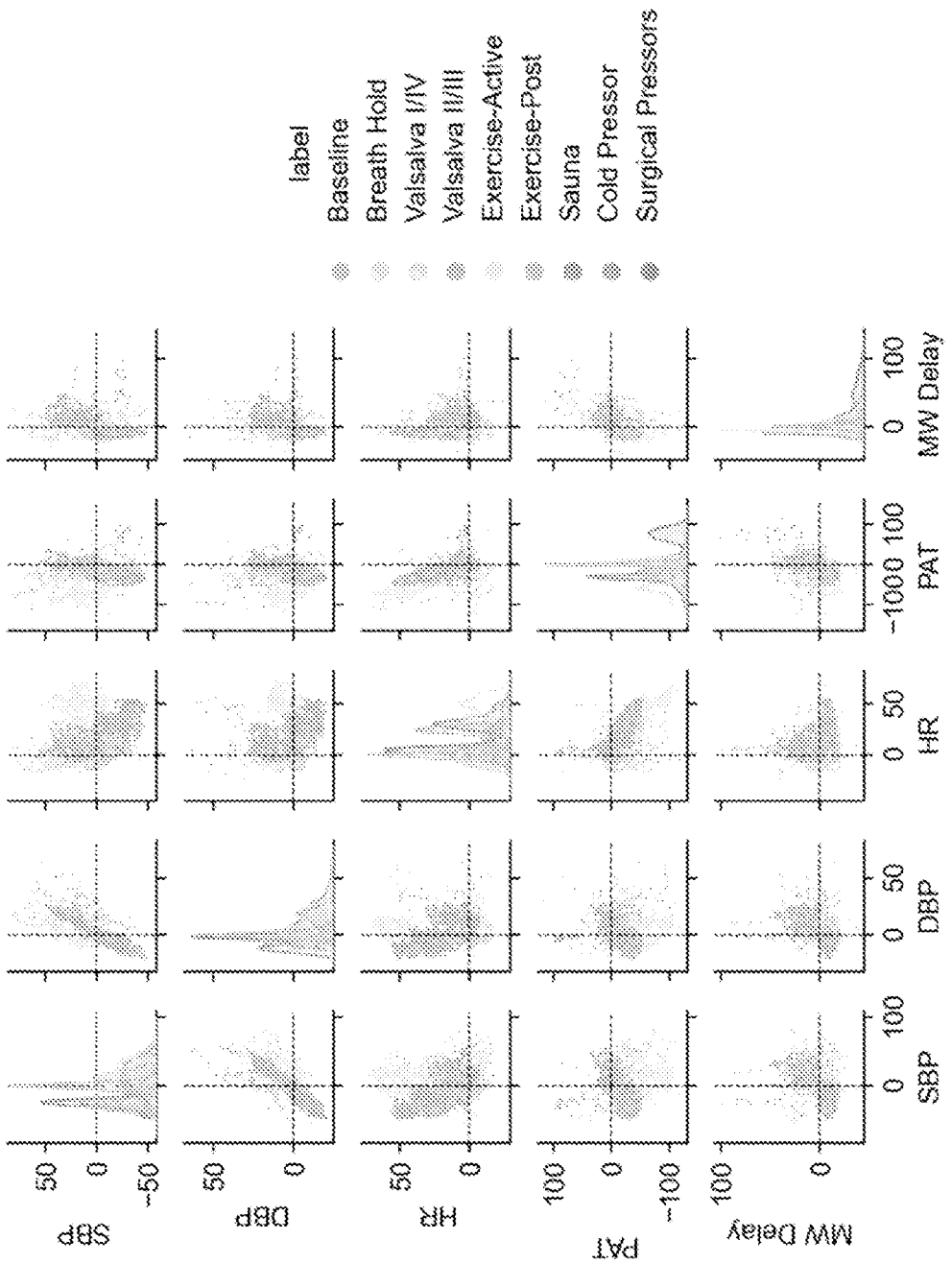

label
Baseline
Breath Hold
Valsalva I/IV
Valsalva II/III
Exercise-Active
Exercise-Post
Sauna
Cold Pressor
Surgical Pressors
SBP
DBP
HR
PAT
MW Delay
50
0
−50
100
−100
−1000
SBP
DBP
HR
PAT
MW Delay

FIG. 12A

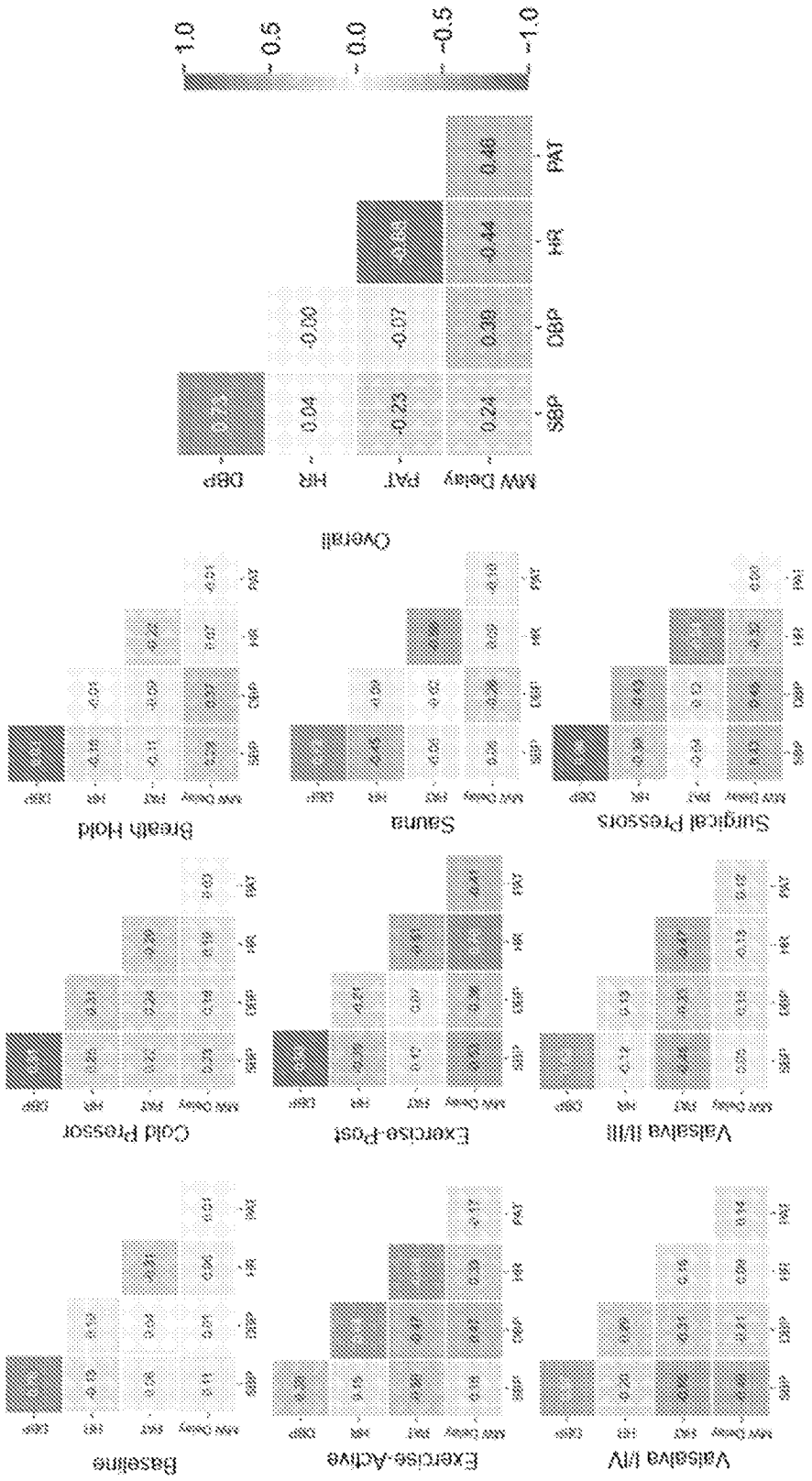

1.0
0.5
0.0
-0.5
-1.0
Overall
Baseline
Exercise-Active
Valsalva I/V
Cold Pressor
Exercise-Post
Valsalva II/III
Breath Hold
Sauna
Surgical Pressors
DBP
HR
PAT
MW Delay
SBP
DBP
HR
PAT

FIG. 12A

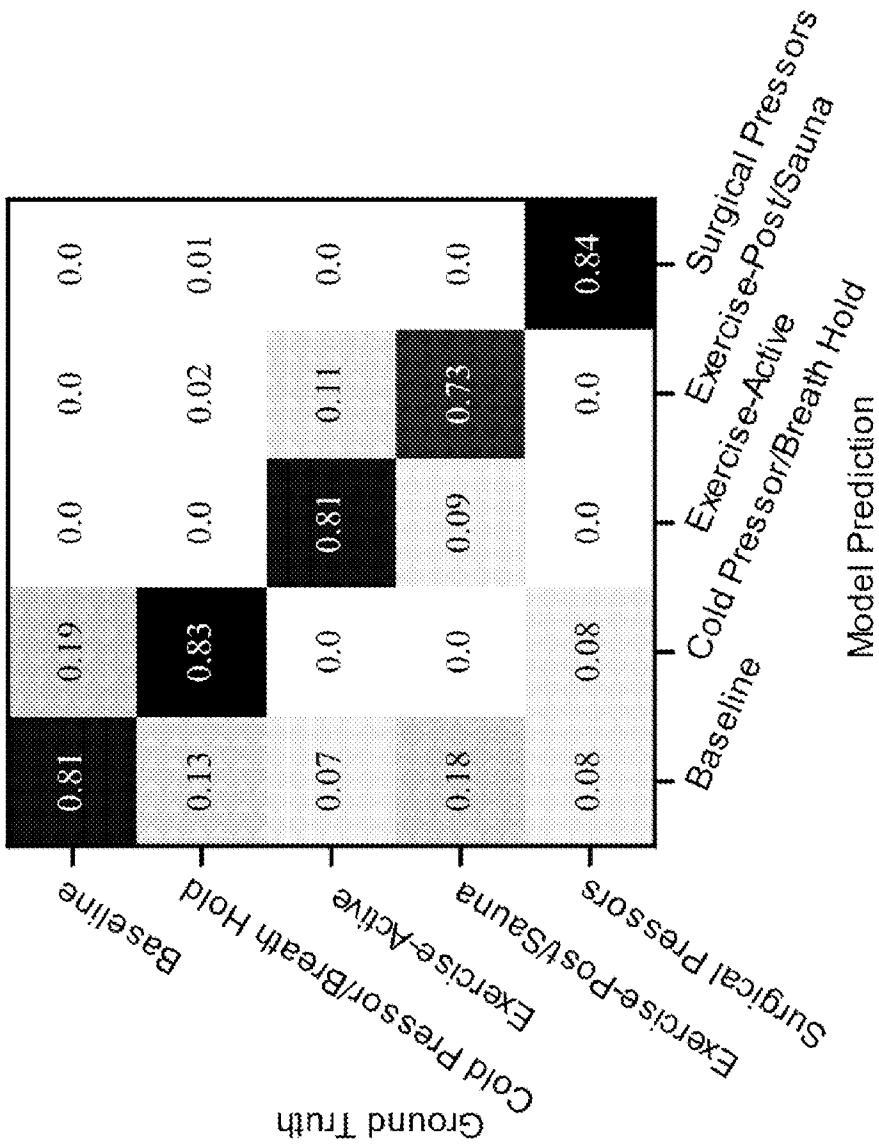

Ground Truth
Baseline
Cold Pressor/Breath Hold
Exercise-Active
Exercise-Post/Sauna
Surgical Pressors
0.81 0.19 0.0 0.0 0.0
0.13 0.83 0.0 0.0 0.01
0.07 0.0 0.81 0.11 0.0
0.18 0.0 0.09 0.73 0.0
0.08 0.08 0.0 0.0 0.84
Baseline
Cold Pressor/Breath Hold
Exercise-Active
Exercise-Post/Sauna
Surgical Pressors
Model Prediction

FIG. 13A

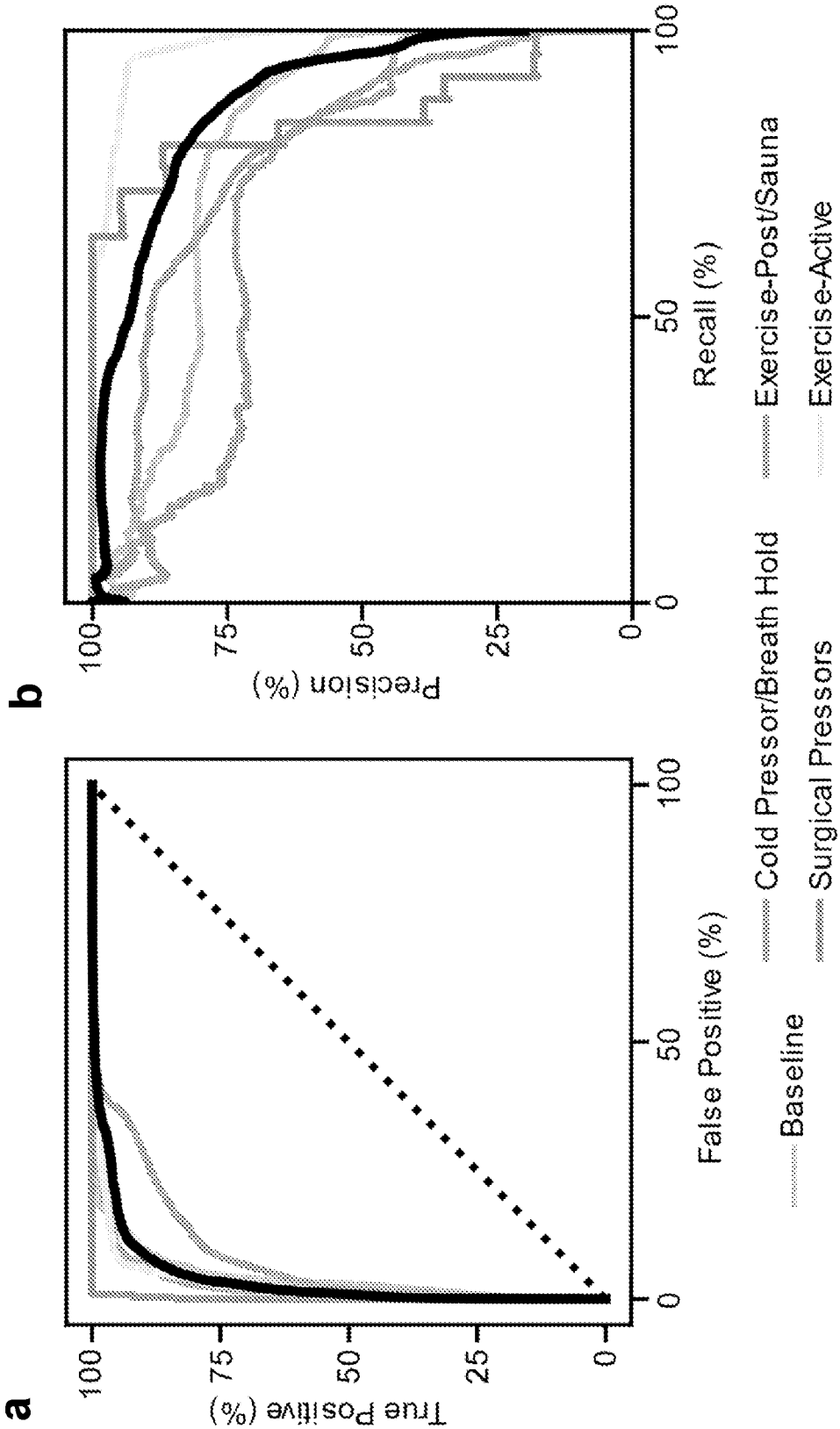

a
True Positive (%)
0
25
50
75
100
0
50
100
False Positive (%)
b
Precision (%)
0
25
50
75
100
0
50
100
Recall (%)
Baseline
Cold Pressor/Breath Hold
Surgical Pressors
Exercise-Post/Sauna
Exercise-Active

FIG. 13B

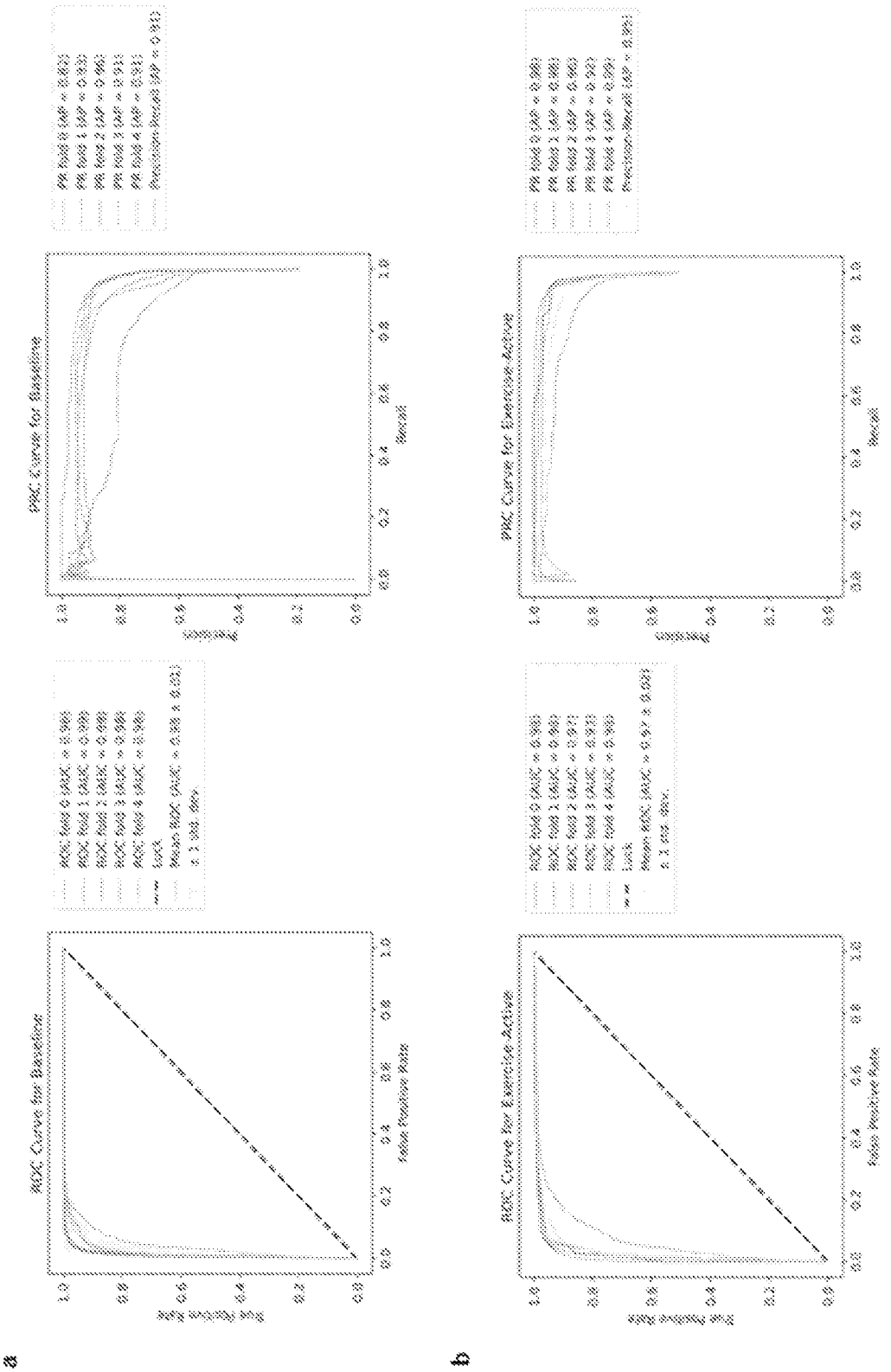

a
b
ROC Curve for Baseline
PRC Curve for Baseline
ROC Curve for Exercise Active
PRC Curve for Exercise Active
True Positive Rate
False Positive Rate
Precision
Recall

FIG. 14A

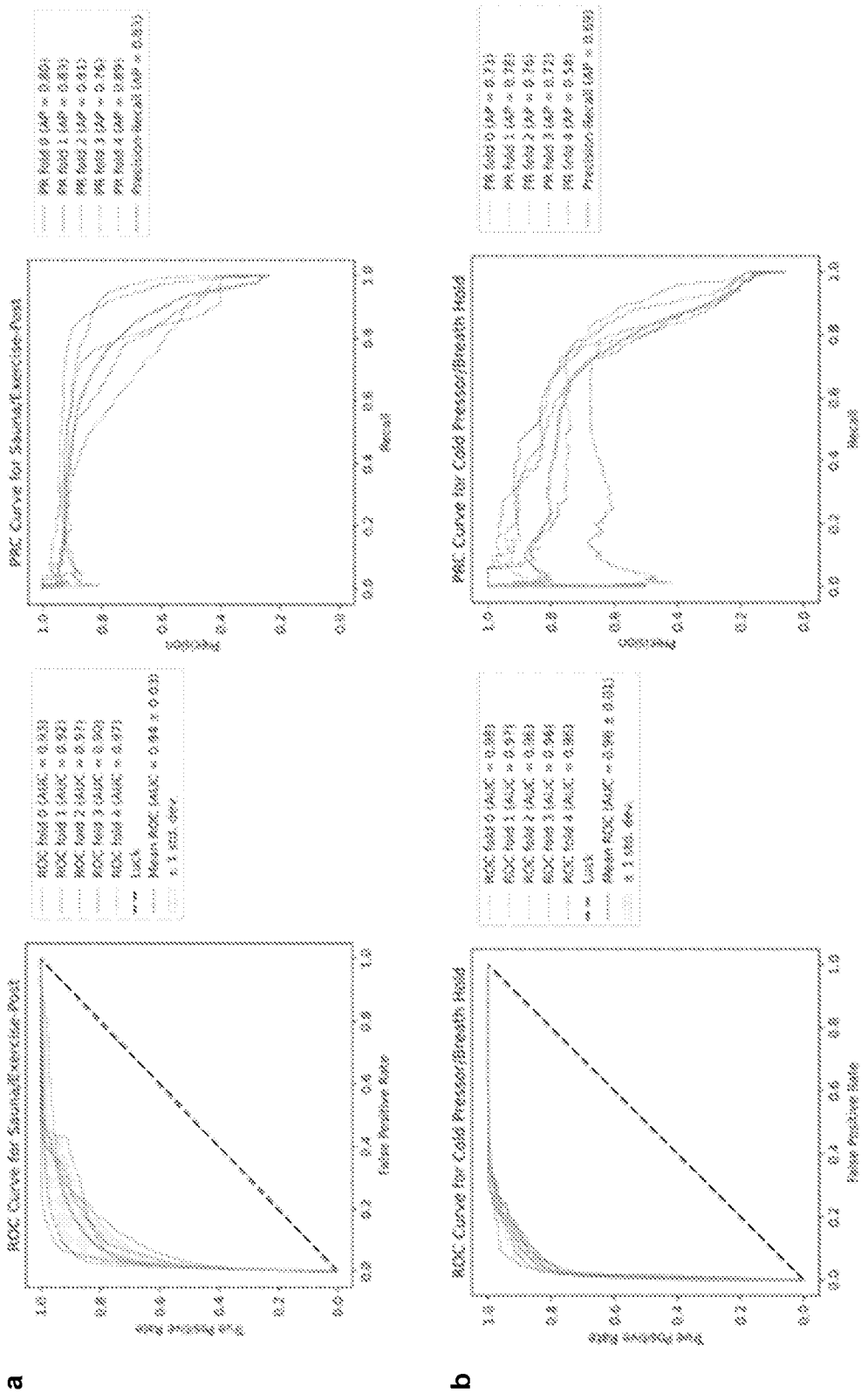

a
b
ROC Curve for Sexual Function Pred
PRC Curve for Sexual Function Pred
ROC Curve for Cold Pressor/Breath Hold
PRC Curve for Cold Pressor/Breath Hold
True Positive Rate
False Positive Rate
Precision
Recall

FIG. 14B

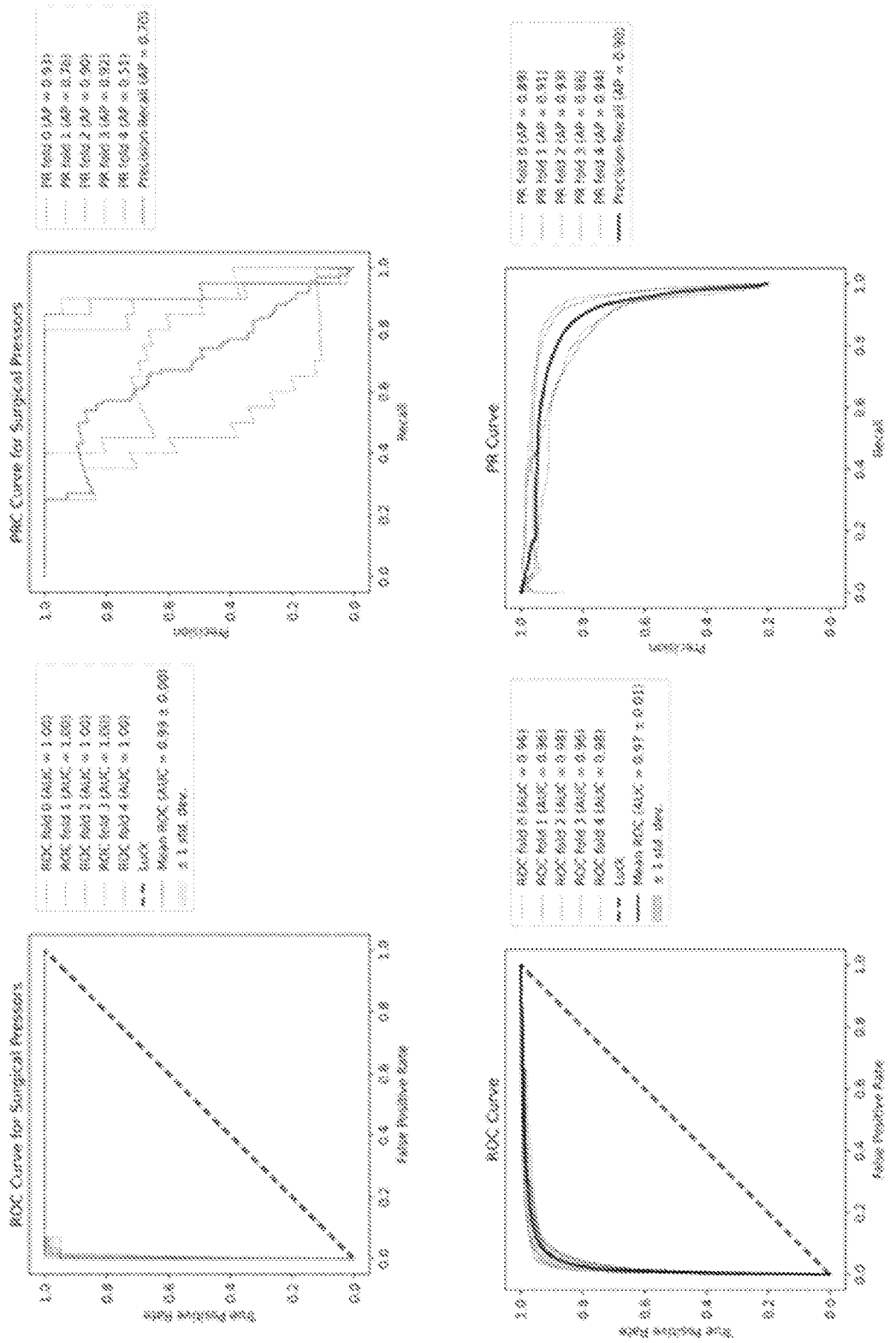
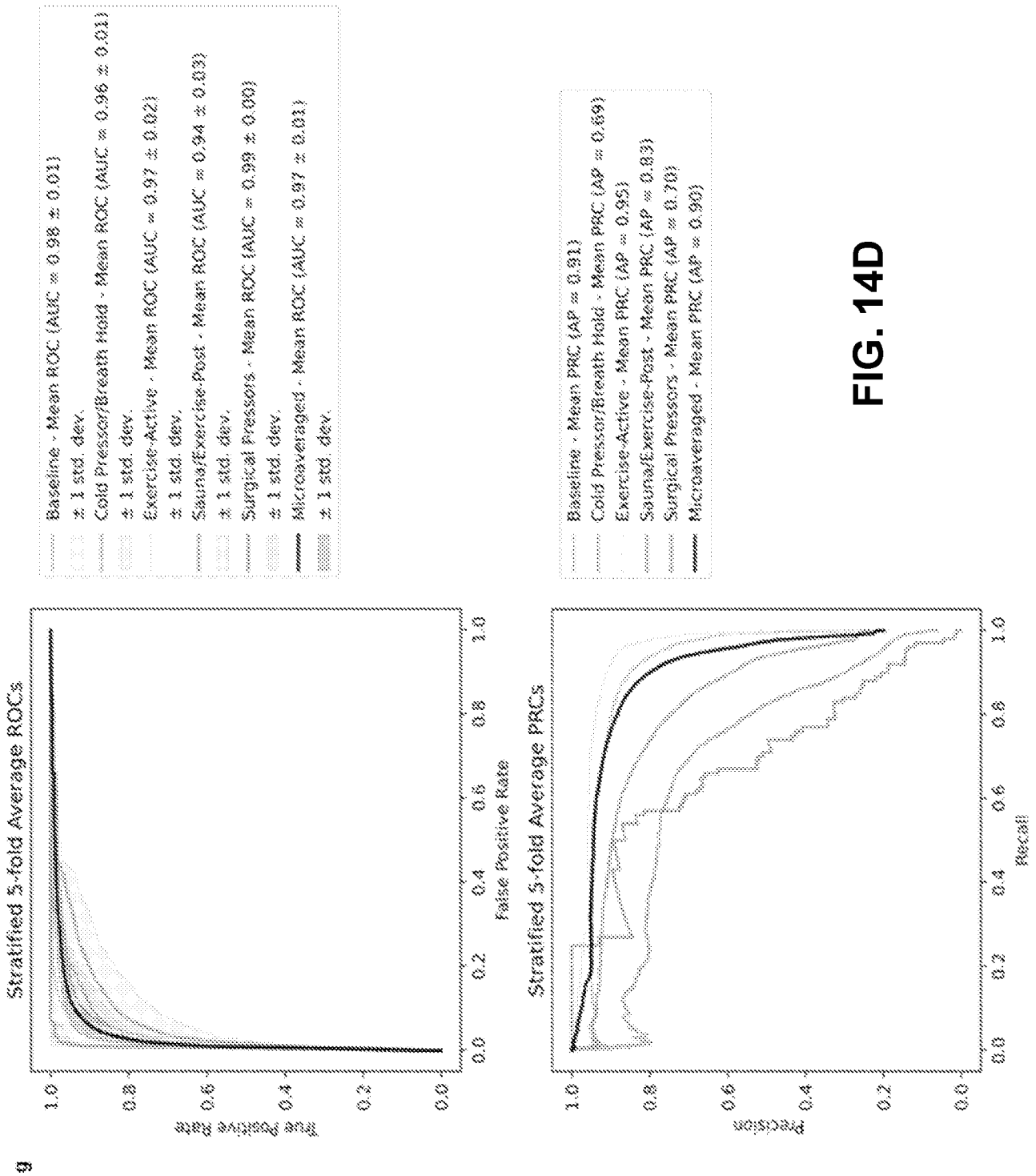

ROC Curve for Surgical Pressure
True Positive Rate
False Positive Rate
ROC fold 0 (AUC = 1.00)
ROC fold 1 (AUC = 1.00)
ROC fold 2 (AUC = 1.00)
ROC fold 3 (AUC = 1.00)
ROC fold 4 (AUC = 1.00)
Luck
Mean ROC (AUC = 0.99 ± 0.00)
± 1 std. dev.
PR Curve for Surgical Pressure
Precision
Recall
PR fold 0 (AP = 0.93)
PR fold 1 (AP = 0.93)
PR fold 2 (AP = 0.90)
PR fold 3 (AP = 0.92)
PR fold 4 (AP = 0.51)
Precision-Recall (AP = 0.79)
ROC Curve
True Positive Rate
False Positive Rate
ROC fold 0 (AUC = 0.96)
ROC fold 1 (AUC = 0.96)
ROC fold 2 (AUC = 0.98)
ROC fold 3 (AUC = 0.96)
ROC fold 4 (AUC = 0.98)
Luck
Mean ROC (AUC = 0.97 ± 0.01)
± 1 std. dev.
PR Curve
Precision
Recall
PR fold 0 (AP = 0.88)
PR fold 1 (AP = 0.91)
PR fold 2 (AP = 0.93)
PR fold 3 (AP = 0.93)
PR fold 4 (AP = 0.94)
Precision-Recall (AP = 0.90)

FIG. 14C


Stratified 5-fold Average ROCs
True Positive Rate
False Positive Rate
Baseline - Mean ROC (AUC = 0.98 ± 0.01)
± 1 std. dev.
Cold Pressor/Breath Hold - Mean ROC (AUC = 0.96 ± 0.01)
± 1 std. dev.
Exercise-Active - Mean ROC (AUC = 0.97 ± 0.02)
± 1 std. dev.
Sauna/Exercise-Post - Mean ROC (AUC = 0.94 ± 0.03)
± 1 std. dev.
Surgical Pressors - Mean ROC (AUC = 0.99 ± 0.00)
± 1 std. dev.
Microaveraged - Mean ROC (AUC = 0.97 ± 0.01)
± 1 std. dev.
Stratified 5-fold Average PRCs
Precision
Recall
Baseline - Mean PRC (AP = 0.91)
Cold Pressor/Breath Hold - Mean PRC (AP = 0.69)
Exercise-Active - Mean PRC (AP = 0.95)
Sauna/Exercise-Post - Mean PRC (AP = 0.83)
Surgical Pressors - Mean PRC (AP = 0.70)
Microaveraged - Mean PRC (AP = 0.90)

g

FIG. 14D

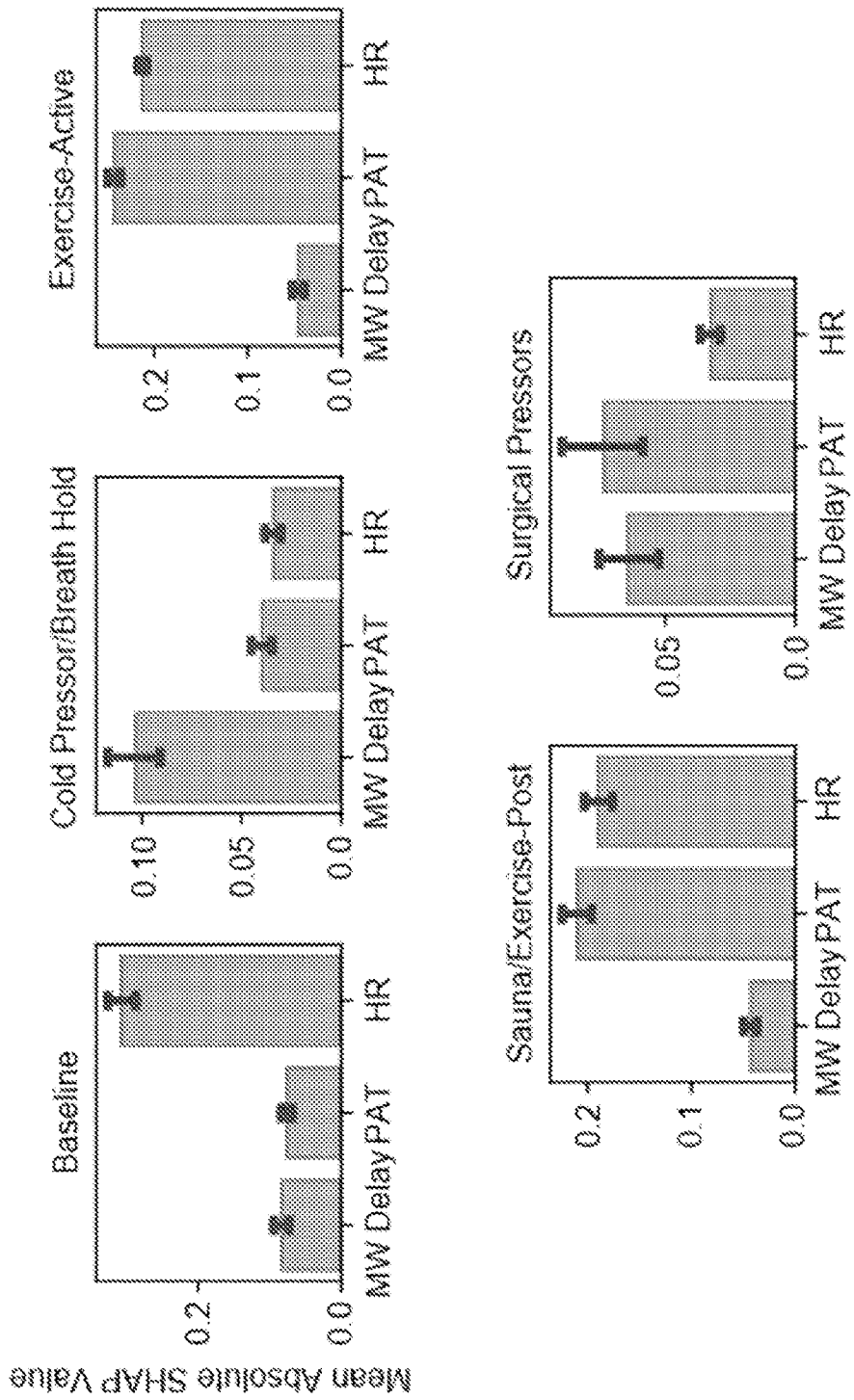
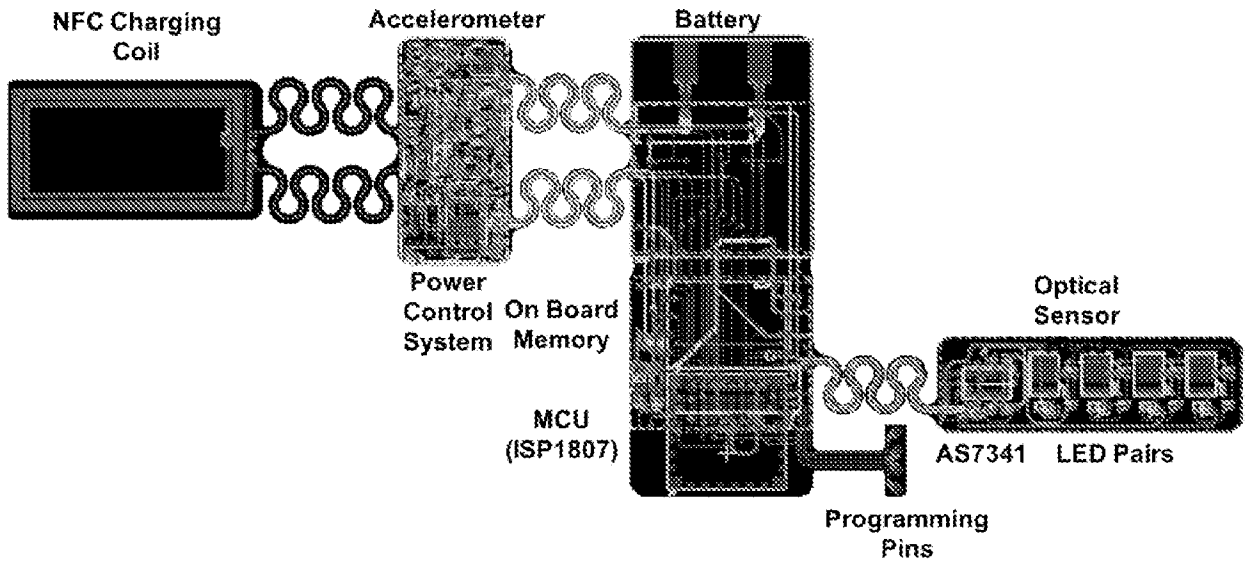

Mean Absolute SHAP Value
Baseline
Cold Pressor/Breath Hold
Exercise-Active
Sauna/Exercise-Post
Surgical Pressors
MW Delay PAT HR
0.0
0.05
0.10
0.1
0.2

FIG. 15

a


NFC Charging Coil
Accelerometer
Battery
Power Control System
On Board Memory
MCU (ISP1807)
Optical Sensor
AS7341
LED Pairs
Programming Pins

b

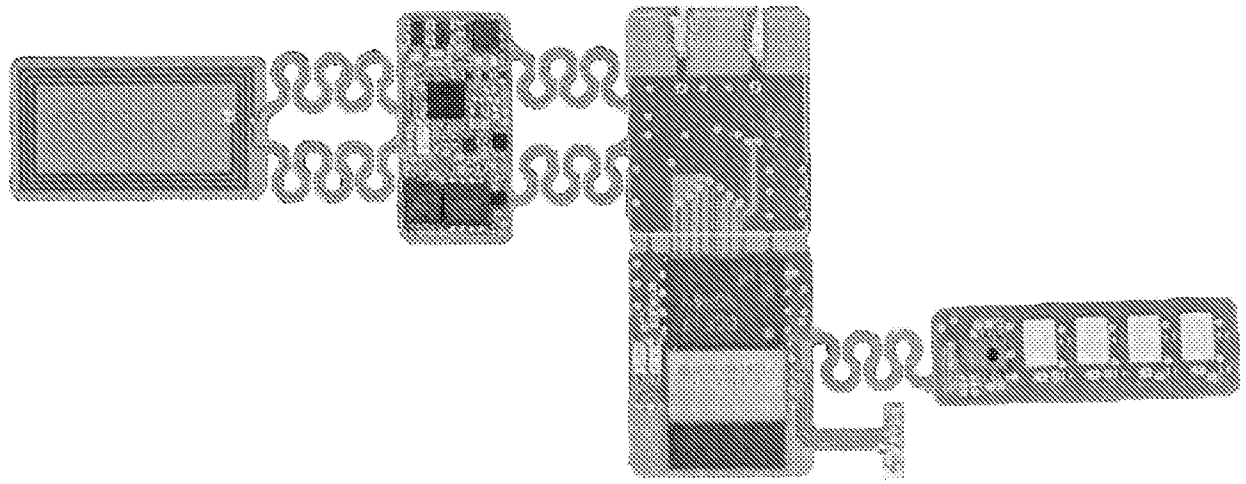


FIG. 16

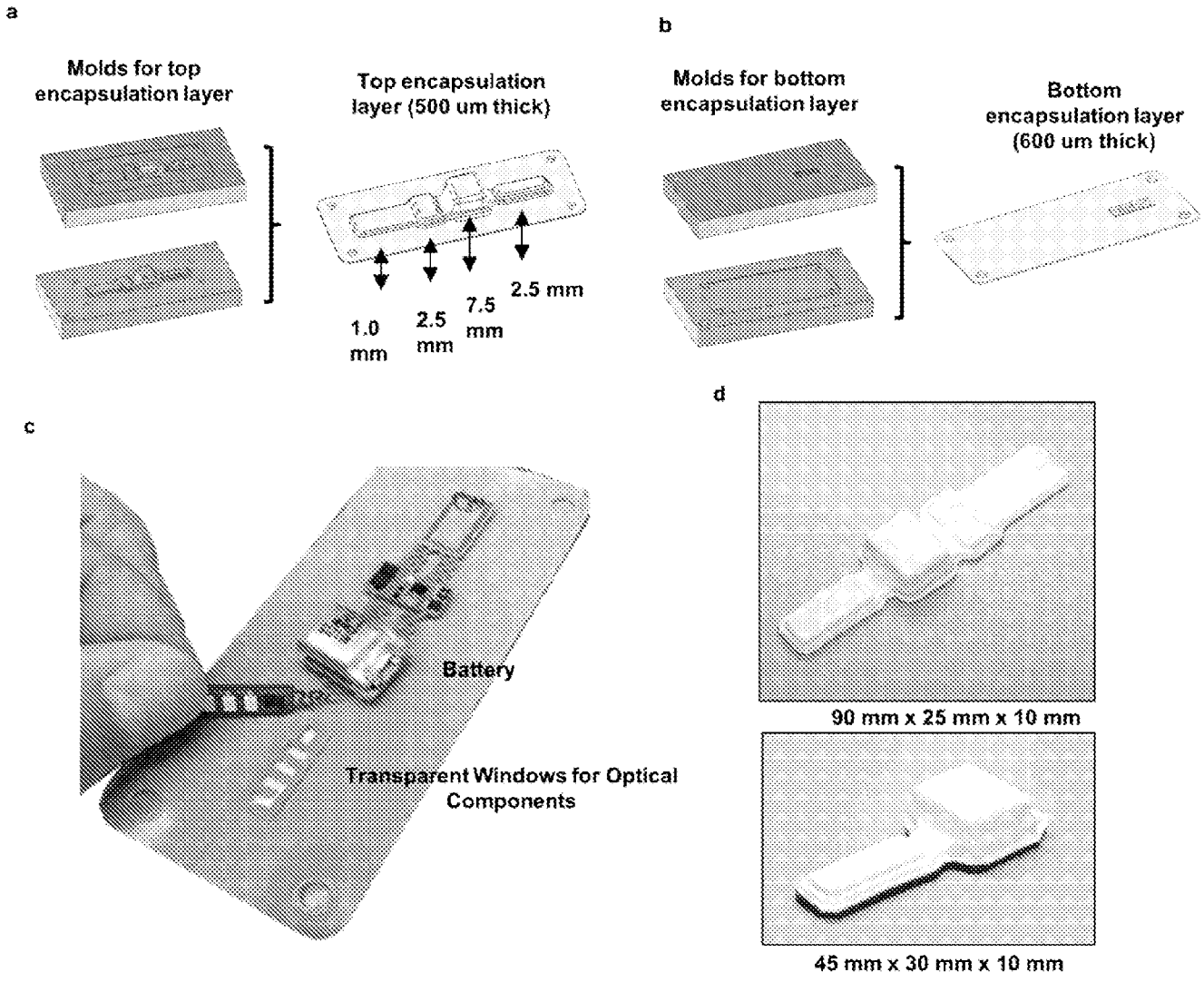

a
Molds for top encapsulation layer
Top encapsulation layer (500 um thick)
1.0 mm
2.5 mm
7.5 mm
2.5 mm
b
Molds for bottom encapsulation layer
Bottom encapsulation layer (600 um thick)
c
Battery
Transparent Windows for Optical Components
d
90 mm x 25 mm x 10 mm
45 mm x 30 mm x 10 mm

FIG. 17

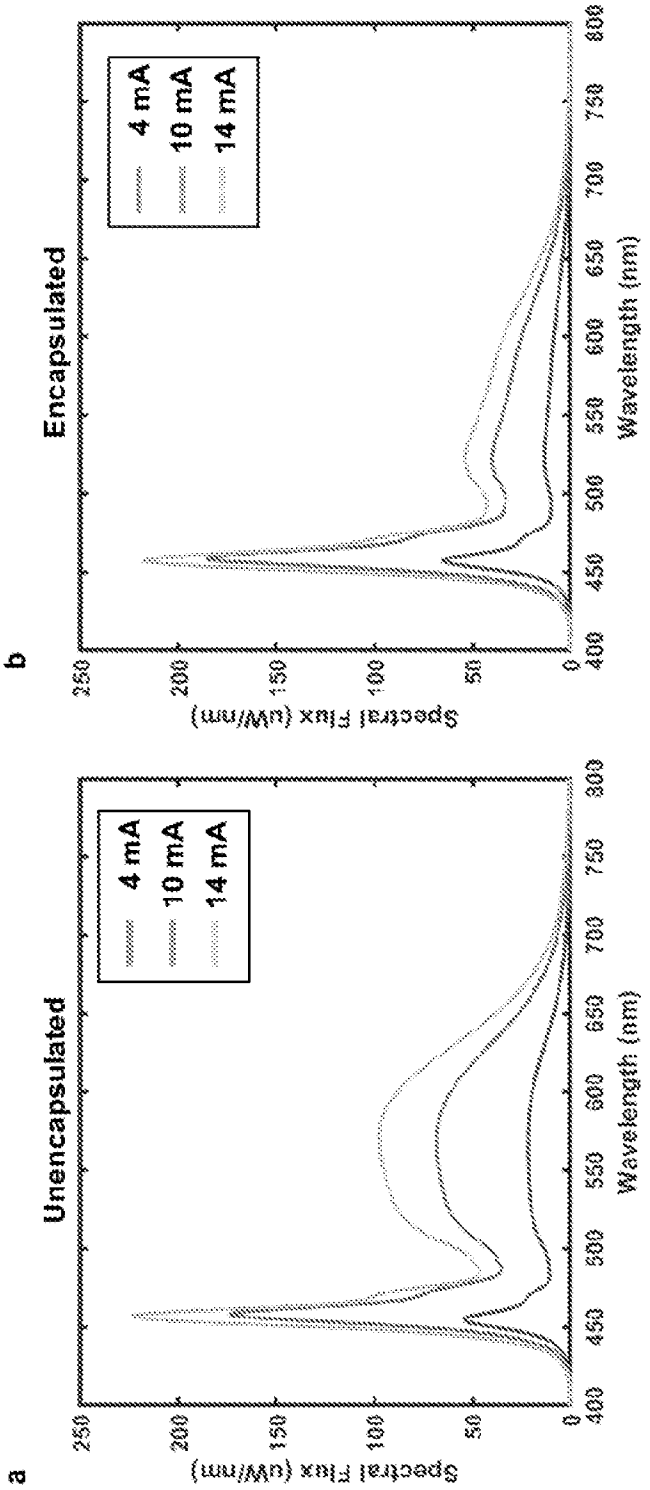

a
Unencapsulated
4 mA
10 mA
14 mA
Spectral Flux (uW/nm)
Wavelength (nm)
b
Encapsulated
4 mA
10 mA
14 mA
Spectral Flux (uW/nm)
Wavelength (nm)

FIG. 18

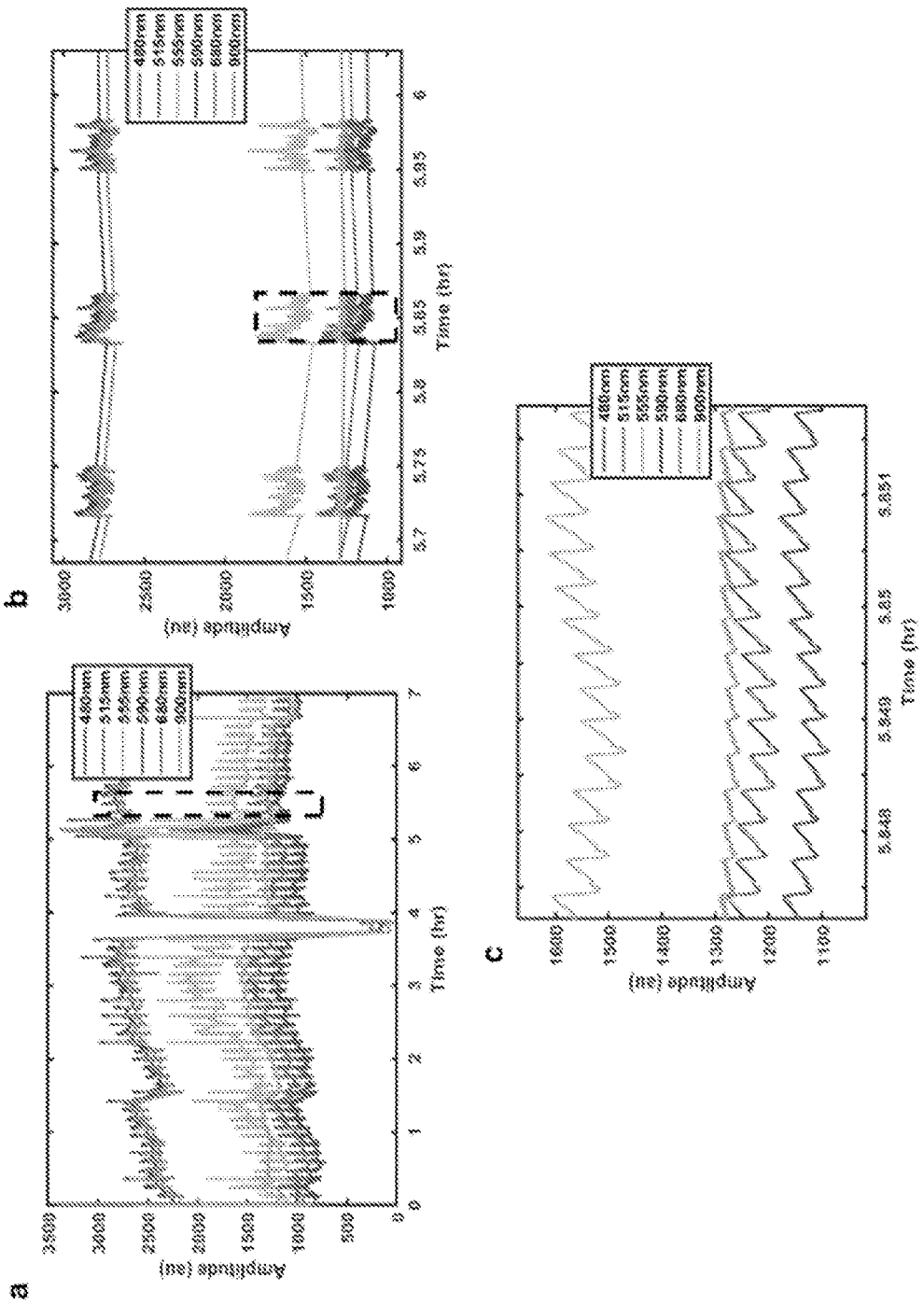

a
b
c
Amplitude (au)
Time (hr)
480nm
515nm
555nm
590nm
680nm
900nm

FIG. 19A

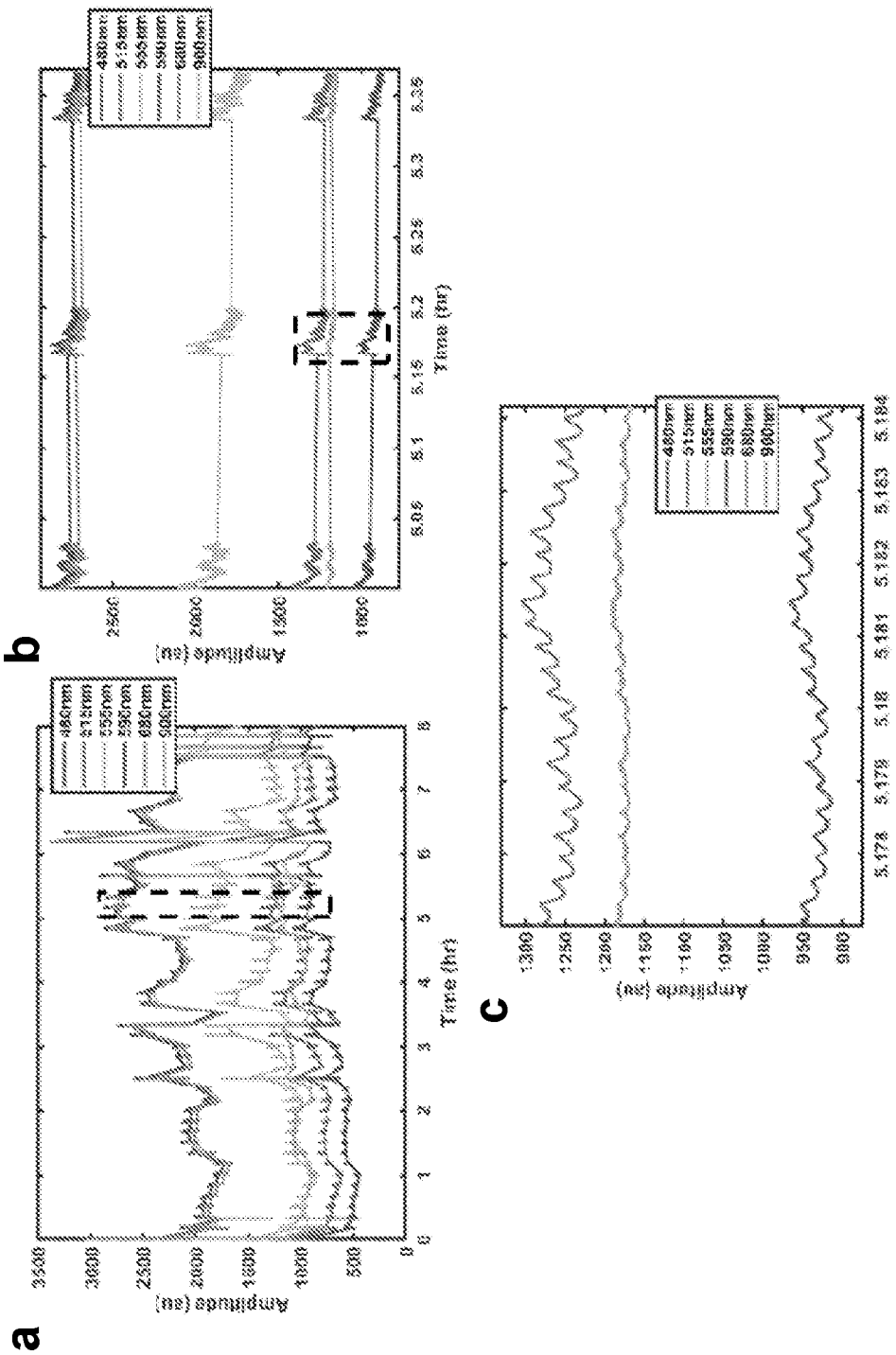

a
b
c
Amplitude (au)
Time (hr)
480nm
515nm
535nm
590nm
680nm
980nm

FIG. 19B

Comparison	n	Mean (std. dev.)	Welch's t-statistic	Brunner-Munzel W
Baseline	2929	0.15 (5.20)	-	-
Baseline vs. Breath Hold	207	9.69 (8.61)	-15.74 (****)	30.81 (****)
Baseline vs. Valsalva I/IV	444	1.41 (11.15)	-2.33 (.02)	.0224 (.982)
Baseline vs. Valsalva II/III	331	4.51 (12.01)	-6.54 (****)	5.31 (****)
Baseline vs. Exercise-Active	7799	-7.13 (2.90)	71.73 (****)	-109.1 (****)
Baseline vs. Exercise-Post	1303	-6.33 (5.26)	37.17 (****)	-64.84 (****)
Baseline vs. Sauna	2312	-6.85 (2.89)	79.43 (****)	-144.1 (****)
Baseline vs. Cold Pressor	732	16.22 (11.73)	-36.18 (****)	67.82 (****)
Baseline vs. Surgical Pressors	25	49.99 (22.55)	-11.05 (****)	685.1 (****)

FIG. 20

INTERNATIONAL SEARCH REPORT

International application No.
PCT/US2024/034184

A. CLASSIFICATION OF SUBJECT MATTER

A61B 5/0245(2006.01)i; **A61B 5/024**(2006.01)i; **A61B 5/11**(2006.01)i; **A61B 5/00**(2006.01)i

According to International Patent Classification (IPC) or to both national classification and IPC

B. FIELDS SEARCHED

Minimum documentation searched (classification system followed by classification symbols)

A61B 5/0245(2006.01); A61B 5/00(2006.01); A61B 5/0205(2006.01); A61B 5/021(2006.01); A61B 5/024(2006.01); G16H 50/20(2018.01); H05K 1/02(2006.01); H05K 1/18(2006.01)

Documentation searched other than minimum documentation to the extent that such documents are included in the fields searched

Korean utility models and applications for utility models
Japanese utility models and applications for utility models

Electronic data base consulted during the international search (name of data base and, where practicable, search terms used)

eKOMPASS(KIPO internal) & Keywords: electrocardiogram, mechano-acoustic, multi-spatial, multi-wavelength photoplethymography, hemodynamic metric, local vascular metric

C. DOCUMENTS CONSIDERED TO BE RELEVANT

Category*	Citation of document, with indication, where appropriate, of the relevant passages	Relevant to claim No.
X	US 2023-0055617 A1 (ANALYTICS FOR LIFE INC.) 23 February 2023 (2023-02-23) See paragraphs [42]-[50] and figures 1,2.	1,2,12-14,24,25
Y		3-11,15-23
Y	US 2022-0330885 A1 (NORTHWESTERN UNIVERSITY) 20 October 2022 (2022-10-20) See paragraph [36] and claims 24-28.	3,7-11,15,19-23
Y	US 2022-0401037 A1 (BIOINTELLISENSE, INC.) 22 December 2022 (2022-12-22) See paragraph [51].	4-6,16-18
A	US 2020-0121258 A1 (ALAYATEC, INC.) 23 April 2020 (2020-04-23) See paragraphs [29]-[45].	1-25
A	US 2020-0315019 A1 (CARNEGIE MELLON UNIVERSITY) 01 October 2020 (2020-10-01) See paragraphs [22]-[30] and figures 1A-3F.	1-25

☐ Further documents are listed in the continuation of Box C. ☑ See patent family annex.

* Special categories of cited documents:
"A" document defining the general state of the art which is not considered to be of particular relevance
"D" document cited by the applicant in the international application
"E" earlier application or patent but published on or after the international filing date
"L" document which may throw doubts on priority claim(s) or which is cited to establish the publication date of another citation or other special reason (as specified)
"O" document referring to an oral disclosure, use, exhibition or other means
"P" document published prior to the international filing date but later than the priority date claimed
"T" later document published after the international filing date or priority date and not in conflict with the application but cited to understand the principle or theory underlying the invention
"X" document of particular relevance; the claimed invention cannot be considered novel or cannot be considered to involve an inventive step when the document is taken alone
"Y" document of particular relevance; the claimed invention cannot be considered to involve an inventive step when the document is combined with one or more other such documents, such combination being obvious to a person skilled in the art
"&" document member of the same patent family

Date of the actual completion of the international search	Date of mailing of the international search report
14 October 2024	**14 October 2024**

Name and mailing address of the ISA/KR	Authorized officer
Korean Intellectual Property Office **189 Cheongsa-ro, Seo-gu, Daejeon** **35208, Republic of Korea**	**LEE, Kang Ha**
Facsimile No. **+82-42-481-8578**	Telephone No. **+82-42-481-5687**

INTERNATIONAL SEARCH REPORT
Information on patent family members

International application No.
PCT/US2024/034184

Patent document cited in search report	Publication date (day/month/year)	Patent family member(s)	Publication date (day/month/year)
US 2023-0055617 A1	23 February 2023	CA 3229058 A1	02 March 2023
		CA 3229061 A1	02 March 2023
		CA 3229081 A1	02 March 2023
		CA 3229089 A1	02 March 2023
		CA 3229090 A1	02 March 2023
		CA 3229092 A1	02 March 2023
		CA 3229098 A1	02 March 2023
		CA 3229112 A1	02 March 2023
		CN 118102970 A	28 May 2024
		EP 4391892 A1	03 July 2024
		US 2023-0071085 A1	09 March 2023
		US 2023-0071467 A1	09 March 2023
		US 2023-0072281 A1	09 March 2023
		US 2023-0075570 A1	09 March 2023
		US 2023-0075634 A1	09 March 2023
		US 2023-0076069 A1	09 March 2023
		US 2023-0127355 A1	27 April 2023
		WO 2023-026151 A1	02 March 2023
		WO 2023-026152 A1	02 March 2023
		WO 2023-026153 A1	02 March 2023
		WO 2023-026154 A1	02 March 2023
		WO 2023-026155 A1	02 March 2023
		WO 2023-026156 A1	02 March 2023
		WO 2023-026158 A1	02 March 2023
		WO 2023-026160 A1	02 March 2023
US 2022-0330885 A1	20 October 2022	EP 4027871 A1	20 July 2022
		EP 4027871 A4	30 August 2023
		WO 2021-050818 A1	18 March 2021
US 2022-0401037 A1	22 December 2022	WO 2022-266392 A1	22 December 2022
US 2020-0121258 A1	23 April 2020	None	
US 2020-0315019 A1	01 October 2020	US 10757815 B2	25 August 2020
		US 11523514 B2	06 December 2022
		US 2019-0215965 A1	11 July 2019